

Membrane Conductance Through Voltage-Gated Ion Channels in the Presence of Carbon Nanomaterials and Dielectrophoretic Force

BY

LORIN MARI JAKUBEK

A DISSERTATION SUBMITTED IN PARTIAL FULFILLMENT OF THE
REQUIREMENTS FOR THE
DEGREE OF DOCTOR OF PHILOSOPHY
IN THE PROGRAM IN BIOMEDICAL ENGINEERING
AT BROWN UNIVERSITY

PROVIDENCE, RHODE ISLAND

MAY, 2011

© Copyright Lorin Mari Jakubek May 2011

This thesis submitted by Lorin Mari Jakubek is accepted in its present form
by the Center for Biomedical Engineering
as satisfying the thesis requirements for the degree of
Doctor of Philosophy.

Date _____

Robert H Hurt, Ph.D., Advisor

Recommended to the Graduate Council

Date _____

Diane Lipscombe, Ph.D., Reader

Date _____

G. Tayhas R. Palmore, Ph.D., Reader

Date _____

Anubhav Tripathi, Ph.D., Reader

Date _____

Ravi Bellamkonda, Ph.D., External Reader

Approved by the Graduate Council

Date _____

Peter M. Weber, Ph.D.
Dean of the Graduate School

Lorin M. Jakubek

Lorin_Jakubek@Brown.edu

Biomedical Engineering
Brown University
Box D, Engineering
Providence, RI 02912

Education

BROWN UNIVERSITY, Providence, RI

Ph.D., Biomedical Engineering, expected Spring 2011
Advisor: Robert Hurt

WORCESTER POLYTECHNIC INSTITUTE, Worcester, MA

B.S., Chemical Engineering, May 2003
Minor: Biochemistry

Research Experience

Research Assistant – Brown University Sept. 2004 to Present
Biomedical Engineering doctoral candidate in the laboratory of Robert Hurt, Ph.D. Collaborative research with Diane Lipscombe Ph.D., Neuroscience Department
Studying the effects of carbon nanotubes on electrically active cells and astrocytes.

Research Intern – Millipore Corporation Summer 2004
Enhanced the design of a confidential material to simplify its use and make it applicable to many more biological platforms.

National Institutes of Health Intramural Training Fellowship Summer 2003
Research Assistant in the laboratory of Thomas Reese, Ph.D. at the Marine Biological Laboratory in Woods Hole, MA.
Characterized Squid Myosin VI antibodies and determined alternative splice sites within the genetic sequence.

National Science Foundation REU Summer 2002
Research Assistant in the laboratory of Gregory Lnenicka, Ph.D. at the University at Albany.
Studied the effect of the second messenger cAMP on the development of drosophila synaptic terminals.

Publications

Jakubek, LM; Hurt, RH. In Press **Nanomaterials and Ion Channels: Observed Effects and Possible Mechanisms**. in VR Preedy (Ed) *Nanomedicine and the Nervous System*. Science Publishers USA

Jakubek, LM; Marangoudakis, S.; Raingo, J.; Liu, X.; Lipscombe, D.; Hurt, RH. 2009 **The inhibition of neuronal calcium ion channels by trace levels of yttrium released from carbon nanotubes**. *Biomaterials*. 30(31) 6351-6357.

Pethig, R., Jakubek, LM, Sanger, RH, Heart, E., Corson, ED, and Smith, PJS. 2005 **Electrokinetic measurements of membrane capacitance and conductance for pancreatic beta-cells**, *IEE Proc. Nanobiotechnology*. 152,189-193.

Press Releases

Featured in a *Nature News* Article and *Nature Neuroscience Podcast* November 2008
Interviewed during my presentation at the annual Society for Neuroscience Conference,
Washington, DC

<http://www.nature.com/news/2008/181108/full/news.2008.1238.html>

Featured in a Brown University Engineering Ingenuity Podcast. A podcast designed to highlight
noteworthy research conducted at Brown.

Fellowships and Academic Honors

Reginald D. Archambault Award for Teaching Excellence – Honorable Mention	2010
Graduate Assistance in Areas of National Need Fellowship	2009 - 2010
NSF Summer Institute on Nano-Mechanics, Nano-Materials and Micro/Nano Manufacturing Fellowship to attend NEMB2010 and NanoEngineered Therapeutics I & II workshops	2010
National Institutes of Health Intramural Training Fellowship	2003
National Science Foundation Research Experience for Undergraduates Award	2002

Teaching Experience

Instructor – Brown University Summers 2007-2010
Developed and taught “Exploring the Interface Between Nanotechnology and Biology”
An intensive Summer course for the *Summer at Brown Program*.

Teaching Assistant – Genetics - Brown University Fall 2005
Led two laboratory sections and help sessions. Graded exams and homework.

Teaching Assistant – Developmental Biology – Brown University Fall 2005
Led review sessions and laboratory section. Graded exams and homework.

Peer Leader – Calculus 1 & 2 – Worcester Polytechnic Institute 2000 –2002
Led two help sessions a week through the *Math and Science Help (MASH)* program.

Academic Societies

Sigma Xi
Biomedical Engineering Society
American Association for the Advancement of Science
Society for Neuroscience

Acknowledgements

First of all, I would like to thank my advisor Prof. Robert Hurt for giving me the freedom, independence and means to explore my experimental ideas while at the same time providing a safety net of support when I needed it. His astute advice, expertise, and experience provided great insight into how to be successful in an academic research environment. It was an invaluable experience.

I would also like to thank Diane Lipscombe who supported my Nano/Neuro interdisciplinary aspirations by allowing me to work on projects in her lab and with the support of members of her team. She has a unique perspective and is a wonderful mentor to the students in her lab. In treating me as one of her own; she provided me with sound advice along the way.

I would also like to thank Peter JS Smith and Ronald Pethig with whom I had the opportunity to work on the dielectrophoresis project in Peter Smith's Lab at the Marine Biological Laboratory in Woods Hole, MA. It was a wonderful project and served to introduce me to Biomedical Engineering at Brown. I sincerely appreciate their continued support.

While I was still an undergraduate at WPI, Professor Elaine Bearer was the first professor I spoke to at Brown. I would like to thank her for her support and for fostering my early scientific endeavors.

My other committee members, past and present, Professors Anubhav Tripathi, Diane Hoffman-Kim, Tayhas Palmore, and Ravi Bellamkonda each deserve a special thank you for their time, support, and advice. I would especially like to thank Professor Ravi Bellamkonda, my outside reader, for taking the time to travel from Georgia Tech and for attending my defense. I sincerely appreciate it!

My labmates: Xinyuan Liu, Love Sarin, Lutfiye Bulut-Altay, Aihui Yan, Lin Guo, Jingyu Liu, Fei Guo, Yantao Chen, Meagan Creighton, Indrek Kulaots, Yang Qiu and Zhongying Wang. Thank you for years of support, friendship and ‘lab outings!’ I would like to thank in particular Xinyuan Liu, Spiro Marangoudakis, Jessica Raingo and Thomas Helton with whom I have had the opportunity to collaborate on neuro/nano projects and Joe Orchard, David Murray, Geoffrey Williams and Sylvia Denome for their technical support.

To my dear friends - my thesis support team - graduate school would not have been the same without you! Ryan Carey, Zaheer Kapadia, Sharon Kuhn, Boris Masis, Miles Schofield, and Prema Srinivasan; Thank you so much for your friendship, countless adventures and numerous hours of ballroom dancing! Greg Vemis, with laughter and support, thank you for always being by my side! My WPI suities: Kara Hartling-Bennett, Cindy Leung, Cinthia Chung-Ngo and Disha Vachhani thanks for years of friendship, encouragement and good times. John Raiti and George Aninwene – Thank you so much! Nicolas Boudreau, thank you for your ‘miłość & wsparcie’ – graduate students writing their theses aren’t usually this happy. Thank you!

To my family, my brothers John, Craig and Todd; you have supported me in this pursuit as well as all the pursuits of my life and have always given me giant big-brother shoulders to lean on - thank you! My sister-in-law Elizabeth, Shannon and Sara thank you for many good times and support.. My niece and nephews, Annie, Ben, Sam, James and David - being a role model for you has been an inspiration to me - thank you for being so cute and curious about the world of science. Lastly, my Mom and Dad, words can’t express my gratitude. With your unconditional love and support you have always been by my side in successes and challenges. I’m so happy to share this most recent success with you!

In Deo Speramus

Table of Contents

1. Introduction.....	1
Effect of Carbon Nanotubes on Voltage-Gated Ion Channels.....	3
1.1 Carbon Nanomaterials in Neuroscience.....	3
Nanotechnology.....	3
Carbon Nanomaterials.....	4
Applications in Neuroscience.....	6
1.2 Carbon Nanomaterials affect Voltage-Gated Ion Channels.....	8
Voltage-gated Ion Channels.....	9
Ion Channels – Types and Functions.....	9
Carbon Nanomaterials and Voltage-gated Ion Channels.....	12
1.3 Nanomaterials and Ion Channels	14
Interaction of Nanometals with Ion Channels.....	14
Interaction of Quantum Dots with Ion Channels.....	15
Possible Interaction Mechanisms	17
Dielectrophoresis for Tissue Engineering of Pancreatic Islets.....	27
1.4 Diabetes.....	27
Treatment Options.....	28
1.5 Dielectrophoresis for Insulin-Secreting Cells.....	31
Islets of Langerhans.....	32
Tissue Engineering with Dielectrophoresis.....	34
Dielectrophoresis Principles.....	36
Dielectrophoresis for Pancreatic Islets.....	43

1.6 References.....	45
2. Electrokinetic Measurements of Membrane Capacitance and Conductance for Pancreatic β -cells.....	53
2.1. Introduction.....	53
2.2. Theory.....	55
2.3. Experimental.....	57
2.4 Results.....	61
2.5. Discussion and Conclusions.....	66
2.6. References	70
3. Inhibition of Neuronal Calcium Ion Channels by Trace Levels of Yttrium Released from Carbon Nanotubes.....	73
3.1 Introduction.....	73
3.2 Materials.....	74
3.3 Results.....	77
3.4 Discussion.....	87
3.5 Conclusions.....	90
3.6 Supplemental.....	91
3.7 References.....	94
4. Conclusions and Future Perspectives.....	98
4.1 Electrokinetic Measurements of Membrane Capacitance and Conductance for Pancreatic β -Cells.....	98
Conclusions.....	98
Future Studies.....	99
4.2 Inhibition of Neuronal Calcium Ion Channels by Trace Levels of Yttrium Released from Carbon Nanotubes.....	100

Conclusions.....	100
Implications.....	101
Future Studies.....	106
Applications to Chronically Implanted Neural Electrodes.....	107
Preliminary Results.....	115
4.3 References	122

Table of Figures

Figure 1.1 Carbon Nanostructures.....	5
Figure 1.2 Schematic of Nanotube Growth Method.....	5
Figure 1.3 Summary of Ion Channel Structure and Fuction.....	11
Table 1.1 Summary of Ionic Radii, Hydration Energies, Ligand Preferences and Effects on VGCC.....	20
Figure 1.4 Summary of Proposed Mechanisms of Nanomaterial Interactions with Voltage-Gated Ion Channels.....	26
Figure 1.5 Diagram of Typical Islet of Langerhans.....	33
Figure 1.6 Dipole effects on a Sphere Suspended in Media Exposed to an Electric field.....	38
Figure 1.7 Electrorotation.....	41
Figure 1.8 Dielectrophoretic Pearling.....	42
Figure 2.1 Dielectrophoretic Chamber.....	61
Figure 2.2 Electrorotation Spectra.....	62
Table 2.1 Anti-field Electrorotation Rate.....	63
Figure 2.3 Plots of Electrorotation Data.....	64
Table 2.2 DEP Cross-over Frequency.....	65
Figure 2.4 Plot of DEP Cross-over Data.....	65
Figure 3.1 SWNT Sample A Inhibits Calcium Ion Channels, while SWNT Sample B Does Not.....	78
Figure 3.2 Bioavailable Nickel and Yttrium in SWNT Samples.....	80
Figure 3.3 Control Experiments with Soluble Salts Isolate the Effects of Ni and Y on Neuronal Voltage-Gated Calcium Ion Channels.....	82
Figure 3.4 Yttrium Phases in SWNTs and Mechanisms of Yttrium Ion Release and Recapture by SWNT Surface Functional Groups.....	84

Figure 3.5 Summary of Proposed Mechanism Through which Carbon Nanotube Suspensions Inhibit Neuronal Calcium Ion Channels.....	86
Figure 4.1 Carbon Nanomaterial and Yttrium Oxide Scaffolds.....	116
Figure 4.2 Astrocyte cell line exposed to acidic conditions.....	119
Figure 4.3 Western blot of Astrocyte Activation as a Function of Media pH ...	119

Chapter 1

1. Introduction

My doctoral work involves contributions to two distinct projects. The major project pertains to the effect of carbon nanomaterials on voltage-gated ion channels. The minor project involves the use of dielectrophoresis to control the electrokinetic functions of pancreatic beta cells. This introduction, therefore, addresses both areas.

Carbon nanomaterials are being used in the field of neuroscience with increasing frequency, as substrates for neuronal growth and stimulation, to electrode coatings to decrease impedance and increase charge transfer. However, the majority of research involves complex material and cellular systems which preclude a fundamental understanding of how distinct material features affect cellular response. This can lead to contradictions and misunderstandings in the literature. One such contradiction involves the effect of carbon nanotubes on calcium homeostasis. A specific aim of my research has been to study the fundamental effects of carbon nanomaterials on voltage-gated ion channels. This is presented in Chapter 3. The first part of this introductory chapter reviews carbon nanomaterials, their application in neuroscience and their effect on voltage-gated ion channels; it concludes with a review of the observed

nanomaterials' effect on voltage-gated ion channels and proposes possible mechanisms underlying the cellular response.

The second part of the introduction addresses the use of dielectrophoresis as a technique in tissue engineering the islets of Langerhans. The incidence of diabetes in this country and abroad is increasing. The finger-prick/insulin injection treatment method is sufficient (albeit uncomfortable) for most of the affected population. However, there is a portion of the affected population that has inhibited glycemic control, and consequently are unable to maintain proper levels even with monitoring. For this population, pancreatic islet transplantation is viewed as a promising experimental treatment strategy. However, a shortage of organ donors limits its use and continued research. This section of the introduction provides an overview of diabetes as a condition, challenges to treatment, and suggests tissue engineering as a viable mechanism to overcome the shortage of organ donors. It describes the islet of Langerhans in detail, the technique of dielectrophoresis and concludes by suggesting this as a mechanism by which islets can be generated. The first steps in pursuing dielectrophoresis for pancreatic islet tissue engineering is provided in Chapter 2.

Chapter 4 reviews conclusions of the works and looks ahead towards future research initiatives. Some research has already been conducted toward these initiatives and will be reviewed in this section.

Effect of Carbon Nanotubes on Voltage-Gated Ion Channels

1.1 Carbon Nanomaterials in Neuroscience

Nanotechnology

According to the National Nanotechnology Initiative '*Nanotechnology is the understanding and control of matter at dimensions of roughly 1 to 100 nanometers, where unique phenomena enable novel applications.*' While some nanomaterials are nanoscale isolations of materials that currently exist in bulk macroscale forms; they are considered novel and unique due to the differences in material properties observed at the nanoscale versus the macroscale. As the dimensions of the materials change, there is a shift in the dominant forces acting to affect material properties.

At the macroscale, gravitational forces dominate, classical mechanics describes the movement of objects, and objects have a small surface-to-volume ratio. At the nanoscale, electrostatic forces dominate, quantum mechanics describes movement, and objects have a very large surface-to-volume ratio. Consequently, macroscale and nanoscale objects of the same material can have differences in optical, mechanical, thermal, magnetic and electrical characteristics.

When interfacing nanomaterials with biological systems, this variation in material behavior at the nanoscale provides both the opportunity for novel applications as well as the potential for unexpected or undesired cellular response. For this reason, it is imperative to conduct fundamental biological

assays evaluating the biological effect of nanomaterials in controlled environments. In this way, known variables can be accounted for, and presently unknown variables can be discovered. Due to the potential applications for carbon nanomaterials in neuroscience, and the contradiction in the literature regarding their effect on cellular calcium homeostasis, the research presented in Chapter 3 is a fundamental assay on the effects of carbon nanomaterials on voltage-gated calcium ion channels.

Carbon Nanomaterials

Carbon nanotubes are well-ordered allotropes of carbon in the form of graphene rolled into seamless cylinders (Figure 1.1). A single-walled nanotube (SWNT) is, as the name implies, a nanotube cylinder comprised of only a single wall. Multi-walled nanotubes (MWNT) are therefore composed of multiple concentric cylinders. An intermediary structure, the double-walled nanotube, is a double layer of concentric cylindrical graphene. Carbon nanotubes have a high aspect ratio with a diameter ranging from 0.5 to 2nm for SWNTs (2nm – 100nm diameter for MWNT) and a length varying from tens of nanometers to several hundred micrometers.

Carbon nanomaterials are synthesized through one of three methods: laser ablation, chemical vapor deposition or electric arc discharge. Catalytic routes, shown in Figure 1.2, are the most common synthesis methods for large scale production. This method produces materials that contain residual catalytic metals. Even with the addition of vendor purification steps, the catalytic metals

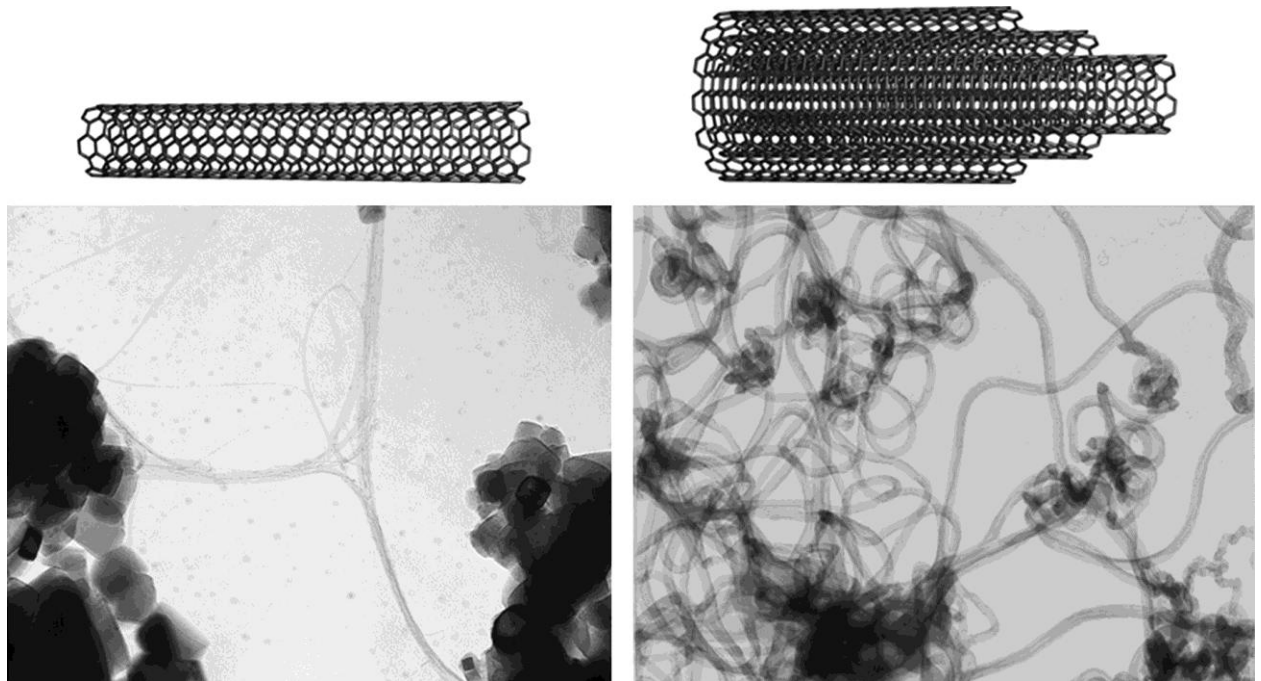


Figure 1.1 Carbon Nanostructures.

Molecular representations of SWNT (top left) and MWNT (top right) with typical transmission electron micrographs below. Figure taken with permission from Donaldson et al¹¹

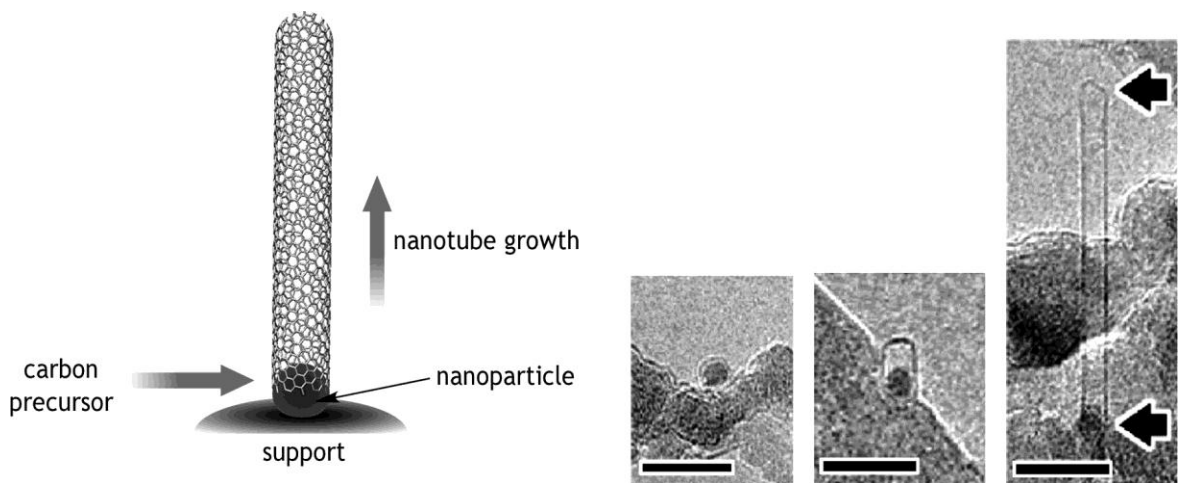


Figure 1.2 Schematic of Nanotube growth method.

Left: Schematic of catalytic metal nanoparticles with nanotube growth. Right: TEM of growing nanotubes. Image taken with permission from Donaldson et al¹¹

are currently part of the resultant product. The most common catalytic metals are nickel, yttrium, iron, cobalt and molybdenum.

In addition to a high aspect ratio, carbon nanomaterials have very high tensile strength and Young's modulus values, making them both strong and elastic. Due to very strong Van der Waals forces, nanotubes tend to bundle or aggregate. Surface modification techniques can be employed to improve dispersion or to add biological functionality, such as, antibody-enabled 'targeting.' Additionally, carbon nanotubes are electrically conductive. The conformation of the carbon atoms in the graphene sheet comprising the nanotube cylinder into either armchair, chiral or zig-zag patterns dictates the conductivity of the nanotubes. These qualities make carbon nanomaterials very attractive for biomedical applications and particularly the area of neuroscience as described in the next section.

Applications in Neuroscience

The main applications of carbon nanomaterials in neuroscience thusfar have pertained to controlling neuronal growth, stimulation and, more recently, neuroprotection. This section provides an overview of the current literature in these areas.

Carbon nanotubes, being strong, flexible and potentially conductive, are also the same size and shape as neuronal processes. Therefore, while the field is not even 15 years old, many research groups have published many papers focused on the development of carbon nanotubes as a biomaterial for neuronal growth. A study conducted by Mattson et al⁴⁴ in 2000 was the first to

demonstrate rat hippocampal neurons successfully grown on multi-walled nanotube scaffolds. Since then, the ability to control scaffold surface properties has improved. Neurons have been shown to grow in response to nanotube scaffold surface charge²¹, alignment⁵³ and in response to adhered neurotrophic factors⁴³. Importantly, covalent modification of carbon nanotube scaffolds with neurotrophins (protein growth factors that aid in the survival and differentiation of neurons) successfully showed that while the neurotrophin is bound to the nanotube, it retains its biological functionality and effect on neuronal growth⁴³. This demonstrates that factors bound to carbon nanotube scaffolds can retain their biological functionality.

Neurons grown on selectively patterned islands of carbon nanotubes positioned on quartz coverslips have been shown to be a novel mechanism for developing neural networks. The neurons preferentially relocate and grow on micro-patterned arrays of carbon nanotube islands and extend processes across the non-permissive quartz regions to neurons on neighboring islands^{15, 62}. The network can be maintained for up to eleven weeks⁶² suggesting the potential use as a biosensor or in the development of neuropharmaceuticals.

The electrical conductivity of carbon nanotubes can also be a benefit to the field of neuroscience. It was observed that electrodes used at the brain-machine interface, coated with nanotubes, have an increased charge transfer rate and decreased impedance as compared to native electrodes³⁰. Moreover, vertically aligned microchip arrays of carbon nanotubes are able to stimulate neurons grown upon them with high charge transfer and without faradic

interactions⁶⁸. This increases the ability of the electrode to record and stimulate neurons. On a cellular level, nanotube scaffolds have been used to stimulate and record from neurons³⁴ and have been suggested to increase the electrical activity of neurons^{40, 45} through tight electrical contacts⁴⁵.

While the potential for carbon nanomaterials for neurological applications is very promising, a great deal of research needs to be conducted in order to completely understand the mechanisms underlying the physiological responses observed. In some cases the route of the physiological response may be resulting from a minor material feature. A recurring theme of this dissertation is the need for fundamental studies involving cellular-material interactions. Therefore, a main objective of this work is to evaluate the effect of carbon nanomaterials on voltage-gated ion channels. A review of voltage-gated ion channels and carbon nanomaterial affects is described in the next section.

1.2 Carbon Nanomaterials Affect Voltage-Gated Ion Channels

Voltage-gated ion channels (VGIC) are essential to all functions of the nervous system, from maintaining membrane potential and synaptic transmission, to endocrine functions. Recent research has shown altered channel function and consequently, altered nervous tissue response with the addition of certain nanomaterials. This section provides an overview of voltage-gated sodium, potassium and calcium ion channels, their structure, function and a review of current literature regarding channel interactions with carbon nanomaterials.

Voltage-gated Ion Channels

The importance of ion homeostasis to the proper function of nervous tissue has been widely known and accepted for over a century. The early work of Sidney Ringer in the late 1800s showed the extracellular solution perfusing a frog heart must contain defined concentrations of sodium, potassium and calcium ions in order for the heart to beat normally ¹⁹. Today, the cellular roles and mechanisms of entry of these ions are well established and applied to the development of pharmaceuticals targeting conditions such as anxiety, epilepsy and pain.

Therefore, the development of novel biomaterials for the nervous system must consider the material interaction with the rudiments of cellular excitability, ie maintenance of membrane potential through ion channels. Quantum Dots (QD) ⁶³, nanometals ¹⁶ and carbon nanomaterials ⁹ have all been shown to alter neural network activity. This section summarizes the available literature regarding the interactions of nanomaterials with VGICs and postulates potential mechanisms underlying these effects.

Ion Channels – Types and Functions

The fluid in and around excitable cells of the nervous system is composed of numerous ionic species, the most abundant being sodium, calcium, potassium, and chloride. Finite ionic gradients define an electrochemical potential across the cellular membrane of excitable cells. At rest, the flow of ions through ion channels and pumps maintains the membrane potential. Ion channels are membrane-bound, pore-forming proteins that enable and facilitate the transfer of ions across the cellular membrane (Figure 1.1B). The response of ion channels

to chemical signals, electrochemical gradients and mechanical tension enables efficient cellular signaling and control of cellular homeostasis. Ion channels are essential to all forms of life, from humans to single-celled organisms, and many pathological conditions derive from, or are exacerbated by, abnormal ion channel function.

Under excitatory conditions, voltage-gated ion channels (VGICs) successively open and close in response to alterations in membrane potential, enabling the flow of ionic current and the propagation of the action potential down the axon. This process is the hallmark of neuronal communication (Figure 1.3A). This section will focus on sodium, calcium and potassium channel members of the superfamily of VGICs. Members of this family are structurally related¹⁹ and have three complimentary aspects, namely, ion conductance, pore gating and regulation⁷¹. For all members, the pore motif is formed by the four homologous domains consisting of six transmembrane regions (Figure 1.3D) comprising the α subunit. For voltage-gated calcium channels (VGCCs) and voltage-gated sodium channels (VGSCs), the four domains of the α subunit are linked together. In voltage-gated potassium channels (VGKCs) they are unlinked. Each domain contains a voltage-sensing transmembrane region which contains repeated positively charged amino acid residues¹⁹. Upon depolarization, the change in membrane potential moves this region towards the extracellular space causing a conformational shift in the protein that opens the channel to allow the flow of current¹⁴ (Figure 1.3C). Each member of the superfamily has a unique

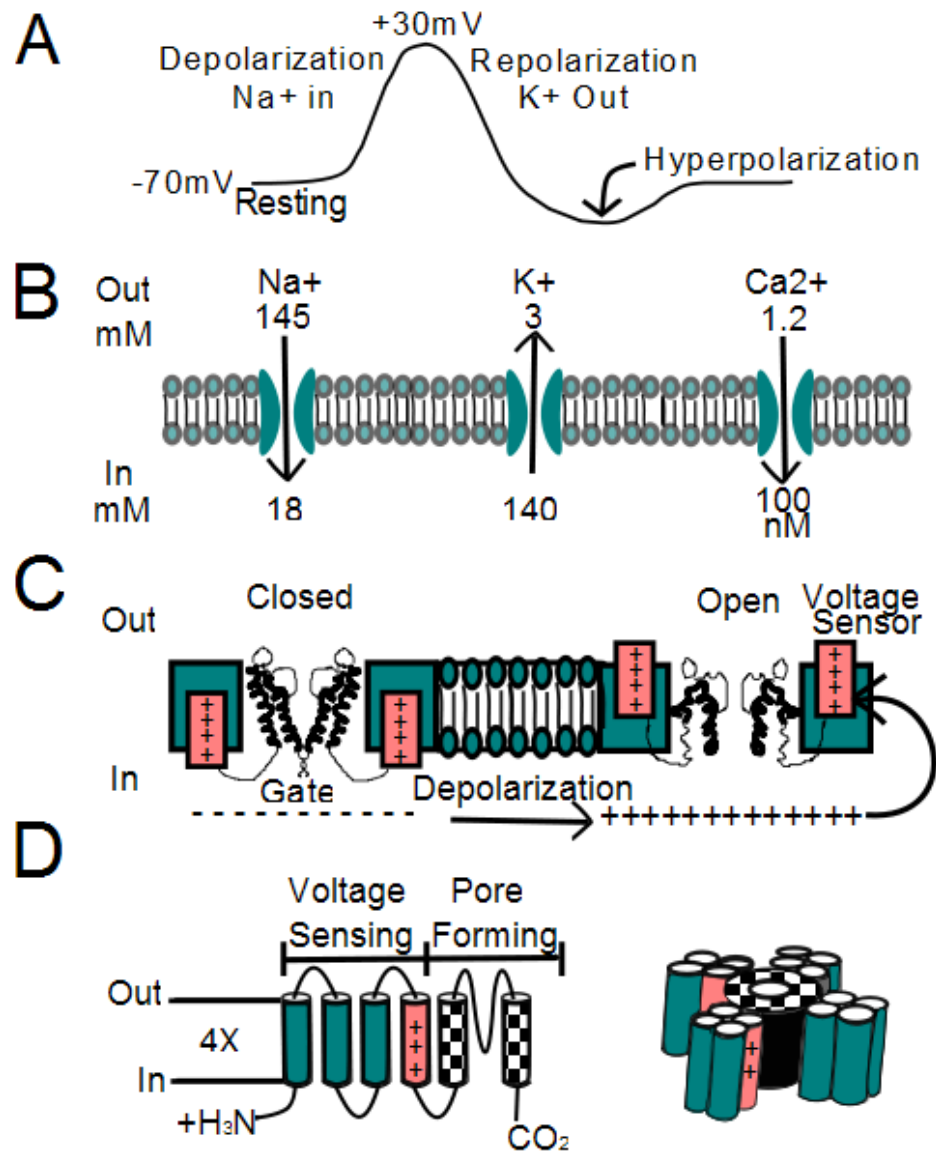


Figure 1.3 Summary of Ion Channel Structure and Function.

A. Action potential diagram. At rest, membrane potential is -70mV . When an action potential is fired, VGSC open and the membrane depolarizes.

Depolarization opens VGKC which pass potassium ions to the extracellular space. VGKCs are responsible for repolarizing the membrane. B. Direction of movement of target ions of voltage-gated ion channels. Relative concentration gradients for ions are provided. C. VGIC mechanics. At rest, the membrane potential is negative and the voltage sensor is at the interior of the membrane. Depolarization causes an influx of positive charge that electrostatically repulses the voltage sensor and consequently opens the channel enabling the passage of current. With permission from Elinder et al¹⁴. D. Simplified schematic of six transmembrane regions comprising one domain of the VGKCs α -subunit. Four domains form the channel shown on the right. Grey transmembrane region is the voltage sensor. With permission from Börjesson et al⁵.

selectivity filter that extends into the pore to preferentially coordinate the throughput of the respective target ions.

VGSC are responsible for the upstroke of the action potential (Figure 1.3A) in nerve, muscle and endocrine cells and in some cases contribute to pacemaker and subthreshold potentials that underlie the decisions to fire an action potential. Given the higher intracellular potassium concentration, VGKC shuttle potassium ions out of the cell and serve to dampen excitation. In this way, VGKCs repolarize the membrane after depolarization events, time the interspike interval during repetitive firing, and lower the effectiveness of excitatory inputs ¹⁹ (Figure 1.3A).

VGCC convert membrane depolarization events into an inward calcium flux essential for muscle contraction, neurotransmission, hormone secretion, gene expression and neurite outgrowth ⁸. VGCCs are classified into three families: Ca_v1, Ca_v2 and Ca_v3. Members of the Ca_v1s are abundant in the retina, skeletal and cardiac muscles. Ca_v2 members are distributed throughout the nervous system and cluster near presynaptic terminals. The entry of calcium through some Ca_v2 members enables vesicle fusion and release of neurotransmitter across the synapse. Ca_v3 members activate near resting potential and are responsible for establishing oscillating firing patterns and rebound bursts ⁷.

Carbon Nanomaterials and Voltage-gated Ion Channels

Carbon nanotubes are electrically conductive and on the same scale as growing neurons. Consequently, nanotubes have been considered in a number of

studies as potential novel biomaterials for neuronal growth⁵⁰ and stimulation⁹. Neurons grown in the presence of water soluble arc-synthesized SWNT functionalized with polyethelene glycol (PEG) demonstrated altered neurite outgrowth patterns consistent with alterations in calcium homeostasis. Using calcium sensitive dyes, Ni et al showed that upon exposure to SWNT-PEG, the intracellular calcium levels were not being restored, suggesting SWNT-PEG was an inhibitor of depolarization-dependent calcium influx⁵⁰. A later study focused on the interaction of arc-synthesized SWNTs on the cultures of primary neurons and glia cells⁴. Whole-cell patch clamp recordings of dorsal root ganglia cells exposed to bundled SWNTs revealed diminished inward conductivity and a more positive resting potential. The authors postulate that their results could be explained if VGCC were affected by the nanotubes⁴.

Although these studies demonstrate an inhibition of ion channel conductance, and an inhibition of calcium current in particular, other studies suggest enhancement of calcium channel activity. Single-cell electrophysiology techniques, which have been used to assess the ability of carbon nanotube mats to stimulate networks of neurons, recorded after potential depolarization events in stimulated cells. These events were inhibited by calcium channel blockers suggesting the nanotubes were in fact enhancing calcium uptake through alterations in the location or function of VGCCs⁹.

Some of the literature regarding multi-walled carbon nanomaterials and potassium ion channels is also contradictory. Early work showed that unmodified SWNTs could inhibit potassium channel function in Chinese hamster ovary cells,

whereas MWNTs did not show appreciable inhibition. The authors suggest direct pore occlusion as the mode of action⁵¹. Contrastingly, later work suggests that MWNTs are antagonists to VGKCs expressed in the pheochromocytoma (PC12) cell line⁶⁹. The mode of action of the inhibition is presently unknown, as is the relation between wall number, surface chemistry, and metal impurities in the nanotubes.

Motivated by the contradictory literature regarding SWNTs and calcium ion channel homeostasis mentioned above, the specific aim of the research presented in Chapter 3 is to evaluate the effect of SWNTs on calcium homeostasis in a simplified experimental system of a cell line expressing only the neuronal type voltage-gated calcium ion channel.

1.3 Nanomaterials and Ion Channels

In order to develop hypotheses regarding the mechanisms by which nanomaterials may be interacting with voltage-gated ion channels, this section expands the background to include a review of current literature regarding channel interactions with quantum dots and nanometals. Based on this literature, I postulate potential mechanisms of interaction, namely: release of metal ions, adsorption of target ions onto nanomaterial surfaces, direct nanomaterial interaction and oxidative stress.

Interaction of Nanometals with Ion Channels

Low particle concentrations of nanometals in solution have been shown to disrupt electrical activity of neural networks grown on multielectrode array neurochips¹⁶.

In a series of studies highlighting the effects of ZnO, CuO and Ag nanoparticles on VGKC and VGSC currents in rat hippocampal neurons, the following contrasting effects were observed. ZnO nanoparticles increase the transient outward potassium current (I_A) and delayed rectifier potassium current (I_K) while increasing the overshoot and diminishing the peak half-width of VGKCs⁷². In contrast, CuO nanoparticles have shown that nanoparticles have no effect on I_A , but inhibited I_K . Furthermore, CuO nanoparticles did not shift the steady-state activation curve of I_K and I_A , whereas the inactivation curve of I_K was shifted negatively⁷⁰.

Relatedly, ZnO nanoparticles increase the peak amplitudes of the VGSC while the inactivation and the recovery from inactivation of the sodium current are promoted by ZnO⁷⁰. Silver nanoparticles reduce the amplitude of the sodium current, produce a hyperpolarizing shift in the activation–voltage curve of the sodium current and delay the recovery after inactivation. Furthermore, peak amplitude and overshoot of the evoked single action potential are decreased and half-width is increased with Ag nanoparticles³⁹. If combined, these results suggest that nanosilver decreases peak amplitude and nano-zinc oxide increases peak amplitude. More research is necessary in order to understand the mechanism underlying each effect.

Interaction of Quantum Dots with Ion Channels

Quantum dots (QDs) are 2-100 nm fluorescent semiconducting nanocrystals of interest to biologists as imaging agents due to their high quantum yield, high resistance to photobleaching, broad absorption and narrow emission spectra. In

a study of rat primary cultured hippocampal neurons, exposed to CdSe QDs, the QDs were shown to increase cytoplasmic calcium levels through the influx of calcium from both extracellular and intracellular (mostly endoplasmic reticulum) stores. Concurrently, the CdSe QDs enhanced activation and inactivation, slowed recovery, reduced the percent of available VGSCs and prolonged the time-course of activation. Interestingly, the effect is observed with QDs 10nm and above; however below 10nm, the effect is not seen⁶⁵. The authors suggest that some of these channel effects were similar to the effects of β -scorpion toxin and may in part be due to the binding of the QDs or QD degradation particles to the S3-S4 loop affecting the function of the VGSC voltage sensor. However, the shift in activation to more depolarizing potentials is not consistent with this hypothesis and further research suggests a more elaborate mechanism.

In studying the mechanisms underlying the elevation of intracellular calcium levels, Tang et al (2008a) observed that the addition of T-type calcium channel blocker, mibefradil, and L-type calcium channel blocker, verapamil, did not block the elevation of intracellular calcium observed with CdSe QD exposure. However, the addition of N-type antagonist, ω -conotoxin, partially blocked the calcium influx. Surprisingly, the inhibition of VGSCs with TTX abolished the elevation of intracellular calcium associated with CdSe QD exposure. Interestingly, the group observed that under exposure to CdSe QDs, VGSCs permitted calcium to permeate the channel as readily as sodium and suggested oxidative stress as a factor in the loss of channel selectivity. Additionally, the

passage of sodium through VGSCs enhanced the release of mitochondrial calcium and contributed to the elevated intracellular calcium levels.⁶⁴

The elevation of intracellular calcium levels in neurons not only affects neuronal survivability, but also neurotransmission. In a follow-up study, the effects of CdSe QDs and streptavidin-CdSe/ZnS QDs demonstrated altered synaptic transmission and plasticity in the hippocampal dentate gyrus area of anesthetized rats. Paired-pulse facilitation was also suppressed under QD exposure. As intracellular calcium levels enable the release of neurotransmitter at the synapse, the elevation of intracellular calcium observed previously may account for this suppression.⁶³ While this study concluded that QDs, regardless of modification, could impair synaptic transmission and plasticity; other studies have reported no significant alteration of ion channel function from exposure to QDs³². It is possible that QDs may affect ion channels and processes dependent on ion channel flux through the degradation and release of metal ions (M+s.) This will be discussed further in the next section.

Possible Interaction Mechanisms

Given the biological evidence in the literature reviewed above, along with knowledge of the fundamental behaviors of nanomaterials in biological environments, I propose four potential mechanisms of nanomaterial interaction with ion channels. As shown in Figure 1.4, mechanisms are free M+ effects, adsorption of target ions, direct particle-protein interaction and oxidative stress. Each mechanism can potentially act independently or in concert with one or more other mechanisms to cause alterations of VGIC dynamics.

Free Metal Ion Effects

It is becoming increasingly apparent that the cellular responses to some nanomaterials are in fact attributable to M+s released from the nanomaterial rather than any direct biological interaction of the particle phase itself. For example, the antibacterial action and cytotoxicity of nano-silver is believed to be primarily the result of silver ion (Ag^+) release and the subsequent binding of Ag^+ to thiol targets^{36, 41}. The response of cells to nickel containing compounds is often correlated with the concentration of nickel ions produced by dissolution processes³⁸. An emerging theme is the effect of ion release from nanomaterials on cellular function. This is particularly relevant as M+s have been shown to block the pore, replace target ions and alter the channel dynamics of VGICs. This section discusses M+ release from nanomaterials and mechanisms of M+ effects on ion channels.

Evidence of Metal Ion Release from Nanoparticles

In general, a wide variety of commercially important nanomaterials may coexist with free ions or other soluble species in physiological solution. Many nanomaterials are oxides, and often undergo slow dissolution under physiological or environmental conditions. Good examples of this are ZnO and NiO. Many nanomaterials contain zero-valent metals which, with the exception of gold, are capable of oxidative dissolution to produce ions. The release of M+s from nanometals, such as nanosilver, decreases with increasing pH, increases with increasing temperature, is dependent on oxidation and therefore the concentrations of dissolved oxygen in the environment. Additionally, M+ release

is decreased by the addition of humic or fulvic acids.³⁵ This suggests that under physiological conditions many nanometals will release ions with the potential to act as conventional M⁺ toxicants. Even carbon-based nanomaterials contain metal catalyst residues that may include Ni, Y, Co, Mo, or Fe. These catalyst particle residues have been shown to significantly release soluble metal forms^{29, 38, 56} through oxidative attack on metal catalyst residues that are not fully encapsulated by graphenic carbon shells^{37, 38}.

In addition to carbon nanomaterials and nanometals, QDs have also been shown to release M⁺s. A bare core QD is composed of its primary semiconducting components, which in this form, make it susceptible to interactions with its environment, particularly water and oxygen. Oxidation of the QD will reduce fluorescence and cause degradation²⁴. Passivation techniques involve the modification of the surface with mercaptopropionic acid, silanization and polymer coatings.³² The most widely used surface modification is CdSe with a ZnS shell. While shells reduce ion release, weathering under acidic (pH ≤ 4) or basic (pH ≥ 10) conditions destabilizes the shell resulting in cadmium/selenite ion release (≤ 1 min).⁴² Cadmium release from QDs can also occur through intracellular degradation.³² Release, however, can be mediated by humic acids, bovine serum albumin (cellular media component), oxalate, nitrilotriacetic acid, EDTA, citrate and cysteine which are presumed to protect QD surface sites from etching.⁴²

Effect of Metal Ions on Voltage-Gated Ion Channels

In order to predict the interaction of M+s (and potentially nanomaterials) with ion channels, two key factors must be considered: the enthalpy of hydration and hard-soft characteristics of M+s. Through solvation, water molecules form a shell around the ion. The enthalpy of hydration is indicative of the attraction of the M+ for oxygen groups and is consequently inversely proportional to the water substitution rate. Hydration energies are highest (meaning the ion is more

	Radius (pm)	Δh_{hyd} (kJ/mol)	Ligand Preference	
Target Ions				
Na ⁺	98	-405	TSYDENQ	
K ⁺	133	-321	TSYDENQ	
Ca ²⁺	106	-1592	TSYDENQ	
Metal ions				VGCC IC50 mM
Ba ²⁺	143	-1304		1.5
Sr ²⁺	127	-1445		2.6
Cd ²⁺	103	-1806		0.001
Co ²⁺	82	-2054	KRHWCM	0.06
Zn ²⁺	83	-2044	KRHWCM	0.03
Ni ²⁺	78	-2106	KRHWCM	1.04
Cu ²⁺	72	-2100	KRHWCM	1.04
Y ³⁺	106	-3620		0.001

Table 1.1 . Summary of Ionic Radii, Hydration Energies, Ligand Preferences and Effects on VGCC.

Target ions of VGICs: sodium, potassium and calcium provide a comparison for metal ions. Atomic radius is given in pm. Table highlights trends mentioned in the text. As charge is increased at constant radius, the enthalpy of hydration (ΔH_{hyd}) increases. For a given charge, as the radius decreases, ΔH_{hyd} increases. The higher the ΔH_{hyd} , the lower the rate at which dehydration occurs in the pore and is one factor contributing to ion permeation or pore blockage. Barium and strontium with lower ΔH_{hyd} are known to permeate VGCCs, whereas cadmium and yttrium block VGCCs. Moreover, cadmium and yttrium are the same size as calcium, suggesting the possibility of biomimicry. Ligand preference, refers to known preferred complexation ligands, in which the letters denote standard amino acids. Table adapted from ^{6, 13, 48}

hydrated) for small ions with large ionic charge (Mg^{2+} , Mn^{2+} , Ni^{2+} , Co^{2+} , Zn^{2+}).

This affects the metal interaction with ion channels as the solvated water molecules are replaced by dipolar groups of the channel inner pore and therefore influences whether an ion will permeate or block the channel ⁶⁶.

Additionally, hard-soft ionic categorizations influence ionic complexation. A hard metal preferably retains its valence electrons and is not easily polarized. Traditionally, hard ions are from the alkaline earth metals, lanthanoids and aluminum. They are small in size, high in charge and prefer to complex with hard bases such as oxygen (water) or fluoride through electrostatic interaction. In contrast, soft ions are transition metals such as Au^+ , Cu^+ , Ag^+ or Hg^+ . They are relatively large, easily polarized and prefer to complex with soft bases such as phosphorus, arsenic, nitrogen (amines, histidine) or sulfur (sulfhydryl, disulfide, thioether) through covalent interaction. The distinction between hard and soft is not well defined and some ions such as Zn^{2+} and Ni^{2+} fall in between. See Table 1.1 for a summary of ion radii, enthalpy of hydration and ligand preference ^{13, 66}. These characteristics influence the interaction of M^+ s released from nanomaterials with ion channels.

Pore block. VGICs are designed for high throughput transport of target ions. Ion selectivity is the function of the channel's selectivity filter. Through similarities in size and charge, it is possible for M^+ s to enter the pore through a type of biomimicry. In this way, M^+ s mimic target ions and hijack the machinery of the pore. Pore block refers to the entry and binding of M^+ s to the pore, resulting in decreased current. Current may decrease to such a degree that the channel is

effectively blocked. M+s may interact with the selectivity filter of the various channels in order to affect a pore-block mechanism. For voltage-gated calcium ion channels, four glutamate residues (EEEE) comprise the selectivity filter. Similarly, the selectivity filter of VGSC involves two regions: a ring of four amino acids (EEDD) in the outer vestibule of the pore, and an inner ring, also of four amino acids (DEKA). Amino acids (TVGYG) make up the selectivity filter of the VGKCs. Many ions released from common nanomaterials are effective voltage-gated channel blocking agents.

Altered Channel Dynamics. Metal ions can affect channel dynamics without ever entering the pore by altering the rates of activation or inactivation. There are three such mechanisms of M+ interaction with voltage-gated channels: charge screening, electrostatic modification of the voltage sensor and non-electrostatic binding effects^{3, 13}. Each of these methods may act alone or together to affect ion channel dynamics.

At rest, under physiological conditions, a negative membrane potential defines the extracellular space to be more positively charged than the intracellular space. When M+s are introduced to the system, the additional positive charge in the extracellular media may alter the membrane potential. The charge screening mechanism of M+ interaction with voltage-gated channels describes this phenomenon¹³. Since high concentrations of M+s are necessary to have an effect through charge screening alone, it seems an unlikely mechanism for nanomaterial interactions.

In the second mechanism, electrostatic modification of the voltage sensor, the binding of released M+s to the membrane surface fixes charges, increases the ionic concentration near the surface and therefore reduces membrane potential. The reduction in membrane potential affects the action of the voltage sensor¹³. The rate of channel opening subsequently decreases, and the rate of channel closure increases. In some cases, the action of the ion is dynamic and channel state specific. Zinc is believed to be attracted to the negatively charged component of the gating apparatus when the channel is at rest¹⁹. When the channel is activated, however, the positive charge of the voltage sensor prevents zinc binding. In this way, zinc decreases the rate of channel opening; however the rate of channel closure remains unaffected. Contrastingly, intracellular zinc does not affect opening but slows closing^{13, 19}.

Non-electrostatic binding effects is the third mechanism. Here, M+s bind close to the pore to affect gating in a non-electrostatic way. In general, the binding of the ion to a portion of the channel apparatus enables ion-mediated steric hindrance or mass effects that inhibit normal function of the channel¹³. The effect of M+s on channel gating is dependent on channel type, M+ type and concentration. While the aforementioned summarizes general mechanisms, exploration into the effect of specific M+s in a given system must be addressed in order to fully account for the ionic effects on gating.

Adsorption of Target Ions

Adsorption refers to the binding of small molecules, proteins or ions to material surfaces including nanomaterial surfaces. This effect can have a two-fold mode

of action to alter channel dynamics. In the first, target ions are chelated from the external solution and are no longer bioavailable for transport through the channels. In the second, M+s are adsorbed onto the material surface for later exposure.

Common chelators are BAPTA (calcium specific chelator) and EDTA (metal ion chelator). *In vitro*, NiO, ZnO, TiO₂, CeO₂ and Fe₂O₃ nanometal oxides significantly reduce calcium and phosphorus levels in the media. Sodium levels are unaffected²⁰. Carbon nanotubes can also be sorbents of target ions^{37, 37}. As the concentration of calcium ions outside the cell is roughly 1.2mM and the concentration inside the cell is 100nM, it is unlikely that nanomaterials, unless highly concentrated, would adsorb enough calcium to have an appreciable effect on VGCC function.

The second adsorption mechanism pertains to the adsorption of M+s onto the nanomaterial surface for exposure later on. The adsorption capacity of M+s to carbon nanomaterials follows $Pb^{2+} > Ni^{2+} > Zn^{2+} > Cu^{2+} > Cd^{2+}$. Adsorption is dependent on temperature and the acidity of the solution. The addition of function groups to the nanomaterial surface increases M+ adsorption capacity⁵⁷. As mentioned previously, certain M+s inhibit ion channel conductance and the conditions under which nanomaterials will adsorb and release M+s should be monitored.

Direct Particle-Protein Interactions

Some nanomaterials have been suggested to directly interact with ion channels. Many of the principles that apply to the interaction of M+s with ion channels and

adsorption mechanisms can be combined and extended to understand the potential for nanomaterials to directly interact with ion channels. Such interaction could include a physical occlusion of the pore or electrostatic alterations. The channel pore is on the scale of nanometers. QDs have been shown to enter the cylindrical cavity of proteins on the same size scale²³, and early work suggested that SWNTs physically occlude the VGKCs⁵¹. While the mode of action remains a mystery, more recent work has shown the non-ROS induced inhibition of VGKCs with carboxylated MWNTs of 40-50nm outside diameter⁶⁹.

Nanomaterials in media form aggregates¹⁶ dependent on ionic strength, surface charge, and surface coating.²⁵ Given that channel dimensions are fixed, agglomeration of nanomaterials increases the hydrodynamic radius of the material and consequently decreases the likelihood of physical interactions. Moreover, in media, nanomaterials are observed to adsorb proteins¹⁷ and ions⁵⁷ increasing the effective size even more. This suggests that if direct interactions are to occur, they would not be mediated by physical occlusion, but rather through electrostatic modification through coupling to the cell membrane⁹ or nanomaterial mediated steric hindrance of the area near ion channels.

Oxidative Stress

The generation of ROS by nanomaterials and the material features contributing to ROS, continues to be of debate. An increase in intracellular calcium, production of ROS and a decrease in mitochondrial membrane potential are characteristics of oxidative stress. In some cases cellular exposure to nanomaterials induces rises in intracellular calcium levels. Some studies have

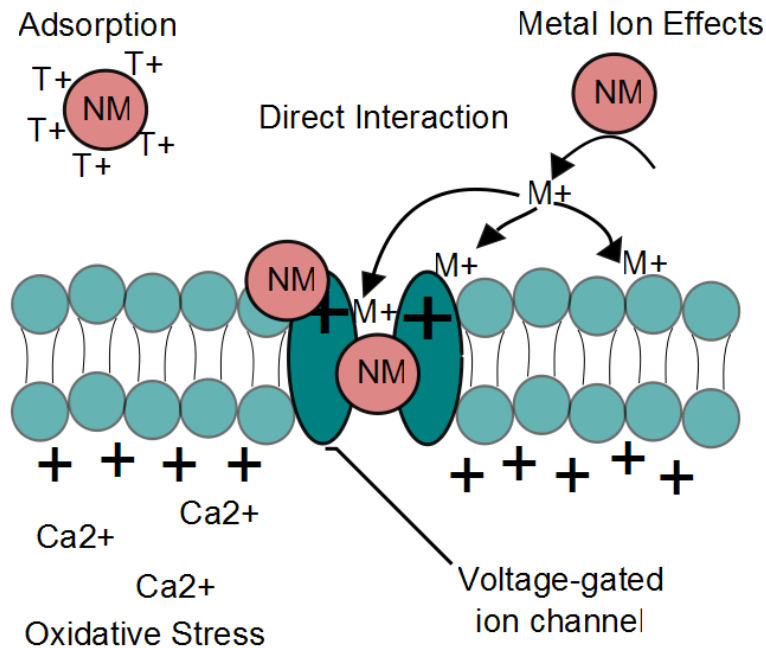


Figure 1.4 Summary of proposed mechanisms of nanomaterial interactions with voltage-gated ion channels.

The membrane above is depolarized and the channel is shown in the open conformation. Adsorption of target ions (T⁺) are rendered biologically unavailable for permeation through the pore due to adsorption onto nanomaterials (NMs). Direct Interaction: NMs interact directly with the pore and prevent the permeation of T⁺ through the pore, or bind to the protein complex, alter the structure and disable channel function. Metal ion effects: NMs release metal ions (M⁺) that enter the pore to affect inhibition, bind to channel components outside the pore to alter channel dynamics or locally concentrate near the membrane by binding to membrane proteins to affect membrane potential and thereby movement of the voltage sensor. Oxidative stress: The increase of cytosolic calcium associated with oxidative stress affects channel dynamics.

suggested ROS production upon exposure to nanomaterials results in altered channel function *in vitro*⁶⁴, whereas others observed a disconnect between the two^{16, 69}. This raises the possibility that nanomaterial induced ROS production

may contribute to alterations in ion channel function through downstream mechanisms; however, more research is needed.

Dielectrophoresis for Tissue Engineering of Pancreatic Islets

1.4 Diabetes

In general, diabetes is characterized by uncommonly high blood glucose levels (hyperglycemia) that can result in serious health complications such as kidney failure, heart disease, blindness and stroke. The metabolic consequences of chronic hyperglycemia can cause neuropathy; characterized by progressive axonal loss and manifested by somatic and autonomic neurophysiological abnormalities⁴⁹. Diagnosis usually occurs when hyperglycemic patients show clinical signs of excessive thirst, hunger and urination. The hyperglycemia is caused by abnormal insulin functionality resulting from either Type 1 or Type 2 diabetes or both. In Type 1 diabetes, the cells responsible for producing insulin, beta-cells in the islets of Langerhans of the pancreas, are destroyed or damaged by the body's autoimmune system. The destruction of the islets is comprehensive enough to significantly alter the levels of insulin produced to well below physiological levels. It is generally believed that Type 1 diabetes is triggered in genetically susceptible individuals through environmental cues². In Type 2 diabetes, the mechanism for releasing insulin into the blood is functional, however, tissues no longer respond to normal amounts of insulin. This type is usually observed in the obese or elderly.

According to the American Centers for Disease Control, 25.6 million people, or 11.3% of all Americans over 20 years of age or older have diabetes, and 1.9 million were newly diagnosed in 2010. The prevalence of Type 1 diabetes in children aged 0-10 years old is roughly 19.7 new cases per 100,000 people estimated between the years 2002 and 2005¹⁰. In Europe, it is predicted that if the present trend continues, the number of new cases of Type 1 diabetes in children under 5 will double between 2005 and 2020 and the prevalence of cases in children younger than 15 will rise by 70%⁵². Diabetes is the seventh leading cause of death in the United States, and the leading cause of kidney failure, non-traumatic limb amputation and new cases of blindness¹⁰. It additionally increases the risk of stroke and heart disease. Since the complications of the condition are so grave, and the rate of new cases is increasing globally, new and effective treatment options are necessary. The next section describes current treatment options.

Treatment Options

Insulin Shots

In Type 1 diabetes, autoimmune attack on beta-cell mass or insulin production, reduces insulin levels to a critical point at which the diabetic pathology is recognized. The first and simplest treatment strategy is to compensate for this loss of functionality by directly replacing insulin in the blood through injections. This procedure has been conducted since the 1920s and in ideal situations only results in a shortened life expectancy of roughly ten years⁶⁷. In 1993, the diabetes control and complications trial established that multiple daily

determinations of blood glucose levels through the finger stick, and combinations of daily injections of insulin, would be the standard of care for the management of Type 1 diabetes⁵⁸. This treatment is effective unless the patient has autonomic insufficiency, and consequently struggles with glycemic control which could potentially result in near fatal overdoses of insulin^{58, 67}. In these cases, whole pancreas transplantations are a viable option.

Stimulation of Insulin Secretion

Treatment with hormones that are observed to enhance insulin secretion from the remaining islets is presently under clinical investigation. Taken from Type 2 diabetes treatment options, it is observed that hormone, glucagons-like peptide-1 (GLP-1) and analogs of this hormone, stimulate secretion in the remaining beta-cells. However, the effect on beta-cell population or immune response is debatable⁶⁷.

Whole Pancreas Transplantation

While the multiple daily determinations of blood-glucose levels through the finger stick in combination with daily injections of insulin is the standard of care for diabetes, this method is not effective for individuals who have autonomic insufficiency. In 2003, the American Diabetes Association encouraged pancreatic tissue transplantation for patients with unacceptably poor glycemic control. In most countries, pancreas transplantation is the only accepted method available to achieve normal glycemic levels^{18, 58, 67}. Moreover, pancreas transplantation has been observed to stabilize diabetic complications such as motor, sensory and autonomic neuropathy⁴⁹. As with any transplantation, the

procedure is invasive, has inherent risk of procedural complications and, once performed, the patient must maintain a regimen of immunosuppressants for the remainder of their lives. However, quality-of-life studies suggest patients feel that the freedom from daily insulin injections outweighs the burden of transplantation and accompanying immunosuppression⁵⁸. A similar, however less invasive procedure, is islet transplantation.

Islet Transplantation

Insulin producing beta-cells can be isolated from the pancreatic tissue of deceased donors and then transplanted into patients with Type 1 diabetes to restore normal glycemia. This procedure is less demanding on the patient as it does not involve major surgery, permits a lesser degree of immunosuppression and is potentially less expensive⁵⁸. It is estimated that roughly 400 patients have received isolated islets between the years 1999 and 2009¹⁸. Unfortunately, in a study following patients receiving isolated islet transplants, it was concluded that by 5 years post-transplantation, less than 10% remained insulin independent⁵⁹. However, the majority of the patients have less frequent hypoglycemia and require less insulin¹⁸. In order to obtain the 12,000 islets per kilogram body weight required to restore normal glycemic levels⁶⁰, patients need to receive islets from roughly 2.1 donors⁶¹. As multiple donors are needed, immune effects are controlled with immunosuppressors; however, the immunosuppressors are believed to negatively effect beta-cell functionality⁶⁷. This is believed to be the root of the decreased islet functionality observed in the study. For this reason, the current research involves suppressing the immunological response. The

original protocol has been modified with new immunosuppressors and is currently in clinical trials⁶⁷.

Once protocols can be developed to protect insulin producing cells once they are transplanted into the body, the main limitation of this method is the availability of donors^{18, 58, 67}. For this reason, a renewable source of islets is required. In Chapter 2, we take the initial steps in demonstrating the electromagnetic control of insulin-releasing cells in vitro through dielectrophoresis. The long-term goal of the project is to develop insulin producing pseudoislets using this method. The next section describes the islet and the use of dielectrophoresis as a method of tissue engineering.

1.5 Dielectrophoresis for Insulin-Secreting Cells

In the United States, 25.6 million people have diabetes (Type 1 diabetes or Type 2 diabetes)¹⁰, and the country produces only about 8,000 organ donors each year¹⁸. As mentioned previously, approximately half of the isolation efforts yield islets suitable for transplant⁶¹ and consequently, recipients usually require islets from multiple donors. Therefore, the effective donor pool for pancreatic islets is very small and can only treat a limited number of patients. According to Harlan et al, efforts to expand the pancreas donor pool, improve isolation techniques from each pancreas, and decrease a recipient's islet requirements, even when combined, will only marginally improve the current disparity between islet supply and potential recipients¹⁸. For this reason research is being conducted to attempt to develop a renewable source of insulin secreting structures. In this

section I describe dielectrophoresis as a technique that might be useful for this endeavor.

Islets of Langerhans

The islets of Langerhans are named after Paul Langerhans, the scientist who identified them in 1869. In mammals, islets are 100-200 μm in dimension²⁶ and make up approximately 2-3% of total pancreatic volume⁵⁸. Given the relatively static islet size, as the volumetric size of the pancreas is proportional to the size of the mammal, the number of islets in the pancreas is also proportional to mammal size²⁶.

As shown in Figure 1.5, the islets of Langerhans contain five endocrine cell types, alpha, beta, gamma, delta and epsilon cells producing the hormones glucagon, insulin, pancreatic polypeptide, somatostatin and ghrelin respectively¹². There are differences between species with regard to islet archetype. In rodents, beta cells form the core of the islet with alpha and delta cells localized around the periphery; in humans, endocrine cells are interspersed throughout the islet³¹. Recent studies have focused on determining comparative percentages of different cell types in different species with interest in developing a structure-function relationship. As this work is fairly recent, there is still some discrepancy between studies. However, beta cells are believed to comprise roughly 60-80% of the islet^{26, 31}.

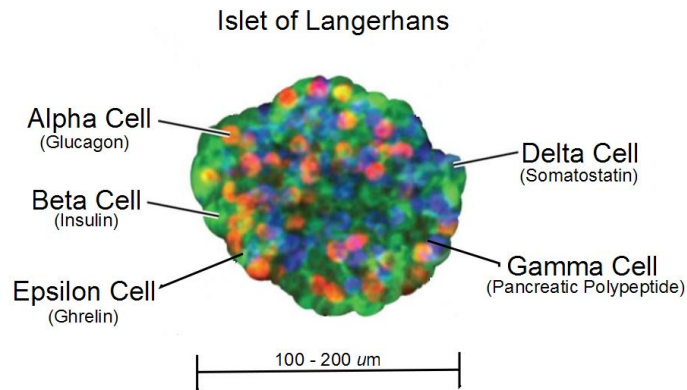


Figure 1.5 Diagram of typical Islet of Langerhans.

Diagram of islet of Langerhans highlighting the typical elliptical morphology of size 100-200 μm. Islets contain five types of endocrine cells: alpha, beta, delta, epsilon and gamma cells, releasing glucagon, insulin, somatostatin, ghrelin and pancreatic polypeptide hormones respectively. In humans, these cell types are interspersed throughout the islet. Figure adapted from Harlan et al¹⁸

The alpha and beta cells of the islet are exclusively sensitive to glucose.

The sole action of insulin, produced by beta cells, is to promote glucose into tissues and decrease gluconeogenesis. Glucagon, produced by alpha cells, stimulates glycogenolysis when hypoglycemia threatens. Glucose stimulates beta cells and inhibits alpha cells⁵⁸. In this way normal glycemic levels are maintained. Gap junctions exist between cells of the islet. It has been observed that coupled beta cells secrete insulin more effectively than single beta cells; moreover, calcium dependent oscillatory action potential patterns in islets produce a complimentary bursting pattern of insulin from beta cells²⁶. This mechanism, as well as the interplay between hormones secreted from islets, is a recent topic in diabetes research. The development of pseudoislets will provide

a source of transplantable islets. This will potentially decrease the number of required transplants (stemming from the current need of multiple donors to attain the required number of islets) to a one-time transplant of the necessary number of islets. This will decrease the use of post-transplant immunosuppression treatments which will increase the long-term viability and effectiveness of implanted islets. Moreover, pseudoislets will provide a three-dimensional model system for studying synchronous electrical activity, formation of gap junctions in three-dimensional tissues, and the testing of new diabetic treatment strategies. The next section describes the potential for dielectrophoresis to enable the tissue engineering of three dimensional pseudoislets.

Tissue Engineering with Dielectrophoresis

Availability of organs is a significant hurdle for the treatment of patients in need of transplants. For this reason, the nearly 20 year-old field of tissue engineering, or the ex vivo generation of tissues for in vivo use, has seen extensive growth in recent years. Conventional methods require the generation of scaffolds composed of biocompatible and ideally biodegradable materials, the seeding of select cells onto the scaffolds and subsequent culturing in a bioreactor. This is very effective for planar tissues such as skin, bone, cornea and cartilage; however, it is significantly more challenging for three-dimensional tissues that are composed of multiple cell types arranged in multiple distinct layers. Moreover, establishing appropriate cell-to-cell interactions physiologically present in functioning tissue, is critical to the bioengineered tissue's end-functionality in

vivo. There are two overarching methods used to generate tissues ex vivo: cell patterning and applied force.

Cell patterning applies external guidance cues to arrange cells into desired patterns mimicking physiological tissues. This technique relies on the surface chemistry of the substrate and the biological interactions known to exist between select cell types and a given substrate. The effectiveness of this method therefore, relies on the natural cell adhesion process and is consequently slow, unregulatable and diverse from cell type to cell type³³ making it somewhat limited in the number of cells that can be patterned in a given experiment.

The use of force to actively direct cells to desired locations can be accomplished using magnetic, optical, or fluidic manipulation techniques. The magnitude of these optical forces is generally insufficient to firmly trap individual biological particles alone, and relies on the trapping of microscopic dielectric objects, such as micron-sized polystyrene beads, which can be biochemically linked to the cells of interest⁴⁶. In this way, the beads serve as handles to a biological system, allowing its manipulation inside a sample chamber. Other techniques involve the attachment of magnetic particles to cells of interest and the use of magnetic fields to direct the patterning of cells. As with the optical tweezer methods, this requires additional surface modification of the cells.

Dielectrophoresis is the lateral motion imparted on uncharged particles as a result of polarization induced by non-uniform electric fields⁵⁵. Several studies have demonstrated that dielectrophoresis can be used to 'trap' and move uncharged cells through non-uniform electric field gradients³³. Unlike the

previous techniques that are limited in their applicability in the number of cell types able to be manipulated, or that require cellular surface modification prior to patterning, dielectrophoresis can be used on many cell types at once without pre-modification. This makes it an interesting technique for the development of an islet of Langerhans, which as mentioned previously, incorporates at least five different cell types into a specialized tissue. The next section describes an overview of the principles underlying dielectrophoresis.

Dielectrophoresis Principles

Dielectrophoresis is the lateral motion imparted on uncharged particles as a result of polarization induced by non-uniform electric fields⁵⁵. The underlying fundamentals involved in this technique are well described in the literature^{1, 22, 27, 47, 54, 55} and rely on understanding particle polarizability and Coulombic force.

Polarization

Polarization is the process of alignment of charge on a body such that the positive and negative bound charges move in an electric field, resulting in the centers of charge aligning along the field lines²². For a particle whose positive and negative regions share a common average position, in the absence of an external electric field, the particle is unpolarized. In the presence of an applied electric field, the particle will develop an 'induced' dipole. An induced dipole is not a permanent dipole (such as the case for water). After the electric field is removed, and induced dipole requires time for charges to return to their neutral conformation. The time it takes for a dipole to form and deform is known as the relaxation time.

Permittivity is a measure of the effect of charge redistribution within a material. The greater the permittivity, the greater the effect of charge redistribution, and the longer it takes the charge to dissipate. Most materials are not strictly capacitors or conductors but, rather, have a quality of each described by the complex permittivity (ϵ^*)^{22, 28}.

$$\epsilon^* = \epsilon_0 \epsilon_R - j \frac{\sigma}{\omega} \quad (1)^{22, 28, 55}$$

Where ϵ_0 is the permittivity of free space, ϵ_R is the relative permittivity of the material, j is the imaginary number ($\sqrt{-1}$), σ is the conductivity of the material (S/m) and ω is the frequency of the electric field applied. The importance of this equation is that it demonstrates that complex permittivities are frequency dependent. As the frequency increases, the imaginary part of Eq 1 tends towards zero and the complex permittivity is dominated by the relative permittivity or polarizability. At low frequencies, the imaginary part dominates, indicating the dependence of the complex permittivity on conductivity.

For an unpolarized particle in media within an electric field, the shift in complex permittivity dependence on polarization versus conductivity, is influenced by shifts that occur within the particle versus those that occur at the particle interface. Briefly, Debye relaxation describes shifts that occur within the particle, namely the inability of a dipole to reorient in time with the applied field. The reason for this, is the time necessary for an induced dipole to form in relation to the cycle frequency of the applied field. For higher frequencies, induced dipoles do not have time to form and as described in Eq 1, the transfer of charge by capacitive coupling does not occur. Shifts that occur at the particle interface

with the medium can be described by Maxwell-Wagner interfacial polarization. If the two materials transfer charge in different ways (based on Eq 1), ie dependent on conduction versus dependent on polarizability, then charge may build up at the interface of the two, creating an interfacial dipole.

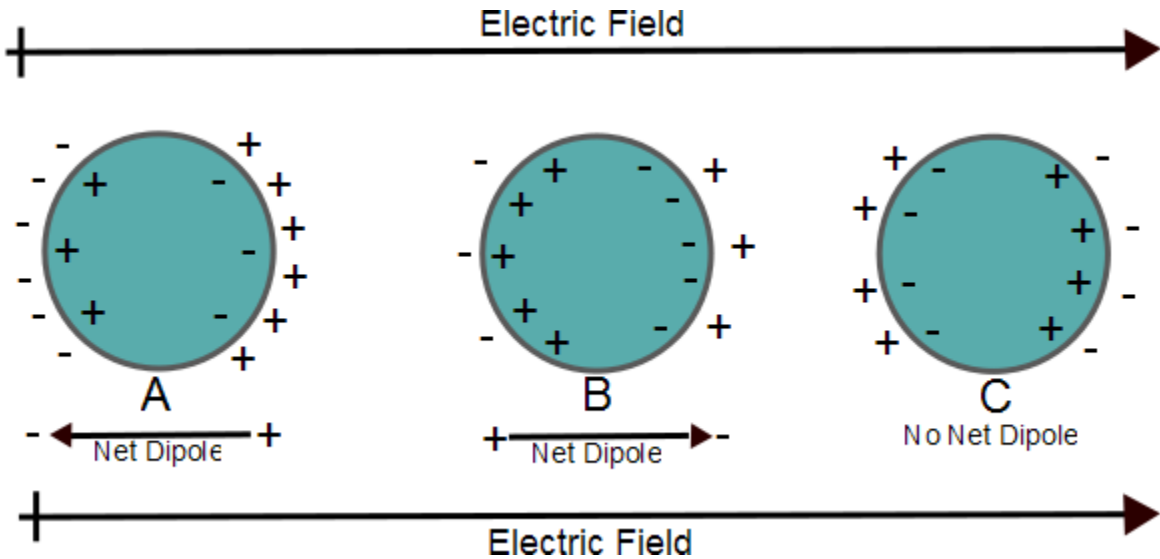


Figure 1.6 Dipole effects on a sphere suspended in media exposed to an electric field.

The net dipole on the particle depends on the relative conductance and capacitance of both the particle and the media in the presence of an electric field; leading to a net dipole across the particle. A) Particle is more polarizable than the media; B) Particle is less polarizable than the media; C) Particle and media equally polarizable. Figure adapted from Hughes 2003²²

When a polarizable particle is within an electric field, charge will build at the interface of the particle with its surrounding media. In order to determine the behavior of the particle within the field, the overall dipole (m) of the particle must be determined. For a spherical particle the dipole, m , is given by Eq 2.

$$m = 4\pi r^3 \epsilon_0 \left(\frac{\epsilon_p^* - \epsilon_m^*}{\epsilon_p^* - 2\epsilon_m^*} \right) E \quad (2)^{22, 55}$$

Where ϵ^* is the complex permittivity of the particle (subscript p), media (subscript m) and free space (0). r is the radius of the sphere. The bracketed

section is the Clausius-Mossotti factor. As complex permittivities depend on frequency of the applied electric field, the dipole of the orientation can therefore shift as a function of frequency.

Figure 1.6 visually describes the process by which the dipole orientation, described in Eq 2 occurs. In Figure 1.6A the particle is more polarizable than the media, suggesting the complex permittivity (Eq 1) is dependent on the conductivity term. Since the particle is acting as a conductor, the media is acting as a capacitor. Consequently, charge will build-up on the media side of the interface. Given the relative charge densities shown in Figure 1.6A, the charge build-up is occurring on the surface of the particle and is greater than within the particle. Therefore, the net dipole for the particle (including surface charges) will be in the same direction as the maximum charge build-up. In this case, the dipole is counter to the direction of the electric field. If the media is more conductive than the particle, as is the case in Figure 1.6B, charges will accumulate within the particle at the interface and the net dipole will be in the same direction as the electric field. In Figure 1.6C, the permittivities of the media and the particle are the same. As a result there is no charge build-up and there is consequently no net dipole.

This section describes the theory underlying particle polarization. Once the particle is polarized by an external electric field, for dielectrophoresis to take place, the field will apply a force on the particle.

Dielectrophoretic Force

The attractive force between different charges and the repulsive force between like charges can be described by Coulomb's Law. This law states that the direction and magnitude of the force between charges is proportional to the magnitude of the product of the charges and inversely proportional to the square of the distance between them. If a particle is within an electrical field, a dipole is induced within the particle and charges build-up as previously described. If the electric field is uniform, then the Coulomb force applied to charges on either side of the particle is equal and opposite and consequently the particle experiences no net force. If however, the electric field is non-uniform, then the force on the particle is not uniform and there will consequently be a net force in a given direction. The force applied to a polarizable particle in a non-uniform electric field is the dielectrophoretic force. For a spherical particle, the dielectrophoretic force (F_{DEP}) is described by the following equation.

$$F_{DEP} = 2\pi\epsilon_0\epsilon_r r^3 \left(\frac{\epsilon_p^* - \epsilon_m^*}{\epsilon_p^* + 2\epsilon_m^*} \right) \nabla E^2 \quad (3)^{22, 55}$$

Again, the bracketed region is the Clausius-Mossotti factor which is dependent on the frequency of the electric field. The factor can be positive or negative. If the factor is positive, the dielectrophoretic force will be positive and the force will act towards increasing electric field gradient. This is called positive DEP. If the factor is negative, then the force will act to repel the particle from regions of high electric field gradient. This is called negative DEP. The use of dielectrophoresis as a means of tissue engineering will then most likely depend on negative

dielectrophoresis to corral the cells into aggregates which can then form intracellular connections³³.

Electrorotation

If the polarizable particle is in a rotating field, the field will induce a dipole as before; however, it will also cause the particle to rotate. Take for example, Figure 1.7, four electrodes exhibiting an alternating current with a phase shift of 90° , as the field rotates, the dipole of the particle will rotate to avoid repulsion from like-charges.

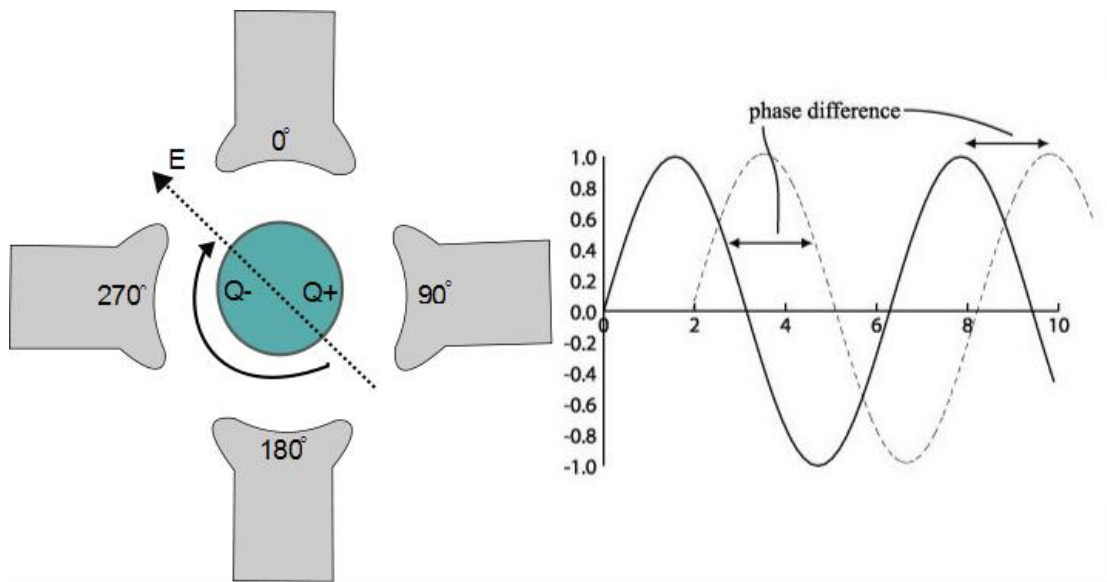


Figure 1.7 Electrorotation

(Left) Induced dipoles require time to form and dissipate, called the relaxation time. If the relaxation time causes the dipole to lag behind the rotation of the electric field, the particle will experience a torque. (Right) Each electrode is receiving an AC current phase shifted by 90° . The associated charge on the electrode corresponds to the amplitude of Y-axis of the respective sine wave. Left figure adapted from Hughes 2003²²

Just as with dielectrophoresis, the sign of the Clausius-Mossotti factor influences the direction of rotation. When the factor is positive, the particle rotates in a

direction opposite to the direction of rotation of the electric field.

Correspondingly, if the sign is negative, the particle will rotate with the field⁵⁵. A particle can experience electrorotation and dielectrophoresis simultaneously.

Pearling

When a polarizable particle is in an electric field, if the particle is conductive (based on Eq 1) then the induced dipole will alter the electric field lines. If the induced dipole is in the same direction as the system electric field, the particle

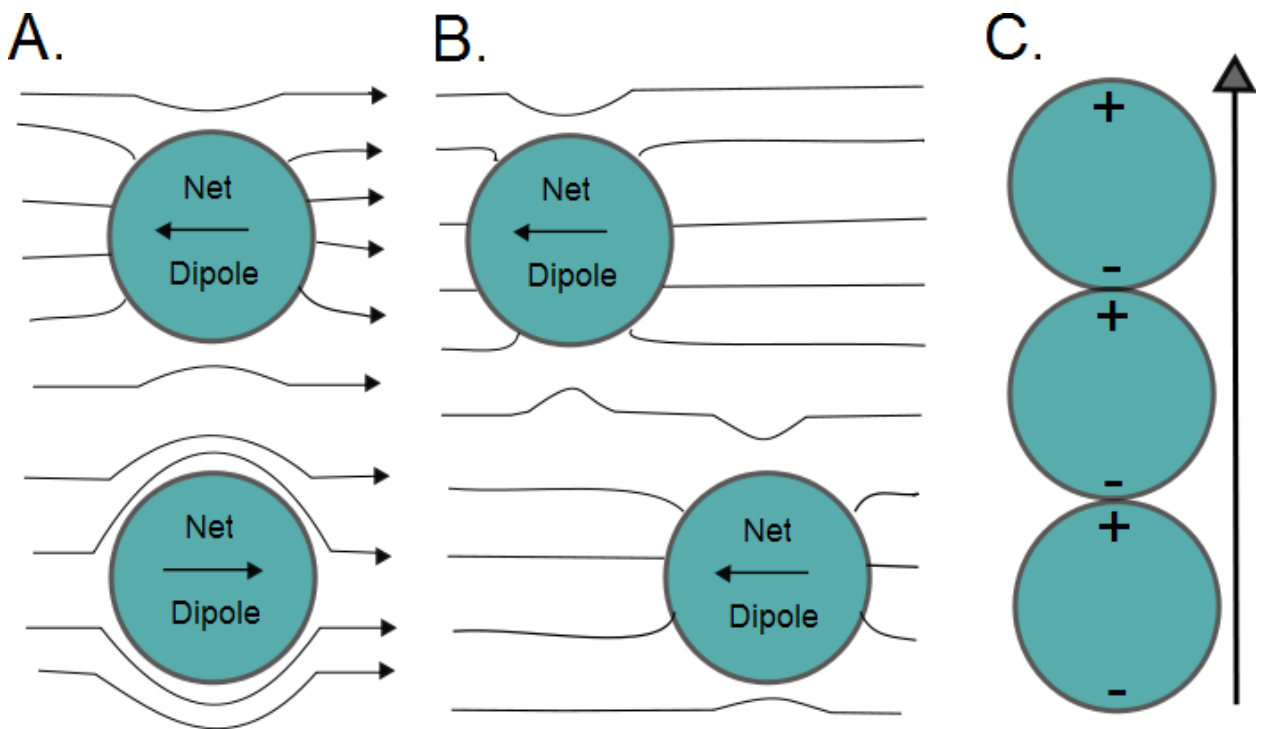


Figure 1.8 Dielectrophoretic Pearling

A. The net dipole over a particle creates its own electric field. (Top) When the net dipole is in the opposite direction of the overall electric field, the particle is conductive and the electric field lines bend in towards the particle. (Bottom) When the net dipole is in the same direction as the electric field, the particle is insulating and the electric field lines wrap around the particle. B. When two conducting particles are close enough together that their induced electric fields interact, dielectrophoretic force moves the particles together to form a pearl chain. C. Pearl chain conformation in which particle dipoles align in the same direction to allow Coulombic attraction. Pearling occurs in both positive and negative dielectrophoresis. Figures adapted from Hughes 2003²².

is insulating and the field lines will wrap around the particle (Figure 1.8A). If conductive particles are close enough such that their induced electric fields interact, dielectric force will pull the particles towards each other (Figure 1.8B). This causes the particles to align in a “Pearl Chain” conformation (Figure 1.8C). The particles align in the chain such that Coulombic attraction between charges of opposite sign exists between each pearl of the chain. The phenomena exists for both positive and negative dielectrophoresis.

Dielectrophoresis for Pancreatic Islets

The technique described in the previous section is a very powerful tool to control the orientation and motion of cells, to non-invasively determine the electrical properties of the cells, and to sort cells based on dielectric properties. The application of dielectrophoresis to tissue engineering is novel; however it is very well suited for the development of pseudoislets. First of all, while the explanation given is provided in planar 2D, the same phenomena should occur if a 3D electrical field is applied. This would enable the development of three dimensional structures. Moreover, as mentioned in the previous section, human islets do not have a well defined overall tissue structure. That is to say, alpha, beta, delta, gamma and epsilon cells are interdispersed within the islet. While it would be possible to generate shells of specific cell types, this lack of specificity makes the initial experimental burden dependent on obtaining the correct concentration of cell type and not necessarily on ensuring the cells are present in the correct ‘shell’. Once the cells are aggregated, dielectrophoresis could again

prove beneficial as the technique may be able to detect, through electrokinetic data, the development of intercellular gap-junctions and insulin bursting mechanisms.

Before the technique can be used in three dimensions with multiple cell types, basic studies on the electrokinetics of specific cell types with a planar dielectrophoretic chamber are necessary. In particular, the knowledge of a cell's electrokinetic behavior in electrolytes of known conductivity is necessary to predict the conditions necessary to generate either positive or negative dielectrophoretic movements of the cells. The research presented in Chapter 2 describes these fundamental electrokinetic measurements for INS cells (insulin secreting cells) and pancreatic beta cells in electrolytes of known conductivity in a dielectrophoretic chamber.

1.6 References

1. Arnold, W.M. and U. Zimmermann. 1988. Electro-rotation: development of a technique for dielectric measurements on individual cells and particles. *Journal of Electrostatics*. 21: 2-3 151-191.
2. Atkinson, M.A. and G.S. Eisenbarth. 2001. Type 1 diabetes: new perspectives on disease pathogenesis and treatment. *The Lancet*. 358: 9277 221-229.
3. Ballatori, N. 2002. Transport of Toxic Metals by Molecular Mimicry. *Environmental Health Perspectives*. 110: 5 689-694.
4. Belyanskaya, L. and S. Weigel and C. Hirsch and U. Tobler and H.F. Krug and P. Wick. 2009. Effects of carbon nanotubes on primary neurons and glial cells. *Neurotoxicology*. 30: 702-711.
5. Börjesson, S.I. and F. Elinder. 2008. Structure, Function, and Modification of the Sensor in Voltage-Gated Ion Channels. *Cell Biochemistry and Biophysics*. 52: 3 149-174.
6. Burgess J. 1978. *Metal Ions in Solution*. Ellis Horwood,
7. Catterall, W.A. 2000. Structure and regulation of voltage-gated calcium channels. *Annual Review of Cell Developmental Biology*. 16: 521-555.
8. Catterall, W.A. and A.P. Few. 2008. Calcium channel regulation and presynaptic plasticity. *Neuron*. 59: 6 882-901.
9. Cellot, G. and E. Cilia and S. Cipollone and V. Rancic and A. Sucapane and S. Giordani and L. Gambazzi and H. Markram and M. Grandolfo and D. Scaini and F. Gelain and L. Casalis and M. Prato and M. Giugliano and L. Ballerini. 2008. Carbon Nanotubes might improve neuronal performance by favouring electrical shortcuts. *Nature Nanotechnology*. 4: 126-133.
10. Centers for Disease Control and Prevention. 2011. National diabetes fact sheet: national estimates and general information on diabetes and prediabetes in the United States, 2011. Department of Health and Human Services, Centers for Disease Control and Prevention,

11. Donaldson, K. and R. Aitken and L. Tran and V. Stone and R. Duffin and G. Forrest and A. Alexander. 2006. Carbon Nanotubes: A Review of Their Properties in Relation to Pulmonary Toxicology and Workplace Safety. *Toxicological Sciences*. 92: 1 5-22.
12. Eberhard, D. and M. Kragl and E. Lammert. 2010. 'Giving and taking': endothelial and [beta]-cells in the islets of Langerhans. *Trends in Endocrinology & Metabolism*. 21: 8 457-463.
13. Elinder, F. and P. Århem. 2004. Metal ion effects on ion channel gating. *Quarterly Reviews of Biophysics*. 36: 4 373-427.
14. Elinder, F. and J. Nilsson and P. Århem. 2007. On the opening of voltage-gated ion channels. *Physiology and Behavior*. 92: 1-7.
15. Gabay, T. and E. Jakobs and E. Ben-Jacob and Y. Hanein. 2005. Engineered self-organization of neural networks using carbon nanotube clusters. *Physica A-Statistical Mechanics and Its Applications*. 350: 2-4 611-621.
16. Gramowski, A. and J. Flossdorf and K. Bhattacharya and L. Jonas and M. Lantow and Q. Rahman and D. Schiffmann and D.G. Weiss and E. Dopp. 2010. Nanoparticles Induce Changes of the Electrical Activity of Neuronal Networks on Microelectrode Array Neurochips. *Environmental Health Perspectives*. 118: 10 1363-1369.
17. Guo, L. and A. Von Dem Bussche and M. Beuchner and A. Yan and A.B. Kane and R.H. Hurt. 2008. Adsorption of essential micronutrients by carbon nanotubes and the implications for nanotoxicity testing. *Small*. 4: 6 721-727.
18. Harlan, D.M. and N.S. Kenyon and O. Korsgren and B.O. Roep and for the Immunology of Diabetes Society. 2009. Current Advances and Travails in Islet Transplantation. *Diabetes*. 58: 10 2175-2184.
19. Hille B. 2001. *Ion Channels of Excitable Membranes*. Sinauer Associates, Inc., Sunderland, MA USA.
20. Horie, M. and K. Nishio and K. Fujita and S. Endoh and A. Miyauchi and Y. Saito and H. Iwahashi and K. Yamamoto and H. Murayama and H.

- Nakano and N. Nanashima and E. Niki and Y. Yoshida. 2009. Protein Adsorption of Ultrafine Metal Oxide and Its Influence on Cytotoxicity toward Cultured Cells. *Chemical Research in Toxicology*. 22: 543-553.
21. Hu, H. and Y. Ni and V. Montana and R.C. Haddon and V. Parpura. 2004. Chemically Functionalized Carbon Nanotubes as Substrates for Neuronal Growth. *Nano Letters*. 4: 3 507-511.
 22. Hughes, M.P. 2003. *Nanoelectromechanics in Engineering and Biology*.
 23. Ishii, D. and K. Kinbara and Y. Ishida and N. Ishii and M. Okochi and M. Yohda and T. Aida. 2003. Chaperonin-mediated stabilization and ATP-triggered release of semiconductor nanoparticles. *Nature*. 423: 628-632.
 24. Jasieniak, J. and P. Mulvaney. 2007. From Cd-Rich to Se-Rich Γ the Manipulation of CdSe Nanocrystal Surface Stoichiometry. *Journal of the American Chemical Society*. 129: 10 2841-2848.
 25. Jiang, J. and G. Oberdörster and P. Biswas. 2009. Characterization of size, surface charge and agglomeration state of nanoparticle dispersions for toxicological studies. *Journal of Nanoparticle Research*. 11: 77-89.
 26. Jo, J. and M.Y. Choi and D.S. Koh. 2007. Size Distribution of Mouse Langerhans Islets. *Biophysical Journal*. 93: 8 2655-2666.
 27. Jones T.B. 1995. *Electromechanics of particles*. Cambridge University Press,
 28. Jones T.B. 1995. *Electromechanics of Particles*. Cambridge University Press,
 29. Kagan, V.E. and Y.Y. Tyurina and V.A. Tyurin and N.V. Konduru and A.I. Potapovich and A.N. Osipov and E.R. Kisin and D. Schegler-Berry and R. Mercer and V. Castranova and A.A. Shvedova. 2006. Direct and indirect effects of single walled carbon nanotubes on RAW 264.7 macrophages: Role of iron. *Toxicology Letters*. 165: 88-100.

30. Keefer, E.W. and B.R. Botterman and M.I. Romero and A.F. Rossi and G.W. Gross. 2008. Carbon nanotube coating improves neuronal recordings. *Nature Nanotechnology*. 3: 434-439.
31. Kim, A. and K. Miller and J. Jo and G. Kilimnik and P. Wojcik and M. Hara. 2009. Islet architecture: A comparative study. *Islets*. 1: 2 129-136.
32. Kirchner, C. and T. Liedl and S. Kudera and T. Pellegrino and A. Muñoz Javier and H.E. Gaub and S. Stölzle and N. Fertig and W.J. Parak. 2005. Cytotoxicity of Colloidal CdSe and CdSe/ZnS Nanoparticles. *Nano Letters*. 5: 2 331-338.
33. Lin, R.Z. and C.T. Ho and C.H. Liu and H.Y. Chang. 2006. Dielectrophoresis based-cell patterning for tissue engineering. *Biotechnology Journal*. 1: 9 949-957.
34. Liopo, A.V. and M.P. Stewart and J. Hudson and J.M. Tour and T.C. Pappas. 2006. Biocompatibility of Native and Functionalized Single-Walled Carbon Nanotubes for Neuronal Interface. *Journal of Nanoscience and Nanotechnology*. 6: 1365-1374.
35. Liu, J. and R.H. Hurt. 2010. Ion Release Kinetics and Particle Persistence in Aqueous Nano-Silver Colloids. *Environmental Science & Technology*. 44: 6 2169-2175.
36. Liu, J. and D.A. Sonshine and S. Shervanti and R.H. Hurt. 2010. Controlled Release of Biologically Active Silver from Nanosilver Surfaces. *ACS Nano*. In Press:
37. Liu, X. and L. Guo and D. Morris and A.B. Kane and R.H. Hurt. 2008. Targeted Removal of Bioavailable Metal as a Detoxification Strategy for Carbon Nanotubes. *Carbon*. 43: 3 489-500.
38. Liu, X. and V. Gurel and D. Morris and D.W. Murray and A. Zhitkovich and A.B. Kane and R.H. Hurt. 2007. Bioavailability of Nickel in Single-Wall Carbon Nanotubes. *Advanced Materials*. 19 2790-2796.
39. Liu, Z. and G. Ren and T. Zhang and Z. Yang. 2009. Action potential changes associated with the inhibitory effects on voltage-gated sodium

current of hippocampal CA1 neurons by silver nanoparticles. *Toxicology*. 264: 3 179-184.

40. Lovat, V. and D. Pantarotto and L. Lagostena and B. Cacciari and M. Grandolfo and M. Righi and G. Spalluto and M. Prato and L. Ballerini. 2005. Carbon Nanotube Substrates Boost Neuronal Electrical Signaling. *Nano Letters*. 5: 6 1107-1110.
41. Lubick, N. 2008. Nanosilver toxicity: ions, nanoparticles or both? *Environmental Science & Technology*. 42: 23 8617-8617.
42. Mahendra, S. and H. Zhu and V.L. Colvin and P. Alvarez. 2008. Quantum Dot Weathering Results in Microbial Toxicity. *Environmental Health Perspectives*. 42: 9424-9430.
43. Matsumoto, K. and C. Sato and Y. Naka and A. Kitazawa and R.L.D. Whitby and N. Shimizu. 2007. Neurite outgrowths of neurons with neurotrophin-coated carbon nanotubes. *Journal of Bioscience and Bioengineering*. 103: 3 216-220.
44. Mattson, M.P. and R.C. Haddon and A.M. Rao. 2000. Molecular Functionalization of Carbon Nanotubes and Use as Substrates for Neuronal Growth. *Journal of Molecular Neuroscience*. 14: 175-182.
45. Mazzatenta, A. and M. Giugliano and S. Campidelli and L. Gambazzi and L. Businaro and H. Markram and M. Prato and L. Ballerini. 2008. Interfacing Neurons with Carbon Nanotubes: Electrical Signal Transfer and Synaptic Stimulation in Cultured Brain Circuits. *Journal of Neuroscience*. 27: 26 6931-6936.
46. Moffitt, J.R. and Y.R. Chemla and S.B. Smith and C. Bustamante. 2008. Recent Advances in Optical Tweezers. *Annu.Rev.Biochem*. 77: 1 205-228.
47. Morgan H. and N.G. Green 2003. AC electrokinetics: colloids and nanoparticles. Baldock : Research Studies Press,
48. Nachshen, D.A. 1984. Selectivity of the Ca Binding Site in Synaptosome Ca Channels. *Journal of General Physiology*. 83: 941-967.

49. Navarro, X. and D.E.R. Sutherland and W.R. Kennedy. 1997. Long-term effects of pancreatic transplantation on diabetic neuropathy. *Ann Neurol.* 42: 5 727-736.
50. Ni, Y. and H. Hu and E.B. Malarkey and B. Zhao and V. Montana and R.C. Haddon and V. Parpura. 2005. Chemically Functionalized Water Soluble Single-Walled Carbon Nanotubes Modulate Neurite Outgrowth. *Journal of Nanoscience and Nanotechnology.* 5: 1707-1712.
51. Park, K.H. and M. Chhowalla and Z. Iqbal and F. Sesti. 2003. Single-walled Carbon Nanotubes are a New Class of Ion Channel Blockers. *Journal of Biological Chemistry.* 278: 50 50212-50216.
52. Patterson, C.C. and G.G. Dahlquist and E. Gynrns and A. Green and G. Soltθsz. 2009. Incidence trends for childhood type 1 diabetes in Europe during 1989-2003 and predicted new cases 2005-20: a multicentre prospective registration study. *The Lancet.* 373: 9680 2027-2033.
53. Pedro, G.-G. and E.W. Keefer and F. Yang and M. Zhang and S. Fang and A.A. Zakhidov and R.H. Baughman and M.I. Romero. 2007. Robust cell migration and neuronal growth on pristine carbon nanotube sheets and yarns. *Journal of Biomaterials Science, Polymer Edition.* 18: 1245-1261.
54. Pethig, R. Cell physiometry tools based on dielectrophoresis. pp. 103-126. *In: M. Ozkan and M.J.Heller. [eds.] 2005. **BioMEMS and Biomedical Nanotechnology.** Springer Science,*
55. Pohl H.A. 1978. Dielectrophoresis: the behavior of neutral matter in nonuniform electric fields. Cambridge University Press,
56. Pulskamp, K. and S. Diabaté and H.F. Krug. 2007. Carbon Nanotubes show no sign of acute toxicity but induce intracellular reactive oxygen species in dependence on contaminants. *Toxicology Letters.* 168: 58-74.
57. Rao, G.P. and C. Lu and F. Su. 2007. Sorption of divalent metal ions from aqueous solution by carbon nanotubes: A review. *Separation and Purification Technology.* 58: 1 224-231.

58. Robertson, R.P. 2004. Islet Transplantation as a Treatment for Diabetes A Work in Progress. *New England Journal of Medicine*. 350: 7 694-705.
59. Ryan, E.A. and B.W. Paty and P.A. Senior and D. Bigam and E. Alfadhli and N.M. Kneteman and J.R.T. Lakey and A.M.J. Shapiro. 2005. Five-Year Follow-Up After Clinical Islet Transplantation. *Diabetes*. 54: 7 2060-2069.
60. Shapiro, A.M.J. and J.R.T. Lakey and E.A. Ryan and G.S. Korbitt and E. Toth and G. Warnock and N. Kneteman and R. Rajotte and V. Rancic. 2000. Islet Transplantation in Seven Patients with Type 1 Diabetes Mellitus Using a Glucocorticoid-Free Immunosuppressive Regimen. *New England Journal of Medicine*. 343: 4 230-238.
61. Shapiro, A.M.J. and C. Ricordi and B.J. Hering and H. Auchincloss and R. Lindblad and R.P. Robertson and A. Secchi and M.D. Brendel and T. Berney and D.C. Brennan and E. Cagliero and R. Alejandro and E.A. Ryan and B. DiMercurio and P. Morel and K.S. Polonsky and J.A. Reems and R.G. Bretzel and F. Bertuzzi and T. Froud and R. Kandaswamy and D.E.R. Sutherland and G. Eisenbarth and M. Segal and J. Preiksaitis and G.S. Korbitt and F.B. Barton and L. Viviano and V. Seyfert-Margolis and J. Bluestone and J.R.T. Lakey. 2006. International Trial of the Edmonton Protocol for Islet Transplantation. *New England Journal of Medicine*. 355: 13 1318-1330.
62. Sorkin, R. and T. Gabay and P. Blinder and D. Baranes and E. Ben-Jacob and Y. Hanein. 2006. Compact self-wiring in cultured neural networks. *Journal of Neural Engineering*. 3: 2 95-
63. Tang, M. and Z. Li and L. Chen and T. Xing and Y. Hu and B. Yang and D.-Y. Ruan and F. Sun and M. Wang. 2009. The effect of quantum dots on synaptic transmission and plasticity in the hippocampal dentate gyrus area of anesthetized rats. *Biomaterials*. 30: 4948-4955.
64. Tang, M. and M. Wang and T. Xing and J. Zeng and H. Wang and D.-Y. Ruan. 2008. Mechanisms of unmodified CdSe quantum dot-induced elevation of cytoplasmic calcium levels in primary cultures of rat hippocampal neurons. *Biomaterials*. 29: 4383-4391.
65. Tang, M. and T. Xing and J. Zeng and H. Wang and C. Li and S. Yin and D. Yan and H. Deng and J. Liu and M. Wang and J. Chen and D.-Y. Ruan.

2008. Unmodified CdSe Quantum Dots Induce Elevation of Cytoplasmic Calcium Levels and Impairment of functional Properties of Sodium Channels in Rat Primary Cultured Hippocampal Neurons. *Environmental Health Perspectives*. 116: 7 915-922.
66. Thévenod, F. 2010. Catch me if you can! Novel aspects of cadmium transport in mammalian cells. *Biometals*. 23: 857-875.
67. Van Belle, T.L. and K.T. Coppeters and M.G. Von Herrath. 2011. Type 1 Diabetes: Etiology, Immunology, and Therapeutic Strategies. *Physiological Reviews*. 91: 1 79-118.
68. Wang, K. and H.A. Fishman and H. Dai and J.S. Harris. 2006. Neural Stimulation with a Carbon Nanotube Microelectrode Array. *Nano Letters*. 6: 9 2043-2048.
69. Xu, H. and J. Bai and J. Meng and W. Hao and H. Xu and J.-M. Cao. 2009. Multi-walled carbon nanotubes suppress potassium channel activities in PC12 cells. *Nanotechnology*. 20: 285102-285110.
70. Xu, L.J. and J.X. Zhao and T. Zhang and G.G. Ren and Z. Yang. 2009. In vitro study on influence of nano particles of CuO on CA1 pyramidal neurons of rat hippocampus potassium currents. *Environ.Toxicol*. 24: 3 211-217.
71. Yu, F.H. and V. Yarov-Yarovoy and G.A. Gutman and W.A. Catterall. 2005. Overview of Molecular Relationships in the Voltage-Gated Ion Channel Superfamily. *Pharmacological Reviews*. 57: 387-395.
72. Zhao, J. and L. Xu and T. Zhang and G. Ren and Z. Yang. 2009. Influences of nanoparticle zinc oxide on acutely isolated rat hippocampal CA3 pyramidal neurons. *Neurotoxicology*. 30: 2 220-230.

Chapter 2

2. Electrokinetic measurements of membrane capacitance and conductance for pancreatic β -cells

2.1 Introduction

In this paper we report determinations of the membrane capacitance and membrane conductance for insulin secreting cells, both rat derived insulinoma cells and mouse primary β -cell cultures, using the electrokinetic techniques of dielectrophoresis (DEP) and electrorotation (ER). These methods avoid the need to make electrode contact to the cells, and many cells can be investigated at the same time for a range of physico-chemical environments. The magnitude of the membrane capacitance can be taken as a measure of the total surface area of the cell, and the extent to which this is enhanced by membrane features such as blebs and microvilli, for example. The membrane conductance comprises two main components, namely the conductance across the membrane associated with ion flux through membrane pores and ion channels, together with ionic conduction parallel to the membrane surface associated with the electrical double-layer induced by the net negative charge carried by all cells.

Like neurons and muscle cells pancreatic β -cells are excitable displaying calcium dependent action potentials in bursting patterns. This activity is a key component of glucose responsive insulin release, exhibiting a hierarchal order of

control such that isolated cells ¹, islets (for rat see ²) and insulin blood levels ³ all exhibit a cyclic pulsatile behaviour. To advance our understanding of normal insulin release and diabetes we need to generate good models for insulin release at the single cell level and build from there. For this study, therefore, the pancreatic β -cell, and immortal insulinoma cell lines offer key advantages. Firstly, there exists information on the electrical behaviour of these cells, metabolic control and vesicle fusion events ^{4, 5}. Secondly, the disease relevance gives any methodology that allows large scale observation and modeling of capacitance and conductance – attributes that change in response to glucose stimulation – clear applications in both the basic biology of insulin release and in the screening of novel pharmacological or therapeutic compounds.

The theoretical and experimental aspects of DEP and ER are well described in the literature ⁶⁻¹⁰. In brief, when a cell is exposed to an electrical field it becomes electrically polarized. This polarization takes the form of induced charges that are generated at the cell's external surface, and also within the cell at interfaces between the cytoplasm and the plasma membrane, endoplasmic reticulum and nucleus, for example. The distribution of these charges produces a macroscopic dipole moment, whose magnitude and polarity depends on the dielectric properties of the surrounding solution, as well as those of the various components of the cell. If an alternating current (a.c.) field is applied at a particular frequency, the induced dipole moment will lag the field by a phase angle whose value depends on the dielectric properties of the cell and the solution at that frequency. For the frequency range (10 kHz - 10 MHz) and

solution conductivities (10 - 100 mS/m) used in this work, the polarizability of a viable cell is largely determined by the resistance and capacitance of the plasma membrane, and the lagging phase angle has a value greater than 180° . If the a.c. field is highly non-uniform the cell will move under the influence of a DEP force. At the lower frequencies, and for the solution conductivities used in our experiments, a viable cell will exhibit negative DEP and be repelled from electrode edges. At the higher frequencies the cell will be attracted to the electrodes by positive DEP. If the a.c. field is rotated, the cell will experience a rotational torque and rotate in an anti-field sense over most of the frequency range between 10 kHz and 10 MHz. Values for the membrane capacitance and conductance are obtained by determining the frequency where the antifield rotation rate reaches its maximum value, and the frequency at which the DEP response makes the transition from negative to positive DEP.

2.2 Theory

A cell of radius r , when exposed to a rotating electric field in a solution of conductivity σ_s , will exhibit a maximum antifield ER rate at a frequency f_{pk} given by ⁷:

$$f_{pk} = \frac{K_{ms}}{\pi \cdot r^2 C_m} + \frac{G_m}{2\pi C_m} + \frac{\sigma_s}{\pi \cdot r \cdot C_m} \quad (1)$$

This relationship holds for the case where the conductivity σ_s of the external solution is much lower than the internal conductivity of the cell. This condition was met in our experiments. In equation (1) C_m and G_m are the trans-membrane

capacitance and conductance values, respectively, and K_{ms} is the surface conductance of the cell membrane. Values for C_m for mammalian cells (e.g., erythrocytes, monocytes, granulocytes, B and T cells) range from around 10 to 15 mF/m² ¹⁰, whilst G_m values associated with ion channel conduction typically range from around 10 to 100 S/m² ¹¹. Values for K_{ms} have been assumed to be similar to those for cell-sized polystyrene particles (0.2 to 2 nS) and to be independent of the solution conductivity and field frequencies between 100 kHz and 1 MHz ⁷. To accommodate the fact that in our experiments the cells exhibited a range of radii, values of for various solution conductivities were recorded. From equation (1) we expect a plot of against $\sigma r f_{pk} \cdot r f_{pk_s}$ to be linear (of the form $y = mx + c$) and have a slope m given by

$$m = \frac{1}{\pi C_m} \quad (2)$$

and an intercept c given by

$$c = \frac{1}{\pi C_m} \left(\frac{K_{ms}}{r} + \frac{r G_m}{2} \right) = \frac{r}{2\pi C_m} \left(\frac{2K_{ms}}{r^2} + G_m \right) \quad (3)$$

Huang *et al* ¹² have derived an expression for the DEP cross-over frequency f_{xo} , and by re-arranging the terms in their equation we obtain:

$$f_{xo} = \frac{\sqrt{2}\sigma_s}{2\pi \cdot r \cdot C_m} \sqrt{1 - \frac{r G_m^*}{2\sigma_s} - \left(\frac{r G_m^*}{2\sigma_s} \right)^2} \quad (4)$$

Although not formally stated in the earlier work ¹², should be taken as the total 'effective' membrane conductance, which from equation (3) can be given as:

G_m^*

$$G_m^* = \left(\frac{2K_{ms}}{r^2} + G_m \right) \quad (5)$$

For the DEP experiments reported here, the average value for r was around 5 μm , and values for σ_s ranged from 49 to 101 mS/m. For $G_m \leq 600 \text{ S/m}^2$ the factor $\frac{2K_{ms}}{r^2}$ should not exceed a value of 0.03, so that (on simple application of the Binomial Theorem) to a very good approximation equation (4) can be simplified to the form:

$$f_{xo} \cdot r = \frac{\sqrt{2}}{2\pi C_m} \sigma_s - \frac{\sqrt{2}G_m^* r}{8\pi C_m} \quad (6)$$

From equation (6) we expect a plot of f_{xo} against σ_s to be linear and have a slope m given by:

$$m = \frac{\sqrt{2}}{2\pi C_m} \quad (7)$$

and an intercept c given by:

$$c = -\frac{\sqrt{2}G_m^* r}{8\pi C_m} \quad (8)$$

2.3 Experimental

3.1 Cell Samples

INS-1 (rat insulinoma β -cells) were cultured using standard procedures ¹³ summarized here. The cells were grown in RPMI 1640 medium (Invitrogen)

supplemented with 10 mM HEPES, 10% heat-inactivated fetal calf serum, 2 mM L-glutamine, 1 mM sodium pyruvate, 50 μ M β -mercaptoethanol, and 100U/ml penicillin–streptomycin. A humidified incubator was used and maintained at 37 °C with 5% CO₂, 95% air. Immediately before the experiments, the cells were centrifuged and washed twice in the media to be used in the DEP and ER measurements (see below)

Pancreatic islets were isolated from Swiss-Webster mice (Charles River) by collagenase digestion as previously described by Larsson et al ¹⁴. Briefly, following CO₂ asphyxiation, 2 ml of ice-cold collagenase (0.5 mg/ml, Roche) was infused into the common bile duct. The inflated pancreas was dissected and incubated for 10 minute at 37°C, followed by vigorous shaking. After three washes, islets were picked by hand four times under a dissecting microscope and after overnight culture dispersed by incubation in Ca²⁺/Mg²⁺ free PBS containing 3 mM EGTA and 0.05 mg/ml trypsin for 10 minutes at 37°C with occasional agitation. Immediately before the experiments, isolated islet cells were centrifuged, washed and suspended in the DEP and ER solutions.

3.2 DEP and ER Solutions

Cell suspending solutions of physiological osmolarity were prepared to cover the conductivity range from 11.5 to 101.4 mS/m at 22.5 °C. For the range 11.5 to 42.5 mS/m, the solutions contained 2mM glucose, 5.5 mM Hepes buffer, and adjusted to 300 mos by adding 96 g/mL sucrose. The pH was adjusted to pH 7.4 using NaOH, and the conductivity of individual aliquots was adjusted using KCl. For the range 48.7 to 101.4 mS/m, a stock solution was prepared, comprising:

140 mM NaCl; 5.4 mM KCl; 2.5 mM CaCl₂; 0.5 mM MgCl₂; 11 mM glucose and 5.5 mM Hepes buffer. The solution of highest conductivity (101.4 mS/m) was prepared by adding 8 mL of this stock solution to 92 mL double-distilled water, plus 8.47 g sucrose to give 300 mos. Lower conductivities were prepared through higher dilutions of the stock solution and a higher concentration of sucrose to achieve 300 mos. The conductivities were measured, to within $\pm 0.25\%$, using a YSI 3200 Conductivity Instrument (probe constant $K = 1.0/\text{cm}$).

3.3 *Electrokinetic Experiments*

Gold microelectrodes were manufactured by photolithography in a class II clean room onto glass microscope slides, with a 5 nm chrome adhesion layer and a 70 nm gold layer. Two basic geometries were employed – namely quadrupolar electrodes of the polynomial¹⁵ and ‘bone’ design¹⁶. These electrode geometries are shown in Figure 1.

Digitally generated voltages of frequencies between 10 kHz and 10 MHz, produced using a custom-built generator, were applied to each quadrupole electrode in sequence through 75 Ω coaxial cables. For the ER experiments the ‘bone’ design electrodes were energized with 8 V (pk-pk) signals in phase quadrature so that, as viewed down the microscope and on a TV monitor, the resultant field between the electrodes rotated in a clock-wise sense. For DEP experiments, voltage signals up to 10 V (pk-pk) were applied to the polynomial design electrodes and arranged to give 180^o phase difference between adjacent electrodes. The magnitudes and phases of the four electrode voltages were monitored with a Tektronix TDS3024B oscilloscope.

The electrode arrays were cleaned with alcohol and pure water, and then submerged in water for at least two hours before each experiment. The cells, at a working concentration of 2×10^5 cells/mL or lower, were pipetted directly onto the electrodes and secured with a cover slip. At this concentration most of the suspended cells remained apart during the electrokinetic experiments. The concentration of cells shown in Figure 1 is of the order 5×10^5 cells/mL, and at this concentration many cells have been attracted together as a result of mutual dipole-dipole interactions. The islet cells exhibited a tendency to adhere quite quickly to the glass substrate, and to avoid this effect the electrodes were energized with a rotating field before adding the cells to the electrode array. The electrokinetic responses of the cells were visualized using a Zeiss Axioskop and recorded at 30 frames/sec for later analysis, with a final magnification of 750 on a TV monitor.

In the DEP measurements attention was focused on cells located about 10~20 μm away from an electrode edge, where the field gradient and resulting DEP force would be greater than for cells located further away from the electrodes. The applied voltage frequency was adjusted to cause the cell under examination to sequentially make transitions between positive and negative DEP. The DEP cross-over frequency f_{xo} was determined either by finding the frequency where the cell became stationary, or by interpolating the estimated cell velocities to find the frequency where the DEP force acting on the cell was zero. ER rates were obtained mainly by simple timing with a stopwatch. When better accuracy was required to determine the maximum rotation rate, the video-captured frames

were analyzed using an image processing method described previously ¹⁷. Measurements were not made for cells that had interacted to form doublet or higher-order 'pearl chain' formations. The exact distance between opposite electrode faces (e.g., 393 μm for the nominal 400 μm bone electrodes) was used as the scale to determine cell diameter to an accuracy of $\pm 0.3 \mu\text{m}$.

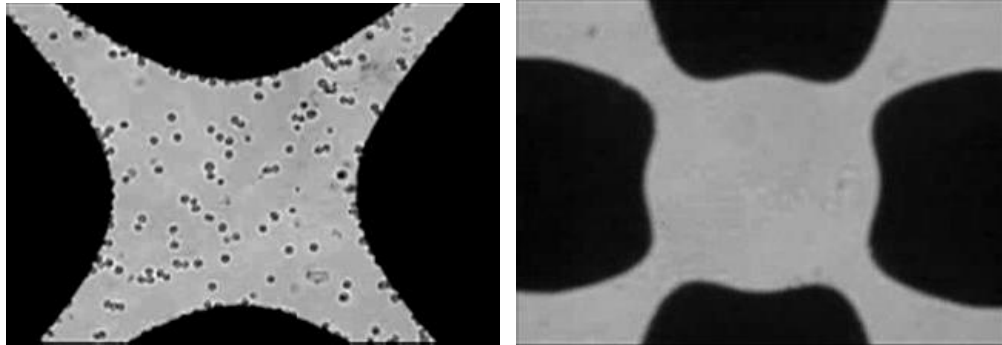


Figure 2.1: Dielectrophoretic Chamber

The polynomial (left) and 'bone' (right) quadrupolar electrode designs used in the DEP and ER experiments, respectively. For DEP measurements, non-uniform electric fields were produced by energizing adjacent electrodes with a.c. signals phased 180° apart. A rotating field was generated by energizing the electrodes with four signals, each separated by 90° phase angle.

2.4 Results

The dispersed pancreatic islet cells tended to adhere strongly to the glass substrate, so that relatively few successful rotation measurements could be obtained for any one cell over the complete frequency range from 10 kHz to 10

MHz. This, coupled with the relatively low number of cells that could be harvested, made it impractical to perform a statistically meaningful ER analysis across the full conductivity range offered by the prepared suspending solutions. The most extensive set of results were obtained using a solution conductivity of 60.3 mS/m, where complete anti-field rotation spectra and values for were obtained for a total of 17 islet cells. Examples of two of these ER spectra are shown in Figure 2.2.

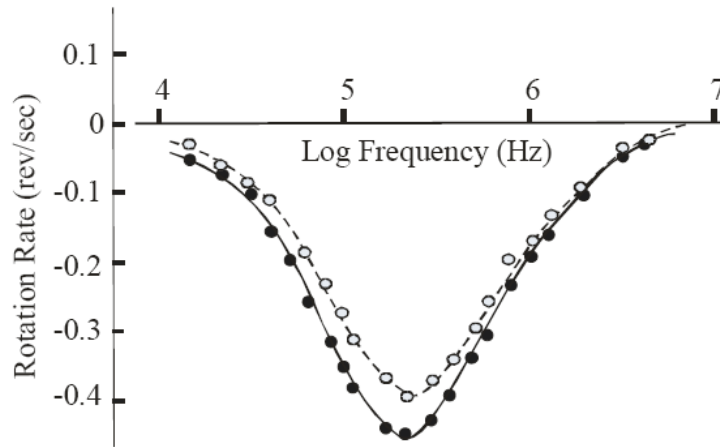


Figure 2.2: Electrorotation Spectra

Electrorotation spectra obtained for two isolated pancreatic islet cells suspended in a solution of conductivity 60.3 mS/m, and with applied quadrature signals of 8 V (pk-pk).

The membrane capacitance $Cpkf_m$ was obtained for each cell using equation (1)

and assumed values for K_{ms} and G_m of 2 nS and 100 S/m^2 , respectively. The

mean value obtained for C_m was 12.57 mF/m^2 , with a standard deviation of 1.46 mF/m^2 . The ER results obtained for the INS-1 cells are shown in Table 2.1 and Figure 2.3.

Conductivity (mS/m)	Cells n	Radius r (μm)	$f_{pk} \cdot r$ (m/sec)
Range 1			
11.5	15	5.3 (0.76)	0.39 (0.10)
21.7	21	5.6 (0.84)	0.62 (0.14)
32.8	15	5.6 (0.54)	1.03 (0.22)
42.5	19	5.3 (0.63)	1.29 (0.30)
Range 2			
48.7	25	4.95 (0.67)	1.58 (0.40)
60.3	15	5.28 (0.77)	1.85 (0.43)
74.9	24	5.61 (0.70)	2.34 (0.67)
86.9	20	5.28 (0.67)	2.66 (0.54)
101.4	24	5.61 (0.71)	3.23 (0.66)

Table 2.1: Anti-field electrorotation rate

The data obtained from determination of cell radius and the frequency f_{pk} , defining the maximum anti-field electrorotation rate, for the INS-1 cells. The mean and standard deviation values are given for the cell radius r and the product $f_{pk} \cdot r$ for cells (number n) suspended in the two sets of suspending media used to cover the conductivity range from 11.5 to 101 mS/m.

The straight lines and formulae shown in Figure 3 are the best linear regression plots obtained using the Microsoft Excel program. From equation (2), using the slope values of 0.0299 and 0.0311, membrane capacitance values of 10.65 mF/m^2 and 10.23 mF/m^2 are derived for the low and higher conductivity data ranges, respectively. The estimated standard deviation for both capacitance results is 2.1 mF/m^2 . Based on these C_m values, the total membrane conductance given by equation (5) can be evaluated using the intercept values given in Figure 3. The 70 cells examined with the lower range (11.5 - 42.5 mS/m)

of solution conductivities were determined to have a radius of $5.3 (\pm 0.68) \mu\text{m}$ which, together with $C_m^* = 10.65 (\pm 2.1) \text{ mF/m}^2$ and $c = 0.0207$, leads to a value for of $261 (\pm 85) \text{ S/m} \cdot \text{mG}^2$. The corresponding value obtained for the higher range (48.7 - 101.4 mS/m) of solution conductivities, for which the 108 cells examined had an average radius of $5.28 (\pm 0.72) \mu\text{m}$, $c = 0.0147$ and $C_m = 10.23 (\pm 2.1) \text{ mF/m}^2$, is $179 (\pm 61) \text{ S/m} \cdot \text{mG}^2$.

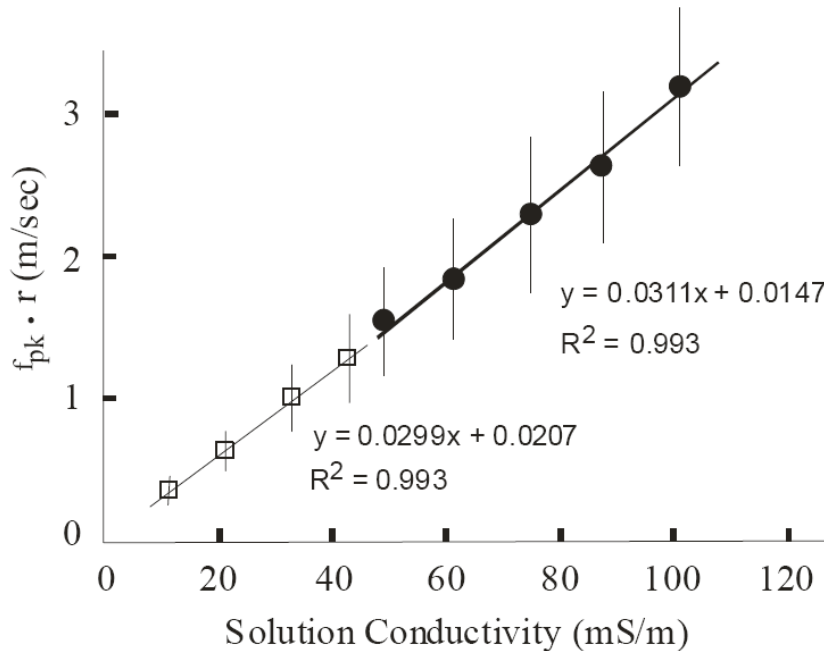


Figure 2.3: Plots of the electrorotation data

Plots of the electrorotation data given in Table 1 for the INS-1 cells. The straight lines represent the best linear regression plots of the data obtained for the two sets of suspending media. The corresponding linear equations and correlation coefficient are presented.

The results obtained from the DEP cross-over frequency measurements on the INS-1 cells are shown in Table 2 and Figure 4. From equation (7), and based on the value (0.0226) for the slope of the linear plot in Figure 4, a value of 9.96

Conductivity (mS/m)	Cells n	Radius r (μm)	$f_{x_0} \cdot r$ (m/sec)
48.7	19	5.24 (0.45)	1.08 (0.26)
60.3	14	5.72 (0.86)	1.33 (0.21)
74.9	15	5.28 (0.70)	1.69 (0.38)
86.9	18	4.96 (0.68)	1.98 (0.47)
101.4	20	5.28 (0.63)	2.25 (0.43)

Table 2.2: DEP Cross-over frequency

The results obtained from determination of the DEP cross-over frequency f_{x_0} for the INS-1 cells. The mean and standard deviation values are given for the cell radius r and the product $f_{x_0} \cdot r$ for cells (number n) suspended in solutions of different conductivity.

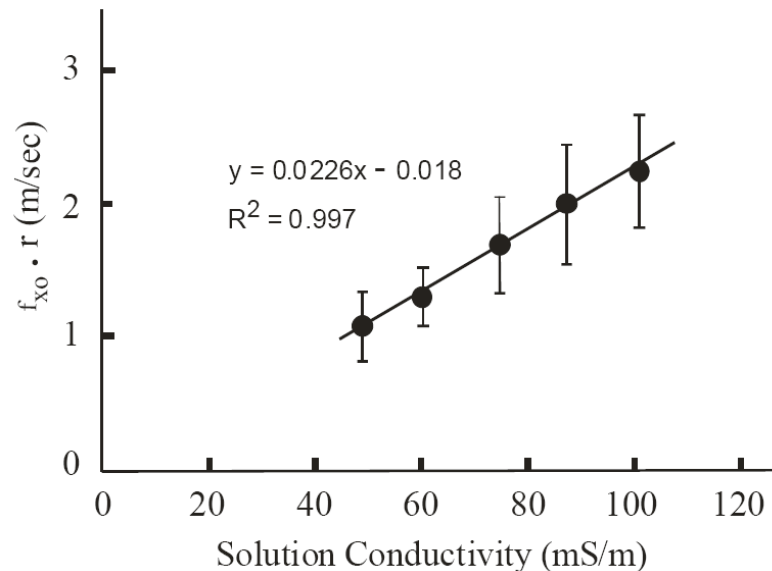


Figure 2.4: Plot of DEP Cross-over Data

Plot of the DEP cross-over data given in Table 2 for the INS-1 cells. The straight line, and corresponding linear equation providing the slope and intercept values, was used to derive a value of $9.96 (\pm 1.89) \text{ mF/m}^2$ and $600 (\pm 340) \text{ S/m}^2$ for the membrane capacitance C_m and effective membrane conductance, respectively.

*mG

mF/m^2 is derived for the membrane capacitance. The estimated standard deviation is 1.89 mF/m^2 . From equation (8), using the mean radius value of $5.3 (\pm 0.6 \mu\text{m})$ determined for the 86 cells examined in the DEP experiments, a mean value of $601 (\pm 182) \text{ S/m}^2$ is obtained for the total effective membrane conductance. *mG

2.5 Discussion and Conclusions

These studies demonstrate that pancreatic β -cells can be characterized and manipulated using the techniques of dielectrophoresis and electrorotation. The dispersed islet cells, if allowed to settle after being loaded onto the electrode assembly, were found to quickly stick to the glass substrate surface. This effect was partially overcome by applying an ER signal to the electrodes during the initial loading of the islet cells. However, a better approach will be to chemically treat or coat the glass substrate to reduce cell adhesion, and this is currently being investigated in our laboratories. The cultured INS-1 β -cells did not adhere to the glass substrate during the experiments and, because sufficient numbers of cells were obtained from the immortalized cell line, measurements could be made for nine different solution conductivities covering the range from 11 to 101 mS/m.

The membrane capacitance value of $12.57 \pm 1.46 \text{ mF/m}^2$ obtained for islet cells, and those of 10.23 ± 2.1 ; $10.65 \pm 2.1 \text{ mF/m}^2$ (ER measurements) and $9.96 \pm 1.89 \text{ mF/m}^2$ (DEP measurements) obtained for INS-1 cells, fall within the range of values determined by ER for T-cells ($10.5 \pm 3.1 \text{ mF/m}^2$), B-cells (12.6 ± 3.5

mF/m²) and granulocytes (11.0 ± 3.2 mF/m²)¹⁸. The ER results for blood cells were obtained for a single suspending medium conductivity (56 mS/m) and were analyzed using the so-called 'single-shell model' for cell structure. The standard deviations obtained in our experiments (1.46 and 2.1 mF/m²) are less than those (3-1 - 3.5 mF/m²) reported¹⁸ for blood cells, and this may reflect the fact that β-cells exhibit a smaller biological variability than blood cells in terms of their membrane morphology. Also, because these membrane capacitance values are less than half the value of 26 mF/m² determined for human breast cancer cells¹⁹, we can conclude that β-cells in their resting state are relatively devoid of surface features such as blebs and microvilli, for example. We base these conclusions on the fact that membrane capacitance values correlate closely with the extent to which the area of an otherwise smooth membrane surface is increased as a result of the presence of membrane folds and protuberances.^{10, 12, 18, 19}

The suspending solutions contained 2 mM glucose or less, and so the INS-1 cells would have been in their resting state. Potassium conductance across the membrane dominates in the resting state of insulin-secreting cells, especially that associated with the ATP-sensitive K⁺ channels.²⁰ Whole-cell patch-clamp measurements on INS cells have produced values for this K_{ATP} conductance of 2,240 (± 248) pS/pF²⁰. Based on the mean membrane capacitance value of 10.44 (± 2.1) mF/m² obtained in our work for the INS-1 cells, this leads to a G_m value for potassium conductance of 23 (± 7) S/m², assuming no contributions from other ion channels or pores. The value derived for the INS-

1 cells from the ER measurements at the high conductivity range is $179 (\pm 61)$ $\text{S/m} \cdot \text{mG}^2$, and it is of interest to note that if we assign a surface conductance K_{ms} value equal to the normally accepted upper value of 2 nS^7 , then from equation (5) we can determine the ion channel conductance G_m value to be $36 (\pm 22)$ S/m^2 . This result lies within the range of the K_{ATP} conductance obtained from the patch-clamp work. However, the K_{ms} value would need to be increased to 3.3 nS for the value of $261 \text{ S/m} \cdot \text{mG}^2$, obtained with the low conductivity solutions, to lead to a G_m value close to that of the K_{ATP} conductance value. In principle, the result from the low conductivity solutions should produce a more accurate determination for G_m based on the intercept value of the linear plot shown in Figure 3, but this can be balanced against the fact that a larger number of cells (108 against 70) were examined at the higher conductivity range.

Finally, a mean value of $601 (\pm 182) \text{ S/m}^2$ was obtained for the total membrane conductance from the DEP cross-over frequency measurements for the INS-1 cells. Although this result is considerably larger than the values obtained from the ER measurements, it is similar to that of $567 (\pm 326) \text{ S/m} \cdot \text{mG}^2$ obtained for rat kidney cells using the same DEP method.¹² It is not clear why membrane conductance values obtained using the ER and DEP techniques should differ so greatly. One reason could be associated with the fact that as a deliberate strategy to maximize the sensitivity of the DEP cross-over experiments, the ‘target’ cells were those near ($\sim 20 \mu\text{m}$ and closer) to the

electrodes. In this situation the cells would experience much larger DEP forces and field stresses than cells further away from the electrodes, and this is a particularly relevant consideration when operating at a field frequency close to the DEP cross-over frequency f_{xo} .²¹ This, in turn, could lead to an increased passive conduction of ions through membrane pores and to increased conduction of ions over the cell membrane surface. In the ER measurements, the cells would experience a uniform rotating field and field stresses much lower than that for the cells characterized for their DEP behaviour. These aspects are now subject to further investigations in our laboratories. We have no evidence to suggest that our applied a.c. electric fields in any way influence ion channel conductances, but this possibility should also be considered.

Acknowledgements:

The INS-1 cells used in this study were a gift from Jude Deeney of the Boston University Medical Center. This study was financed by a gift from the Denis Robinson Memorial Fund to RP and NIH grants NCRR RR001395 and DK06984 to PJSS. We thank Mark Messerli and Leon Collis for valuable discussions, and Robert Lewis and Craig Hamilton for their assistance.

2.6 References

1. Ashcroft, F.M. and P. Rorsman. 1989. Electrophysiology of the pancreatic [beta]-cell. *Progress in Biophysics and Molecular Biology*. 54: 2 87-143.
2. Ikeuchi, M. and W.Y. Fujimoto and D.L. Cook. 1984. Rat Islet Cells have Glucose-Dependent Periodic Electrical Activity. *Horm Metab Res*. 16: 03 125,127-
3. Pørksen, N. 2002. The in vivo regulation of pulsatile insulin secretion. *Diabetologia*. 45: 1 3-20.
4. Rutter, G.A. 2001. Nutrient-secretion coupling in the pancreatic islet [beta]-cell: recent advances. *Molecular Aspects of Medicine*. 22: 6 247-284.
5. Tarasov, A. and J. Dusonchet and F. Ashcroft. 2004. Metabolic Regulation of the Pancreatic Beta-Cell ATP-Sensitive K⁺ Channel. *Diabetes*. 53: suppl 3 S113-S122.
6. Pohl H.A. 1978. Dielectrophoresis: the behavior of neutral matter in nonuniform electric fields. Cambridge University Press,
7. Arnold, W.M. and U. Zimmermann. 1988. Electro-rotation: development of a technique for dielectric measurements on individual cells and particles. *Journal of Electrostatics*. 21: 2-3 151-191.
8. Jones T.B. 1995. Electromechanics of particles. Cambridge University Press,
9. Morgan H. and N.G. Green 2003. AC electrokinetics: colloids and nanoparticles. Baldock : Research Studies Press,
10. Pethig, R. Cell physiometry tools based on dielectrophoresis. pp. 103-126. *In: M. Ozkan and M.J.Heller. [eds.] 2005. **BioMEMS and Biomedical Nanotechnology**. Springer Science,*

11. Lewis, S.A. and J.W. Hanrahan New insights into Cell and Membrane Transport Processes. pp. 305-326. *In*: G. Poste and S.T. Crooke. [eds.] 1986. Plenum Press,
12. Huang, Y. and X.B. Wang and F.F. Becker and P.R.C. Gascoyne. 1996. Membrane changes associated with the temperature-sensitive P85gag-mos-dependent transformation of rat kidney cells as determined by dielectrophoresis and electrorotation. *Biochimica et Biophysica Acta (BBA) - Biomembranes*. 1282: 1 76-84.
13. Farfari, S. and V. Schulz and B. Corkey and M. Prentki. 2000. Glucose-regulated anaplerosis and cataplerosis in pancreatic beta-cells: possible implication of a pyruvate/citrate shuttle in insulin secretion. *Diabetes*. 49: 5 718-726.
14. Larsson, O. and J.T. Deeney and R. Brønström and P.O. Berggren and B.E. Corkey. 1996. Activation of the ATP-sensitive K Channel by Long Chain Acyl-CoA. *Journal of Biological Chemistry*. 271: 18 10623-10626.
15. Huang, Y. and R. Pethig. 1991. Electrode design for negative dielectrophoresis. *Measurement Science and Technology*. 2: 12 1142-
16. Dalton, C. and A.D. Goater and J. Drysdale and R. Pethig. 2001. Parasite viability by electrorotation. *Colloids and Surfaces A: Physicochemical and Engineering Aspects*. 195: 1-3 263-268.
17. Zhou, X.-F. and J. Burt and R. Pethig. 1998. Automatic cell electrorotation measurements: studies of the biological effects of low-frequency magnetic fields and of heat shock. *Physics in Medicine and Biology*. 43: 5 1075-1090.
18. Yang, J. and Y. Huang and X. Wang and X.B. Wang and F.F. Becker and P.R.C. Gascoyne. 1999. Dielectric Properties of Human Leukocyte Subpopulations Determined by Electrorotation as a Cell Separation Criterion. *Biophysical Journal*. 76: 6 3307-3314.
19. Becker, F.F. and X.B. Wang and Y. Huang and R. Pethig and J. Vykoukal and P.R. Gascoyne. 1995. Separation of human breast cancer cells from blood by differential dielectric affinity. *Proceedings of the National Academy of Sciences of the United States of America*. 92: 3 860-864.

20. Nakazaki, M. and M. Kakei and H. Ishihara and N. Koriyama and H. Hashiguchi and K. Aso and M. Fukudome and Y. Oka and T. Yada and C. Tei. 2002. Association of upregulated activity of KATP channels with impaired insulin secretion in UCP1-expressing insulinoma cells. *The Journal of Physiology*. 540: 3 781-789.

21. Menachery, A. and R. Pethig. 2005. Controlling cell destruction using dielectrophoretic forces. *Nanobiotechnology, IEE Proceedings -*. 152: 4 145-149.

Chapter 3

3 Inhibition of Neuronal Calcium Ion Channels by Trace Levels of Yttrium Released from Carbon Nanotubes

3.1 Introduction

Carbon nanotubes show promise as scaffolds for neuronal growth^{9, 19, 23, 31} and stimulation^{3, 17, 20}, nano-pipettes for cell delivery and sampling³⁰, and electrode coatings for enhanced recording¹². Keefer and colleagues recently reported that metal wire electrodes can be coated with CNTs to enhance charge transfer, recording, and electrical stimulation of neurons at the brain-machine interface¹². Intelligent design of this interface may enable the treatment of epilepsy, depression, and Parkinson's disease; and provide hope for restoration of function in paralysis^{7, 12}.

Essential to the success of CNTs in neurotechnologies is their successful integration with electrically active cells. Studies of the patterns of neurites grown upon CNT scaffolds^{9, 19} have revealed altered neurite outgrowth. Additionally, neurons grown in the presence of water soluble SWNTs demonstrated similar outgrowth patterns to those grown upon CNT scaffolds²³ possibly resulting from interference of stimulated endocytosis from CNTs in the cell external solution¹⁸.

Each of these studies suggests that CNTs alter calcium dependent cellular functions of growing neurons. An earlier study suggests that SWNTs can physically occlude ion channels²⁵. The present study was therefore designed to fundamentally assess and characterize the possible effects of CNTs on voltage-gated calcium ion channels, which are present in all excitable cells and underlie many essential cellular functions. In neurons, these channels control calcium entry that triggers transmitter release, gene expression, neuronal excitability, and growth cone extension. Dysfunctional voltage-gated calcium ion channels are implicated in a number of diseases and disorders, and are the targets of many pharmaceutical drugs and neurotransmitters.

3.2 Materials

Source, processing, and characterization of SWNTs:

A variety of commercial arc-synthesized SWNTs were acquired, characterized, and labeled SWNT A-D. Sample B, C, and D were described by the vendor as “purified” and sample A “as-produced”. Sample C was supplied in functionalized form with 4-6 atom-% carboxylate groups. To obtain uniform suspensions in the electrophysiology buffer, SWNTs were rendered hydrophilic through covalent functionalization with aryl-sulfonate groups. Briefly, SWNTs were immersed in 8.4 mM sulfanilic acid solution at 70°C. While maintaining constant temperature and agitation, 1.5 mL of .2 M sodium nitrite solution was added and allowed to incubate for 2 hours. The SWNTs were subsequently washed with distilled water six times and dried at 100 °C for 8 hours. Aryl-sulfonated SWNTs were then suspended in external solution (see below) through mild bath sonication.

Transmission electron microscopy was carried out on JEOL 2010 high-resolution microscope at 200 kV and a Philips 420 microscope at 120 kV. Partial oxidation was carried out to simulate oxidative purification processes for removal of amorphous carbon by heating the carbon nanotubes in a TA Instrument 951 thermogravimetric analyzer at 10 °C/min followed by a 60 min isothermal hold at target temperature. X-ray diffraction analysis of the TGA residues was performed on a Bruker AXS D8 Advance. To remove functional groups on the surface for selected experiments, a ceramic boat was placed in a bench-top tube furnace and purged with nitrogen for 30 min before raising the furnace temperature to 1000°C for 60 min hold time. The furnace was allowed to cool under nitrogen to room temperature.

Transient expression of Ca_v2.2 calcium channels in tsA201 cell line:

Calcium channel subunits Ca_v2.2 (AF055477¹⁴) together with Ca_vβ₃ (sequence homologous to M88751), Ca_vα₂δ₁ (AF286488¹³), and enhanced green fluorescent protein cDNAs (eGFP; BD Bioscience) were transiently expressed in tsA201 cells as described previously using Lipofectamine 2000 (Invitrogen)³².

Cell Studies:

Prior to cell exposure, SWNTs were dispersed through 2-hr bath sonication in the identical cell external solution used in the electrophysiology experiments. The solution in the electrophysiology chamber was then replaced with the external

solutions containing varying doses of SWNTs. The supernatant sample was generated by transferring the sonicated suspensions to a 5000 NMWL Amicon Ultra-Centrifuge tube (Millipore, MA) and subjecting the samples to centrifugal ultrafiltration at 4500 RPM and 4°C for 30 min. We have shown that this protocol removes essentially all of the nanotubes¹⁶.

Electrophysiology:

Calcium currents were recorded using the standard whole cell patch clamp method as described elsewhere³². The extracellular solution contained 1 mM CaCl₂, 4 mM MgCl₂, 10 mM HEPES, 135 mM choline chloride, pH adjusted to 7.2 with CsOH. The recording electrode solution contained 100 mM CsCl, 10 mM EGTA, 1 mM EDTA, 10 mM HEPES, 4 mM MgATP, pH 7.2 with CsOH. Recording electrodes had resistances of 2-4 MΩ when filled with internal solution. Series resistances (< 6 MΩ for whole cell recording) were compensated 70-80% with a 10 μs lag time. Calcium currents were evoked by voltage-steps and currents leak subtracted on-line using a P/-4 protocol. Data were sampled at 20 kHz and filtered at 10 kHz (-3 dB) using pClamp V8.1 software and the Axopatch 200A amplifier (Molecular Devices). All recordings were obtained at room temperature. Cells were typically held at -100 mV to remove closed-state inactivation before applying test pulses 20-25 ms in duration every 6 seconds³².

Assays for metal bioavailability assay and cation surface binding:

Metal bioavailability (mobilization) assays were performed by dispersing the SWNTs in the identical cell external solution used in the electrophysiology experiments or in lysosomal simulant fluid at pH 5.5 (acetate buffer) and removing the SWNTs through centrifugal ultrafiltration (See Cell Studies). Nickel and yttrium content in the clear filtrate were measured by a Jobin Yvon JY2000 Ultrace inductively coupled plasma atomic emission spectrometer (ICP-AES) as described previously¹⁶. Measurements were made at a wavelength of 221.647 nm for Ni and 371.030 nm for Y and intensities were calibrated using standards ranging in concentration from 0 to 5 ug/ml for Ni and from 0 to 10 ug/ml for Y. ICP is accurate at concentrations down to 10 ppb. The interactions between yttrium cation and CNT surface functional groups was studied by adding 0.05-1.0 mg/ml SWNTs to -0.1mM YCl_3 aqueous solution (in DI water, saline or acetate buffer) and ultrasonicated in water bath for 1 hr and rotated overnight at 60 rpm. The solids were then removed by centrifugal ultrafiltration and the filtrate analyzed for Y by ICP as above.

3.3 Results

We used a human embryonic kidney cell line, tsA201, to express cloned neuronal $Ca_v2.2$ N-type calcium ion channel chosen for its established role in regulating neurite outgrowth, transmitter release, and neuronal signaling.^{2, 28} This technique avoids current from other types of channels and thus isolates the behavior of the $Ca_v2.2$ N-type calcium ion channel. Calcium currents originating from synchronous activation of $Ca_v2.2$ channels were recorded using the whole-cell patch clamp recording method (Fig 3.1a, and Supplemental). We exposed

cells to physiological solutions containing different concentrations of water soluble (aryl-sulfonate functionalized³⁵) arc synthesized single-walled carbon

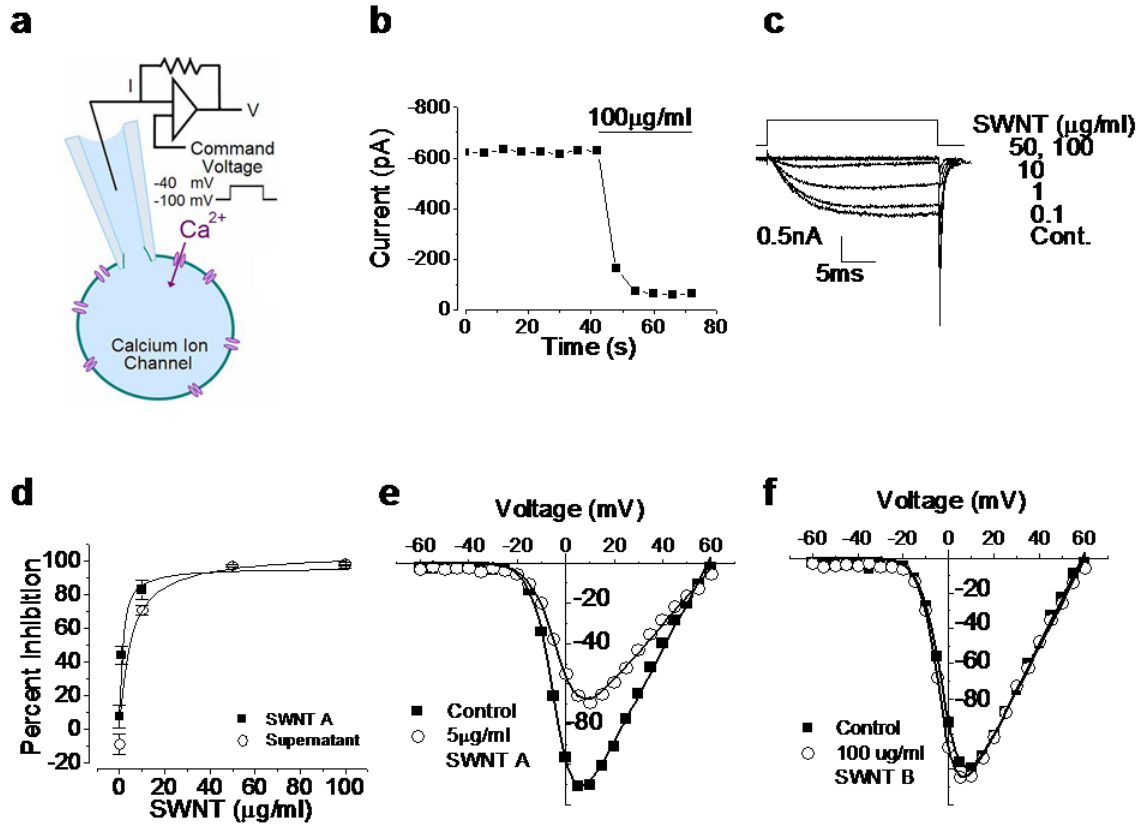


Figure 3.1 SWNT sample A inhibits calcium ion channels, while SWNT sample B does not.

a: Schematic of whole cell patch clamp experiment. b: Time course of calcium current under constant voltage step exposed to 100 µg/ml SWNT A. Horizontal bar indicates the time of nanotube application. c: Calcium current traces from cell exposed to 0.1, 1, 10, 50 and 100 µg/ml SWNT A. X axis is time in ms and the Y axis is calcium current in mA. d: Dose response of calcium current inhibition resulting from exposure to varying concentrations of SWNT A (solid squares) and associated supernatant (i.e. nanotube-exposed buffer solution after nanotube removal) (open circles). Strong inhibition is seen even in the CNT-free supernatant! Error bars represent standard error (n=3). SWNT A data fit with a hyperbolic non-linear curve, $y = 96.3x/(1.22 + x)$; the IC_{50} of SWNT A is $1.22 \mu\text{g/ml} \pm 0.13$. The supernatant is fit with hyperbolic non-linear curve $y = 105x/(5.0 + x)$ and the associated IC_{50} is $5.00 \mu\text{g/ml} \pm 2.3$. e: Entering calcium current as a function of command voltage over the range -60 mV to 60 mV of control (solid square) and 5 µg/ml SWNT A exposed cell (open circle). The maximum current observed in the control cell occurred at 5 mV and is -111 pA. The maximum current after exposure to 5 µg/ml is at 10 mV and is -69.4 pA. f: Entering calcium current as a function of command voltage over the range -60 mV to 60 mV of control (solid square) and 100 µg/ml SWNT B exposed cell (open circle).

f: Entering calcium current as a function of command voltage over the range -60 mV to 60 mV of control (solid square) and 100 $\mu\text{g/ml}$ SWNT B exposed cell (open circle). Maximum current of -199 pA was observed at 10 mV in control and -125 pA at 5 mV. Panel 1a adapted from Dunlop *et al* Nature Reviews 2008⁴ nanotubes (SWNTs) and monitored the magnitude and voltage-dependence of calcium currents.

Calcium currents were inhibited rapidly when cells were exposed to SWNT-containing solutions (Fig 3.1b; sample "A"). Inhibition was dose-dependent (Fig. 3.1c) and apparent at all voltages without altering the voltage-dependence of channel activation (Fig. 3.1e). The magnitude and speed of inhibition was unexpected and indicative of direct inhibitory effects on the calcium ion channel (Fig. 3.1b). We removed the SWNTs from solution through centrifugal ultrafiltration and, surprisingly, observed an almost equivalent level of inhibitory activity (Fig. 3.1d), which was similar in time course to the action of the original SWNT-containing solution (Fig. 3.1c). This inhibition occurs in the absence of the original nanotubes.

The inhibitory action of the supernatant indicates a mechanism involving nanotube-induced alteration of the fluid medium, rather than direct interaction between tubular graphene and the ion channel or other cellular targets. High-surface-area SWNTs have been shown to significantly alter cell culture medium through adsorption of folic acid⁶ and molecular probes³⁴ and can release soluble metal forms^{11, 16, 27} through oxidative attack on metal catalyst residues that are not fully encapsulated by graphenic carbon shells^{15, 16}. To assess the role of metals, we therefore tested the effects of SWNT B, a sample determined to be unusually well purified with respect to free metal (Fig 3.2 c, d). Physiological

solutions containing SWNT B had no detectable inhibitory activity on voltage-gated calcium channels up to 100 $\mu\text{g/ml}$ (Fig. 3.1f). Since the supernatant of SWNT A had similar inhibitory capability to SWNT A containing solutions, and the unusually well purified sample SWNT B did not have any inhibitory action, this strongly suggests a metals effect rather than an alteration of the buffer composition through adsorption.

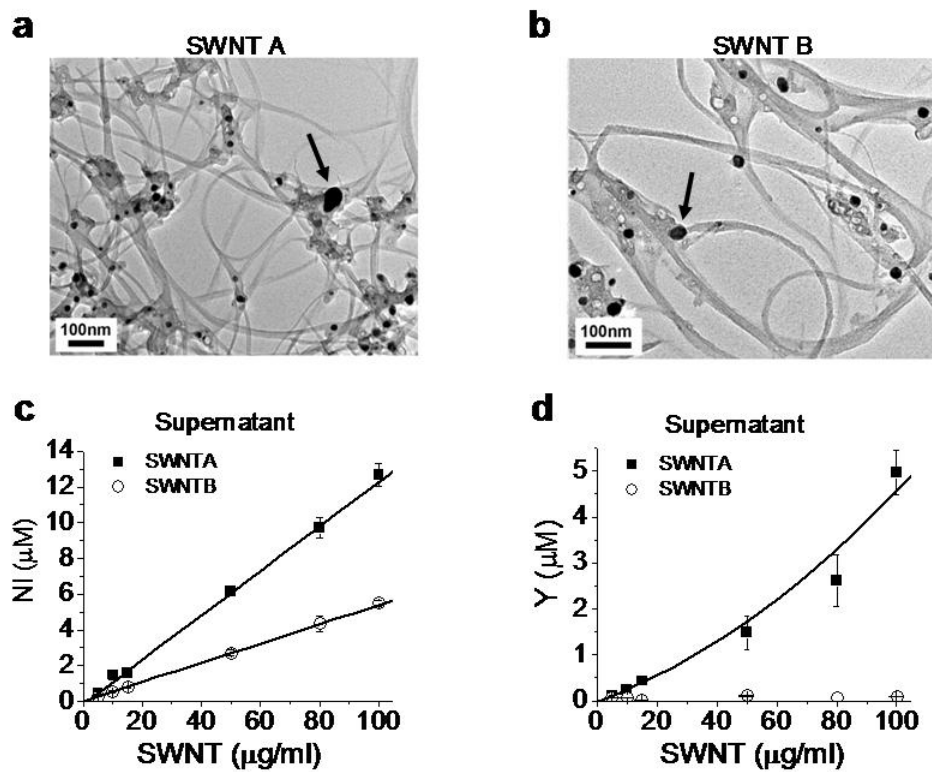


Figure 3.2 Bioavailable nickel and yttrium in SWNT samples.

a, b: Metal catalyst nanoparticles visible by TEM. Scale bar: 100 nm. Arrows point to catalytic particles. The total metal mass percentages by digestion and ICP-ES are 23.3% nickel and 5.77% yttrium for SWNT A, and 6.7% nickel and 1.3 % yttrium for SWNT B. c,d: Results of quantitative dose-dependent metal mobilization (bioavailability) assays. Figures give total soluble Ni and Y concentrations after SWNT samples were sonicated in CES buffer for 2 hours at pH 7.2 followed by centrifugal ultrafiltration and ICP analysis of the filtrate. These were the same conditions used for electrophysiological characterization. Error bars represent standard deviation from triplicate determination.

The nanotubes in our studies were fabricated using a nickel-yttrium catalyst, and abundant metal nanoparticles are visible in both SWNT samples by TEM (Fig. 3.2). Previous studies have reported that a small portion of CNT-embedded metal is typically fluid accessible through defective carbon shells, and can become solubilized in physiological buffers by slow oxidation^{15, 16}. This "bioavailable" metal fraction is not always eliminated by current purification protocols, and does not correlate well with total metal content^{15, 16}. As both SWNT samples contain visible metal nanoparticles, we hypothesized that nickel and yttrium are released and solubilized into the recording solution in sufficient quantities to inhibit the channels from SWNT A but not B. We used inductively coupled plasma- atomic emission spectrometry (ICP-AES) to measure levels of bioavailable nickel and yttrium (Figs 3.2c, 3.2d) in the recording solution (See 3.6 Supplemental). Figure 3.2 shows that both SWNT samples contain bioavailable nickel, but only SWNT A contains detectable quantities of bioavailable yttrium.

We next tested the sensitivity of N-type calcium channels to nickel and yttrium cations in control salt solutions. Both metals inhibited calcium current rapidly, but yttrium was 300-fold more potent than nickel (Nickel IC₅₀ = 219 ± 40 μM; Yttrium IC₅₀ = 0.76 ± 0.15 μM; n = 3; Fig. 3). Similar inhibitory effects of yttrium have been documented on native calcium channels and calcium-dependent processes^{1, 21, 22} consistent with inhibitory effects of other ions of the lanthanide series at protein calcium binding sites²¹. Of the trivalent ions in the lanthanide series, yttrium is the most potent inhibitor of high voltage-activated calcium channels¹. Yttrium like cadmium, another potent inhibitor of high voltage-

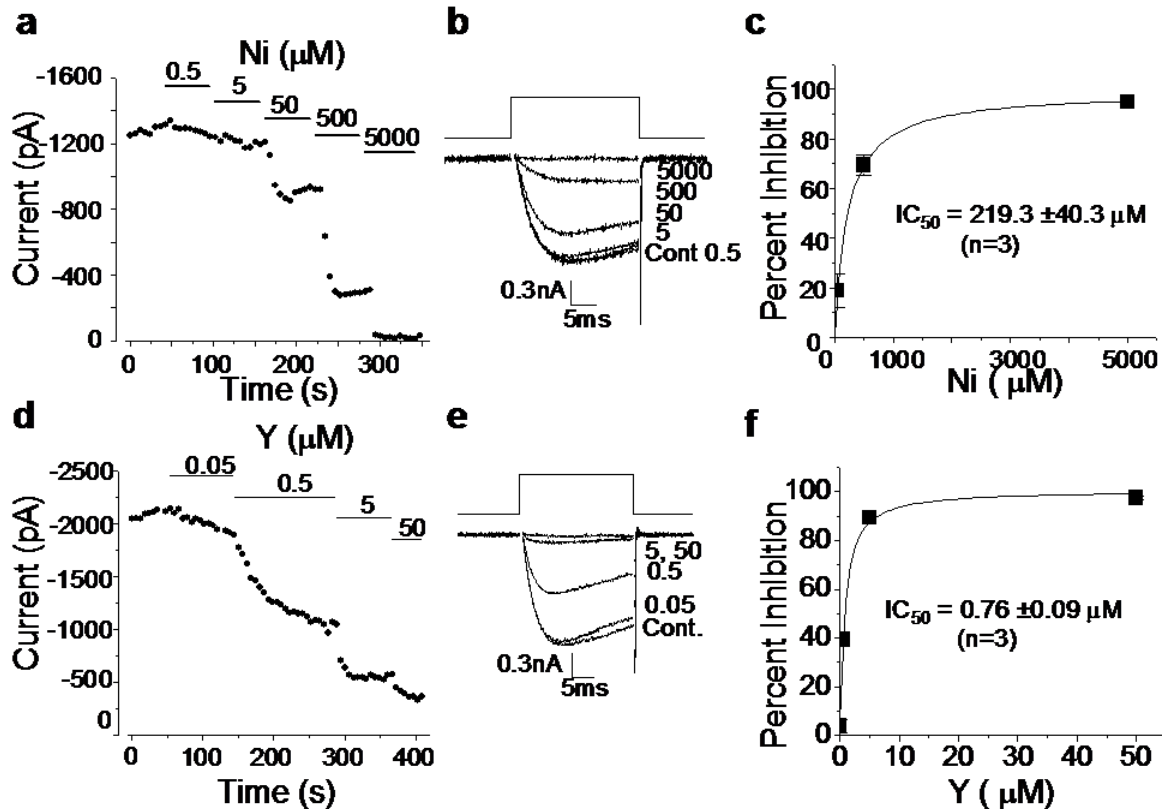


Figure 3.3 Control experiments with soluble salts isolate the effects of Ni and Y on neuronal voltage-gated calcium ion channels.

a-c: Nickel effects. a: Time course showing decreasing calcium current with increasing nickel dose. Solid bars represent time and dose of application. b: Representative traces of nickel inhibition across the range 0.5 to 5000 μM . c: Nickel dose response curve fit with a hyperbolic non-linear function of the equation: $y = 99.3x / (219.3 + x)$. From these results, the IC_{50} for nickel inhibition of $\text{Ca}_v2.2$ -type neuronal calcium channels is 219 μM . d-f: Yttrium effects. d: Time course showing decreasing calcium current with increasing dose of yttrium. Solid bars represent time and dose of application. e: Representative traces of yttrium inhibition across the range 0.05 to 50 μM . f: Yttrium dose response curve fit with a hyperbolic non-linear function of equation: $y = 100.7x / (.76 + x)$. From these results, the IC_{50} for yttrium inhibition of $\text{Ca}_v2.2$ -type neuronal calcium channels is 0.76 μM . Yttrium is an extremely potent calcium-ion-channel blocker.

activated calcium channels, is thought to inhibit calcium flow by competing for calcium binding sites of the ion selectively filter of the pore^{1, 22, 29} (see Fig. 3.5).

To characterize the factors governing yttrium release from nanotubes, we included two additional SWNT samples (C and D) and studied the location, form, and behavior of CNT-associated yttrium. SWNT C has been commercially functionalized with carboxylate groups. SWNT D was included to show that significant concentrations of bioavailable metal may remain in vendor purified samples. A majority of CNT-associated metal in these samples is in the form of metal-rich nanoparticles encapsulated by thin carbon shells of variable thickness (Fig. 3.4). Partial oxidation of SWNT D was carried out to simulate oxidative purification processes for removal of amorphous carbon by heating. Air oxidation attacks carbon shell structures (See 3.6 Supplemental), greatly increasing the mobilization of Y and Ni into media (Fig. 3.4c). The dissolved Y:Ni ratio is much higher than the initial condensed-phase Y:Ni ratio of 1:7. This indicates preferential oxidation and solution release of Y over Ni, consistent with the higher oxidation potential of Y (2.37 V^8) relative to Ni (0.25 V). While SWNT D has been “purified” by the supplier, it nevertheless contains sufficient free Y to inhibit channel function, even before air oxidation is employed to remove carbon shells and increase metal bioavailability ($\sim 10 \mu\text{M}$ at zero carbon loss in Fig. 3.4c, which by Fig. 3.3f, is 13 times the IC₅₀ of Y).

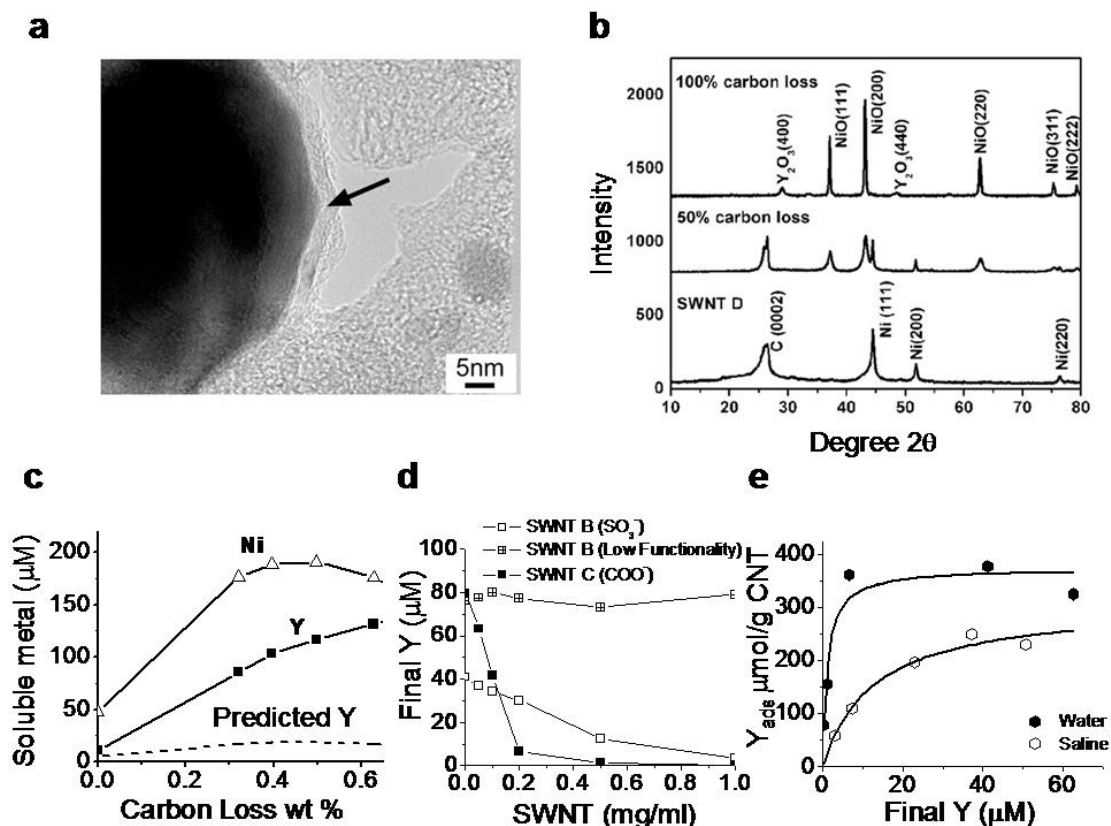


Figure 3.4 . Yttrium phases in SWNTs and mechanisms of yttrium ion release and recapture by SWNT surface functional groups.

a: Typical metal catalyst morphology in arc-synthesized SWNT (sample D): Ni/Y nanoparticles are encapsulated in thin (2 – 10 nm) carbon shells (arrow). Previous studies on nanotube nickel and iron show that carbon-shells protect most but not all metal from fluid-phase attack by dioxygen or protons that leads to oxidation and soluble ion release^{5, 15, 16}. b: X-ray diffraction spectra show that most metal is in the form of zero-valent metal nanoparticles with nickel lattice spacing, which upon extensive dry air oxidation can be converted to separate NiO and Y₂O₃ phases. c: Effect of controlled air oxidation of SWNT D on metal phases and ionic release into a cellular lysosomal simulant buffer at pH 5.5 (2 hr incubation at room temperature of 1.0 mg/ml SWNTs). The dashed curve gives the soluble Y concentration expected if the release were proportional to the Ni release at the initial Ni:Y ratio of 7:1 w/w. d,e: Fundamental adsorption isotherms that characterize the interactions of soluble yttrium with nanotube surface functional groups. D: sulfonated and carboxylated nanotubes remove yttrium ion from solution by surface binding, while the graphenic surfaces of unfunctionalized nanotubes have little effect. e: Adsorption isotherms for yttrium ion binding on SWNT-COOH in pure water and saline. pK_a of these COOH groups determined here to be 3.5 by mass titration. Panel E data allow estimation of the fundamental equilibrium constants for competitive Y³⁺/Na⁺ binding (see dashed curves and analysis in Supplemental). K_d = 1.2 µM (for Y³⁺/SWNT-COO⁻); and K_d = 9060 µM (for Na⁺/SWNT-COO⁻).

In samples subjected to acid purification, yttrium salt re-deposition on surface functional groups is also possible and may be an unappreciated source of bioavailable metal in nanotubes. Figure 3.4d shows that sulfonate and carboxylate functional groups introduced on CNTs can bind soluble yttrium from solution. The adsorption isotherms in panel Figure 3.4e were used to derive fundamental equilibrium constants for yttrium binding to CNT-carboxylate (See 3.6 Supplemental) and the competitive effects of Na^+ binding on yttrium adsorption from saline solutions. We report dissociation constants: $K_d = 1.2 \mu\text{M}$ (for $\text{Y}^{3+}/\text{SWNT-COO}^-$); and $K_d = 9060 \mu\text{M}$ (for $\text{Na}^+/\text{SWNT-COO}^-$). The low K_d for soluble Y is consistent with the expected strong binding of the hard Lewis acid Y^{3+} to the hard carboxylate anion. This strong binding allows significant Y^{3+} adsorption to occur even in the presence of Na^+ , which is the major ion in physiological saline (~1500 factor higher concentration than yttrium). The K_d for Ca^{2+} ($\text{Ca}^{2+}/\text{SWNT-COO}^-$) is $26.5 \mu\text{M}^{15}$, which is also much higher than K_d for Y^{3+} ($1.2 \mu\text{M}$), implying that Y^{3+} has the potential to replace Ca^{2+} on carboxylic binding sites.

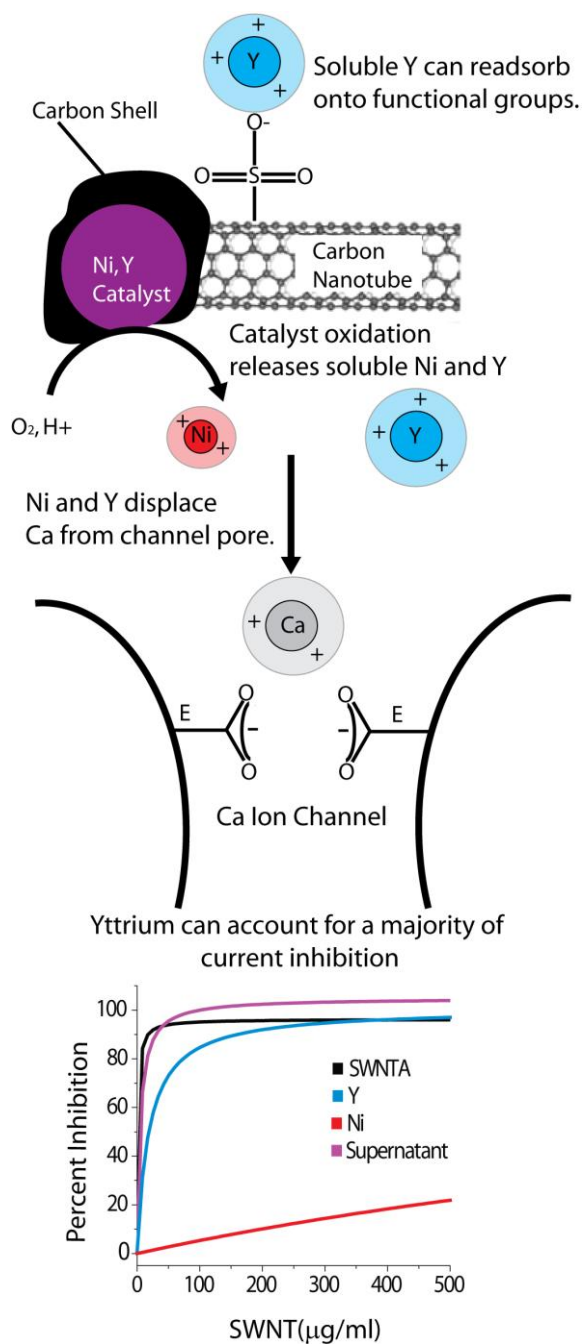


Figure 3.5 Summary of proposed mechanism through which carbon nanotube suspensions inhibit neuronal calcium ion channels.

Nickel-yttrium catalyst nanoparticles (Purple) are oxidatively corroded by fluid-phase attack through defects or cracks in the surrounding carbon shells leading to solubilization of nickel (Red) and yttrium (Blue) into the media. Purification protocols reduce but do not typically eliminate this bioavailable metal. For functionalized nanotubes, soluble metal can become re-associated during purification or processing by adsorption onto anionic functional groups, to become an additional source of bioavailable metal in nanotube samples¹⁵. Nickel

and especially yttrium ions in solution compete with and displace calcium ions (Gray) from the channel pore. The putative selectivity filter of the calcium ion channel consists of four glutamate residues (E). Two glutamates are shown pointing into the calcium ion pore, creating a calcium ion binding site which is predicted to be part of the ion selectively filter²⁹. Calcium is believed to coordinate these residues to enable both high throughput permeability and ion selectivity of the channel. Yttrium cation has a similar ionic radius to calcium, and thus exhibits a good geometric match to the selectivity filter, but is trivalent and has a higher binding coefficient for carboxyl residues than calcium, likely leading to its very high potency as a channel inhibitor. Nickel has a smaller ionic radius than calcium suggesting it is unable to coordinate the carboxyl side chains as effectively as calcium and yttrium consistent with its lower potency as an inhibitor²². The figure (bottom) shows model curves generated from our combined data (Figs. 3.1, 3.2, 3.3) in order to estimate the contribution of yttrium and nickel to the overall inhibition by the whole SWNT A sample. The SWNT A inhibition curve is forecast from our experimental data. The equation of the curve (from Fig. 3.1d) is $SWNT_A_{inh} = 96.3x/(1.22 + x)$ with IC_{50} 1.22 $\mu\text{g/ml}$ SWNT A. Similarly, the equation of the supernatant curve (Fig. 3.1d) is $y = 105x/(5.0 + x)$ with IC_{50} of 5.0 $\mu\text{g/ml}$ SWNT A. The concentration of yttrium released from higher doses of SWNT A is given by $Y_{conc} = .04[SWNT_A]$. These yttrium concentrations are then substituted into the inhibition curve provided in Fig. 3.3f. The inhibition associated with each yttrium concentration is shown as a function of corresponding SWNT A concentration to yield the inhibition model shown by equation $Y_{inh} = 100.7x/(19.0 + x)$ with IC_{50} 19.0 $\mu\text{g/ml}$ SWNT A. The concentration of nickel released from higher doses of SWNT A is given by $Ni_{conc} = .124[SWNT_A]$. These nickel concentrations are then substituted into the inhibition curve provided in Fig. 3.3c. The inhibition associated with each nickel concentration is shown as a function of corresponding SWNT A concentration to yield the inhibition model shown by equation $Ni_{inh} = 99.3x/(1768.5 + x)$ with IC_{50} of 1768.5 $\mu\text{g/ml}$ SWNT A. It is evident that yttrium is responsible for a majority of the channel inhibition during nanotube exposure. We find no evidence that the tubular graphene structure is involved in channel inhibition.

3.4 Discussion

Figure 3.5 summarizes our findings on the chemical pathways for yttrium responsible for SWNT-induced channel inhibition. Included in Fig. 3.5 is a set of calculated curves derived from the combined data set that give quantitative estimates of the contribution of CNT-derived yttrium and nickel to the overall

inhibition seen in the whole nanotube sample. SWNT-derived yttrium can account for the inhibition within experimental error, while nickel is not a factor in this dose range. The modest difference between the whole nanotubes and the yttrium salt solutions may be due to differences in yttrium speciation or cooperative (synergistic) effects of Y and Ni, which were not studied here. The difference cannot reflect a contribution from tubular graphene, because the nanotube-free supernatant shows the same behavior as the whole nanotubes (Fig. 3.1f) and the nanotube sample with ultra-low-yttrium (B) shows no inhibition (Fig. 3.1f) even when all the tubular graphene is present.

The potency of yttrium as a channel blocker here is not unexpected, and is likely due to strong yttrium/carboxylate binding, as already discussed for the case of carboxylate groups on nanotube surfaces. The putative selectivity filter within the ion conducting pore of high voltage-gated calcium channels contains four glutamates, one contributed by each of the four domains of the channel²⁹ (Fig. 3.5). The carboxyl residues of the glutamate side chains are thought to coordinate two calcium ions; creating the selectively filter and supporting ion permeation²⁹. Yttrium is likely to compete for and displace calcium ions from their binding sites within the ion pore without permeating. The ionic radii of calcium and yttrium are similar (0.99 and 0.90 Å, respectively) consistent with the proposal that they could occupy the same narrow binding site within the ion pore. Smaller ions like Ni (0.69 Å) have lower affinity perhaps because they cannot coordinate the carboxylate side of the selectivity filter as well as calcium, yttrium, and cadmium. If the trivalent yttrium has a higher binding affinity as compared to

calcium, it will occlude calcium entry^{1, 21, 22}. Unlike calcium, which is present at concentrations high enough to carry charge (2 mM), Y levels are insufficient to support significant current, so the net effect is current inhibition.

Our finding that CNT-yttrium blocks calcium-ion channels has important implications for nanotube-enabled drug delivery, biolabeling, and tissue engineering in bone, muscle, nerve, and other excitable cells. Channel inhibition may also follow unintended nasal inhalation and translocation across the olfactory bulb to the brain²⁴. The Ni:Y catalyst is the most common formulation in arc-synthesized SWNTs today²⁶, and yttrium's high potency on voltage-gated calcium ion channels (IC₅₀ of 70 ppb) suggests SWNTs at levels as low as 1 ug/ml (1 ppm w/w) could disrupt normal calcium signaling in neurons and other electrically active cells.

Our results also indicate that current purification practices do not reliably reduce free yttrium content to levels below 70 ppb, therefore effects on calcium signaling in neurons and other excitable cells may be expected from many arc-synthesized tubes. Tissue engineering applications may be especially sensitive to yttrium released from CNTs because nanotubes are close-packed in scaffolds or on substrates to produce high effective local nanotube concentrations in the near-cellular space. In light of our results, it is possible that soluble metals are the underlying cause of some literature reports of calcium-dependent effects and nanotube-induced ion channel blocking. We note, however, that many studies of nanotube/neuronal interactions use other nanotube types that do not contain yttrium, and thus cannot trigger the mechanism reported here (see for example

Cellot et al³, which uses MWNTs grown using an Fe catalyst). In general, the influence of metal ions in CNT/neuroengineering studies will be highly variable and dependent on the specific nanotube material and its processing history. Future studies should carefully control for the release of metal ions, especially yttrium, to ensure proper interpretation of the observed interaction between nanotubes and electrically active cells.

3.5 Conclusions

Aqueous suspensions of arc-synthesized single-wall carbon nanotubes are observed here to inhibit neuronal calcium ion channels at low nanotube doses. The electrophysiological characterization of the nanotube-suspensions combined with the control experiments using supernatant solutions and salt solutions clearly show that this inhibition is not due to tubular graphene, the primary nanotube structure, but rather bioavailable yttrium released from the nanotube catalyst. Yttrium is such a potent inhibitor of high voltage-gated calcium ion channels (IC₅₀ of 0.76 μ M or 0.07 ppm w/w) that yttrium-related effects on excitable cells are likely to occur for other arc-synthesized SWNT samples. The present finding highlights the complexity of nanomaterial samples and the potential for secondary or trace material features to trigger adverse biological responses.

3.6 Supplemental

Whole Cell Patch Clamp Technique

The whole cell patch recording method is used to measure currents from small cells while maintaining constant voltage (voltage-clamp). In this method inward calcium currents are activated by test voltages applied at values between -60 mV and +60 mV from a holding potential of -100 mV. Characteristic time-dependent changes in current are exemplified by current traces shown in Fig. 3.1c. The maximum current vs. test voltage relationship is U-shaped (Fig. 3.1e). Inward current increases with stronger test depolarization because of the steep dependence of channel open probability on voltage. However, the concomitant decrease in driving force on calcium ions with depolarization acts to decrease current flow through each individual channel. The inward current is eventually balanced by an equal and opposite outward current at the channel reversal potential of close to +60 mV (Fig 3.1e).

Analysis of competitive metal binding to CNT-carboxylate functional groups

The metal adsorption isotherms in Fig. 3.4e were used to determine equilibrium constants for soluble yttrium binding to CNT-carboxylate, both in DI water and in saline where Na⁺ ions compete for the same sites. The relevant reaction and binding equilibrium constant are:



$$K_Y = \frac{[\text{CNT-COOY}^{2+}]}{[\text{CNT-COO}^-][\text{Y}^{3+}]} = \frac{N_Y}{(N_{\text{max}} - N_Y)[\text{Y}^{3+}]} \quad (\text{S2})$$

where N_Y is the number of bound sites, N_{max} is the total number of surface carboxylic sites, and $[\text{Y}^{3+}]$ represents here the total concentration of all soluble yttrium species at equilibrium. Relation S2 fits the experimental isotherm of Fig. 3.4f well giving $N_{\text{max}}=0.37$ mmol/g and $K_Y = 857$ l/mmol. Expressed as a dissociation constant: $K_d = 1/K_Y = 1.2$ μM , which is the soluble yttrium concentration at which 50% of the available carboxylic sites will be occupied. From Figure 3.2d, yttrium mobilization into the electrophysiology buffer achieves higher concentrations than 1.2 μM , indicating that CNT-surface-bound Y^{3+} is likely another source of bioavailable Y (beyond the discrete nanoparticles), and may explain why whole SWNT suspension has a slightly stronger calcium ion channel inhibitory effect than the supernatant alone (where the CNT-surface-bound yttrium is absent).

In physiological solutions yttrium must compete with other ions for carboxylate binding sites on nanotubes and in the selectivity filter in the ion channel pore. Here simple experiments were conducted in saline solution to probe the competitive binding of yttrium and sodium on CNT-carboxylates. Figure 3.4e shows that total yttrium binding from 80 μM solutions is reduced but still significant in the presence of 154 mM Na^+ , allowing a quantitative analysis of competitive binding. In Y-doped saline two equilibrium expressions must be satisfied simultaneously:

$$K_Y = \frac{[\text{CNT-COOY}^{2+}]}{[\text{CNT-COO}^-][\text{Y}^{3+}]} = \frac{N_Y}{(N_{\text{max}} - N_{\text{Na}} - N_Y)[\text{Y}^{3+}]} \quad (\text{S3})$$

$$K_{Na} = \frac{[\text{CNT-COOY}^{2+}]}{[\text{CNT-COO}^-][\text{Na}^+]} = \frac{N_{Na}}{(N_{\max} - N_{Na} - N_Y)[\text{Na}^+]} \quad (\text{S4})$$

Where K_Y , N_{\max} were determined previously (857 l/mmol and 0.37 mmol/g respectively). At 154 mM, $[\text{Na}^+]$ is nearly constant since it is much higher than the initial (maximum) yttrium concentration (~0.1 mM). This leaves K_{Na} as the only unknown variable. Fitting the data in Fig. 4e yields $K_{Na} = 0.11$ l/mmol, or a sodium dissociation constant K_d of 9060 μM and provides a satisfactory curve shape (see Figure 3.4e bottom line). Clearly yttrium binding continues in the presence of the abundant Na^+ ion, but is reduced from the pure water case by ion-ion competition.

Our reported dissociation constants ($K_d = 1.2 \mu\text{M}$ for yttrium/SWNT-COO⁻) can be compared to the reciprocal binding constants for Y^{3+} and $\text{Y}(\text{OH})^{2+}$ reported by Turkel *et al.* in experiments on salicylic acid, which range from 0.1 to 1000 μM depending on the soluble yttrium species^{8, 33}. The metal speciation diagram for yttrium indicates Y^{3+} and $\text{Y}(\text{OH})^{2+}$ under the neutral pH conditions of the CES buffer¹⁰

3.7 References

1. Beedle, A.M. and G. Zamponi. 2002. Inhibition of Transiently Expressed Low- and High- Voltage-Activated Calcium Channels by Trivalent Metal Cations. *Journal of Membrane Biology*. 187 225-238.
2. Catterall, W.A. and A.P. Few. 2008. Calcium channel regulation and presynaptic plasticity. *Neuron*. 59: 6 882-901.
3. Cellot, G. and E. Cilia and S. Cipollone and V. Rancic and A. Sucapane and S. Giordani and L. Gambazzi and H. Markram and M. Grandolfo and D. Scaini and F. Gelain and L. Casalis and M. Prato and M. Giugliano and L. Ballerini. 2008. Carbon Nanotubes might improve neuronal performance by favouring electrical shortcuts. *Nature Nanotechnology*. 4: 126-133.
4. Dunlop, J. and M. Bowlby and R. Peri and D. Vasilyev and R. Arias. 2008. High-throughput electrophysiology: an emerging paradigm for ion channel screening and physiology. *Nature Reviews Drug Discovery*. 7: 358-368.
5. Guo, L. and D.G. Morris and X. Liu and C. Vaslet and R.H. Hurt and A.B. Kane. 2007. Iron Bioavailability and Redox Activity in Diverse Carbon Nanotube Samples. *Chemistry of Materials*. 19: 14 3472-3478.
6. Guo, L. and A. Von Dem Bussche and M. Beuchner and A. Yan and A.B. Kane and R.H. Hurt. 2008. Adsorption of essential micronutrients by carbon nanotubes and the implications for nanotoxicity testing. *Small*. 4: 6 721-727.
7. Hochberg, L.R. and M.D. Serruya and G.M. Friehs and J.A. Mukand and M. Saleh and A.H. Caplan and A. Branner and D. Chen and R.D. Penn and J.P. Donoghue. 2006. Neuronal ensemble control of prosthetic devices by a human with tetraplegia. *Nature*. 442: 164-171.
8. Horovitz C.T. 1999. *Biochemistry of Scandium and Yttrium, Part 1: physical and chemical fundamentals*. Kluwer Academic/Plenum Publisher,

9. Hu, H. and Y. Ni and V. Montana and R.C. Haddon and V. Parpura. 2004. Chemically Functionalized Carbon Nanotubes as Substrates for Neuronal Growth. *Nano Letters*. 4: 3 507-511.
10. Johnson, D.J. and D.T. Amm and T. Laureson and S.K. Gupta. 1998. Monolayers and Langmuir-Blodgett films of yttrium stearate. *Thin Solid Films*. 326: 223-226.
11. Kagan, V.E. and Y.Y. Tyurina and V.A. Tyurin and N.V. Konduru and A.I. Potapovich and A.N. Osipov and E.R. Kisin and D. Schegler-Berry and R. Mercer and V. Castranova and A.A. Shvedova. 2006. Direct and indirect effects of single walled carbon nanotubes on RAW 264.7 macrophages: Role of iron. *Toxicology Letters*. 165: 88-100.
12. Keefer, E.W. and B.R. Botterman and M.I. Romero and A.F. Rossi and G.W. Gross. 2008. Carbon nanotube coating improves neuronal recordings. *Nature Nanotechnology*. 3: 434-439.
13. Lin, Y. and S.I. McDonough and D. Lipscombe. 2004. Alternative Splicing in the Voltage-Sensing Region of N-Type Cav2.2 Channels Modulates Channel Kinetics. *Journal of Neurophysiology*. 92: 2820-2830.
14. Lin, Z. and S. Haus and J. Edgerton and D. Lipscombe. 1997. Identification of Functionally Distinct Isoforms of the N-Type Ca²⁺ Channel in Rat Sympathetic Ganglia and Brain. *Neuron*. 18: 1 153-166.
15. Liu, X. and L. Guo and D. Morris and A.B. Kane and R.H. Hurt. 2008. Targeted Removal of Bioavailable Metal as a Detoxification Strategy for Carbon Nanotubes. *Carbon*. 43: 3 489-500.
16. Liu, X. and V. Gurel and D. Morris and D.W. Murray and A. Zhitkovich and A.B. Kane and R.H. Hurt. 2007. Bioavailability of Nickel in Single-Wall Carbon Nanotubes. *Advanced Materials*. 19 2790-2796.
17. Lovat, V. and D. Pantarotto and L. Lagostena and B. Cacciari and M. Grandolfo and M. Righi and G. Spalluto and M. Prato and L. Ballerini. 2005. Carbon Nanotube Substrates Boost Neuronal Electrical Signaling. *Nano Letters*. 5: 6 1107-1110.

18. Malarkey, E.B. and R.C. Reyes and B. Zhao and R.C. Haddon and V. Parpura. 2008. Water Soluble Single-walled Carbon Nanotubes Inhibit Stimulated Endocytosis in Neurons. *Nano Letters*. 8: 10 3538-3542.
19. Mattson, M.P. and R.C. Haddon and A.M. Rao. 2000. Molecular Functionalization of Carbon Nanotubes and Use as Substrates for Neuronal Growth. *Journal of Molecular Neuroscience*. 14: 175-182.
20. Mazzatenta, A. and M. Giugliano and S. Campidelli and L. Gambazzi and L. Businaro and H. Markram and M. Prato and L. Ballerini. 2008. Interfacing Neurons with Carbon Nanotubes: Electrical Signal Transfer and Synaptic Stimulation in Cultured Brain Circuits. *Journal of Neuroscience*. 27: 26 6931-6936.
21. Mlinar, B. and J.J. Enyeart. 1992. Block of current through T-type calcium channels by trivalent metal cations and nickel in neural rat and human cells. *Journal of Physiology*. 469 639-652.
22. Nachshen, D.A. 1984. Selectivity of the Ca Binding Site in Synaptosome Ca Channels. *Journal of General Physiology*. 83: 941-967.
23. Ni, Y. and H. Hu and E.B. Malarkey and B. Zhao and V. Montana and R.C. Haddon and V. Parpura. 2005. Chemically Functionalized Water Soluble Single-Walled Carbon Nanotubes Modulate Neurite Outgrowth. *Journal of Nanoscience and Nanotechnology*. 5: 1707-1712.
24. Oberdörster, G. and E. Oberdörster and J. Oberdörster. 2005. Nanotoxicology: An Emerging Discipline Evolving from Studies of Ultrafine Particles. *Environmental Health Perspectives*. 113: 7 823-839.
25. Park, K.H. and M. Chhowalla and Z. Iqbal and F. Sesti. 2003. Single-walled Carbon Nanotubes are a New Class of Ion Channel Blockers. *Journal of Biological Chemistry*. 278: 50 50212-50216.
26. Plata, D.L. and P.M. Gschwend and C.M. Reddy. 2008. Industrially synthesized single-walled carbon nanotubes: compositional data for users, environmental risk assessments, and source apportionment. *Nanotechnology*. 19: 1-13.

27. Pulskamp, K. and S. Diabaté and H.F. Krug. 2007. Carbon Nanotubes show no sign of acute toxicity but induce intracellular reactive oxygen species in dependence on contaminants. *Toxicology Letters*. 168: 58-74.
28. Raingo, J. and A.J. Castiglioni and D. Lipscombe. 2007. Alternative splicing controls G protein-dependent inhibition of N-type calcium channels in nociceptors. *Nature Neuroscience*. 10: 3 285-292.
29. Sather, W.A. and E.W. McCleskey. 2003. Permeation and Selectivity in Calcium Channels. *Annual Review of Physiology*. 65: 133-159.
30. Schrlau, M.G. and E.M. Falls and B.L. Ziober and H.H. Bau. 2008. Carbon nanopipettes for cell probes and intracellular injection. *Nanotechnology*. 19: 015101 1-4.
31. Seidlits, S.K. and J.Y. Lee and C.E. Schmidt. 2008. Nanostructured scaffolds for neural applications. *Nanomedicine*. 3: 2 183-199.
32. Thaler, C. and A.C. Gray and D. Lipscombe. 2004. Cumulative inactivation of N-type Cav2.2 calcium channels modified by alternative splicing. *Proceedings of the National Academy of Sciences*. 101: 15 5675-5679.
33. Turkel, N. and R. Aydin and U. Ozer. 1999. Stability of complexes of scandium (III) and yttrium (III) with salicylic acid. *Turkish Journal of Chemistry*. 23: 249-256.
34. Worle-Knirsch, J.M. and K. Pulskamp and H.F. Krug. 2006. Oops They Did It Again! Carbon Nanotubes Hoax Scientists in Viability Assays. *Nano Letters*. 6: 6 1261-1268.
35. Yan, A. and X. Xiao and I. Külaots and B.W. Sheldon and R.H. Hurt. 2006. Controlling water contact angle on carbon surfaces from 5° to 167°. *Carbon*. 44: 3113-3148.

Chapter 4

4. Conclusions and Future Perspectives

I contributed to two distinct projects as part of my doctoral research. This chapter will address these topics individually. Each subsection will review the main conclusions of the published papers and suggest future work. In the latter work, I had the opportunity to begin conducting experiments linked to these future research objectives and will present preliminary data. The first subsection will discuss dielectrophoresis of insulin secreting cells. The second subsection will address the effect of carbon nanomaterials on voltage-gated ion channels.

4.1 Electrokinetic Measurements of Membrane Capacitance and Conductance for Pancreatic β -cells

Conclusions

In order to effectively use dielectrophoresis as a means of tissue engineering islets of Langerhans, it is first necessary to determine if the technique can effectively control insulin secreting cells in two dimensions. For this purpose, primary beta cells and INS-1 cells (Insulinoma cell line) were placed in a dielectrophoretic chamber. The osmolarity of the media was altered and cell membrane capacitance and membrane conductance values were reported. Through the methods of dielectrophoresis and electrorotation, a membrane capacitance value of $12.57 (\pm 1.46) \text{ mF/m}^2$ was obtained for β -cells, and the

values ranging from $9.96 (\pm 1.89) \text{ mF/m}^2$ to $10.65 (\pm 2.1) \text{ mF/m}^2$ were obtained for INS-1 cells. This falls within the range expected for mammalian cells. The electrorotation results for the INS-1 cells lead to a value of $36 (\pm 22) \text{ S/m}^2$ for the membrane conductance associated with ion channels, if values in the range 2nS to 3 nS are assumed for the membrane surface conductance. This membrane conductance value falls within the range reported for INS cells obtained using the whole-cell patch-clamp technique. However, the total 'effective' membrane conductance value of $601 (\pm 182) \text{ S/m}^2$ obtained for the INS-1 cells by dielectrophoresis is significantly larger (by a factor of around three-fold) than the values obtained by electrorotation. This could result from an increased membrane surface conductance, or increased passive conduction of ions through membrane pores, induced by the larger electric field stresses experienced by cells in the dielectrophoresis experiments. These results confirm that it is possible to control the directionality of INS-1 cells dielectrophoretically.

Future Studies

In order to further explore the application of dielectrophoresis to tissue engineering the islets of Langerhans, it will be necessary to determine if insulin-secreting cells can be aggregated in three dimensional structures. The techniques of planar dielectrophoresis described in this work will need to be extended to enable the aggregation of three dimensional structures. Viability assays will need to be conducted to determine if insulin-secreting cells remain viable once aggregated into a three dimensional cluster. It will also be interesting

to establish if the three-dimensional aggregate will form intercellular connections, such as gap-junctions, which are key features of native islets. Finally, it will be interesting to determine if the pseudoislet will have the phenotypic bursting pattern associated with glucose-triggered secretion of insulin.

Using the data presented in Chapter 2, remaining members of the research team made progress towards these goals by generating a pseudoislet through dielectrophoresis. The islet was approximately the size of native islets (150 μm X 120 μm) and constructed of insulin secreting cells.⁴² Further studies will address the above posed questions.

4.2 Inhibition of Neuronal Calcium Ion Channels by Trace Levels of Yttrium Released from Carbon Nanotubes

Conclusions

Carbon nanotubes (CNTs) are used with increasing frequency in neuro-engineering^{21, 22, 27-30, 35}. CNT scaffolds are used to transmit electrical stimulation to cultured neurons^{22, 27, 30} and to control outgrowth and branching patterns of neurites^{21, 29, 35}. CNTs have been reported to disrupt normal neuronal function including alterations in endocytotic capability²⁸ and inhibition of ion channels⁴⁰. Calcium ion channels regulate numerous neuronal and cellular functions including endo and exocytosis, neurite outgrowth, and gene expression. CNT interactions with these channels would have significant biological implications. The results presented in Chapter 3 show that physiological solutions containing CNTs inhibit neuronal voltage-gated calcium-ion channels in a dose-dependent and sample-dependent manner with IC_{50} as low as 1.2 $\mu\text{g}/\text{ml}$. Importantly, we

demonstrate that the inhibitory activity does not involve the tubular graphene structure, but rather very low concentrations of soluble yttrium released from the nanotube growth catalyst. Cationic yttrium inhibits calcium ion channel function^{3, 33, 34} with an inhibitory efficacy, IC_{50} , of 0.07 ppm w/w. Because of this inhibitory potency, unpurified and even some reportedly “purified” CNT samples contain sufficient bioavailable yttrium to inhibit channel function at low nanotube doses. The results have important implications for emerging nano-neurotechnologies and highlight the critical role that trace components can play in the biological response to complex nanomaterials.

Implications

The alteration of biological response in the presence of nanomaterials or studies testing material biocompatibility falls within the broad spectrum of nanotoxicology. Careful review of the literature suggests that water-soluble single-walled carbon nanotubes affect normal neuronal calcium homeostasis. Early studies observed varied effects of complex materials on complex neuronal structures resulting in seeming disparity among the literature. Our contribution was to simplify the complex cellular and complex material system to one in which material features were controlled and used to study their effect on a particular cellular response, i.e. calcium current through voltage gated ion channels. The results were interesting in a number of ways. First, it presented evidence that tubular graphene does not inhibit voltage-gated ion channels as previously hypothesized in the literature⁴⁰ Second, it attributed the bulk of the inhibitory

effect to catalytic yttrium; having the smallest presence within the minor components of the catalyst of the single-walled nanotube structure. Lastly, it highlights that some vendor-purified nanotubes contain enough yttrium to have a biological effect. More broadly, however, this work is unique among nanotoxicological studies in its design and result. By simplifying the system, we were able to directly attribute the toxicological effect of each component of the complex nanostructure on the observed biological effect. This is a very powerful result rarely obtained in the field of nanotoxicology.

Beyond the scientific methodology, the results may have a broader impact regarding the biocompatibility of single-walled nanotubes for neuronal applications. This work may suggest a potential causal-effect between arc-synthesized single-walled carbon nanotube catalytic contaminants and the observed alterations of calcium homeostasis highlighted by outgrowth patterns of neurites previously reported in the literature³⁵. In our work, the system contained sulfonated single-walled nanotubes dispersed into solution through sonication. We suggest that the release of metal ions into solution results from fluid phase accessibility of the catalyst resulting in oxidation and metal ion release. The fluid phase can access the catalyst through surface defects inherent in some of the amorphous carbon shells. It is possible that the sulfonation and sonication process further weakened the carbon shells enhancing the release of bioavailable metal ions. As similar materials and preparation techniques were used in the Ni *etal* study, it is also possible that release of metal ions into solution could have caused the observed altered neurite outgrowth patterns. A direct

connection, however, cannot be made without conducting ICP bioavailability studies within the system originally studied.

The catalytic contaminants of nickel and yttrium, specifically, are not present in all commercial single-walled nanotubes. Since catalytic fabrication methods are dominant for large-scale production, almost all commercial carbon nanotube samples, including vendor-purified samples, do however, contain catalytic residues. Other popular catalysts include: iron, cobalt and molybdenum. In addition to nickel and yttrium, many of these other metal catalysts are also voltage-gated channel inhibitors¹⁷. In a recent survey of roughly seven carbon nanotube manufactures, most 'as-produced' single-walled nanotube samples contain 25-40% wt catalytic particles. With new purification protocols, vendor purified samples contain 1.5–3% wt metal catalysts. While ranges are provided by manufactures, the actual quality of each individual sample needs to be characterized in order to properly account for the actual metal content contained in each nanotube sample.

A sample calculation can be made to address the possibility that metal ions leached from engineered nanotube-based biomaterial scaffolds. Assume a scaffold composed of single-walled nanotubes contains 0.1 mg nanotube per 50 mm² scaffold surface area, with metallic compositions of 3% and 40% by weight to account for both 'vendor-purified' and 'as-produced' samples, and with a ratio of 4:1 (wt) Ni:Y provided by the vendor for the composition of metal present in the catalytic particles. If all the yttrium is released, then the total amount of yttrium present will be in the range of 0.015 µg/mm² to 0.2 µg/mm². To approximate the

effective concentration, the depth of homogenous diffusion prior to cellular effect has to be considered. If we assume a distance of 5 μm and 5 mm, representing cells grown on the scaffold and in the vicinity of the scaffold respectively, then the effective concentration for vendor purified nanotube samples containing 3% metallic residue would be in the range 33,708 μM (at 5 μm) to 33.7 μM (at 5mm). For samples containing 40% metallic residue, the concentration of yttrium present, if all metal ions were released, would be even higher; 449,438 μM (at 5 μm) and 449.44 μM (at 5mm). As you increase the distance from the scaffold, the concentration of yttrium will decrease. These values are well above the IC50 value (0.76 μM yttrium) observed for voltage-gated calcium ion channels in our published work. In fact, the distance from the scaffold at which the concentration of yttrium is equivalent to the IC50 value for yttrium, is 222 mm for scaffolds containing 3% metal content, and 2,957 mm for scaffolds containing 40% metal content. This suggests yttrium release from single-walled nanotube scaffolds of both 'vendor-purified' and 'as-produced' samples could potentially inhibit calcium ion channels of cells grown on and in the vicinity of the scaffolds.

The above calculation provides the maximum yttrium concentration possible from a scaffold of 0.1 mg nanotube per 50 mm^2 , allowing for 3% and 40% metal content respectively and 1/4th of the available metal being yttrium. While this provides a valuable approximation, some caveats should be mentioned. First, it is unlikely that all metal catalyst will be released at once when a sample is arranged as a scaffold. Not all amorphous carbon shells encasing the catalytic particles will have cracks that allow the liquid phase to

enter and oxidize the metals enabling ionic release. It is possible that over time, scaffolds can be worn and damaged enabling the release of additional metal ions. Additionally, as the nanotubes are arranged in a scaffold, it is possible that not all carbon shells are on the surface and fluid accessible. These considerations would decrease the available yttrium-ion concentration from the maximum values provided.

In order to eliminate the potential effects of ionic release from catalytic metals, many strategies have recently been developed and published. First, removal of catalytic residues through additional acid washes and purification steps eliminate catalytic metals available to the fluid phase, catalysts that remain encased are shown to be stable for up to two months²⁶. Second, recent work has suggested the possibility of manufacturing nanotubes with inert catalysts such as gold⁴ or in the absence of metal catalysts altogether¹⁸. Lastly, some scaffold preparation techniques, such as functionalization through 1,3-dipolar cycloaddition followed by defunctionalization onto glass coverslips, are known to produce scaffolds that are free of catalytic residues^{8, 27, 30}.

If researchers are aware of the potential biological effects of residual catalytic metals, the aforementioned strategies may remove the toxicological threat. However, the potential for cross-disciplinary researchers to obtain 'vendor-purified' samples and assume they are free of metallic residues exists. The broader importance of our work is, therefore, to definitively highlight the inhibitory effect of these minor material features on voltage-gated ion channels in the field of neuroscience. With the onset of additional purification protocols, new

manufacturing techniques and material handling procedures, metallic residues may be reduced or eliminated. However, stringent quality control protocols will be necessary to insure that metallic residue do not produce unintended or unwanted consequences.

Future Studies

The inhibition of neuronal type calcium ion channels from single-walled carbon nanotubes through the release of catalytic yttrium is of importance, not only to clarify previous literature, but also to potentially design new nanomaterial interfaces. The inhibition of voltage-gated calcium ion channels has a deleterious effect if it inhibits neuronal communication or alters neuronal-growth patterns in unpredictable ways.

Many pharmaceutical drugs target ion channels for inhibition as the mode of action. This inspired me to identify a situation where the inhibition of voltage-gated calcium ion channels is beneficial and to design experiments that maximize this benefit. While the work is in progress, the potential is great. In the next section I will provide appropriate background and describe the potential application of yttrium oxide nanoparticles in combination with carbon nanotubes as a novel surface coating for chronically implanted neural electrodes to increase charge transfer and decrease biological impedance resulting from glial scar formation. I will then show preliminary data highlighting the progress and limitations of the experiments that have been conducted to date.

Application to Chronically Implanted Neural Electrodes

Establishing a direct and controllable electrical link to the neural circuitry of the brain is a goal of the field of neuroengineering. The chronically implanted neural electrode (CINE) is the hardware at the physical interface with neurological tissue and the current means of establishing a connection to the circuitry of the brain. CINEs have been used for the development of the brain machine interface (BMI) most commonly applied through deep brain stimulation DBS and the generation of neuroprosthetics. DBS is becoming a common treatment option for movement disorders such as Parkinson's disease and tremor, neuropathic pain, epilepsy and psychiatric disorders such as Tourette Syndrome, obsessive compulsive disorder and depression. Future treatment considerations utilizing DBS include hypertension, minimally conscious states, obesity, aggressiveness and drug addiction². Hamani *et al* reported an instance where DBS applied to treat an obese patient unexpectedly resulted in detailed autobiographical memories and improved associative-memory tasks,¹⁵ suggesting the possibility that DBS might be useful for memory impairment disorders. In addition to medical therapies, DBS has also provided new insight into our understanding of cortical function³⁷. The BMI has also enabled the generation of neuroprosthetics such as the cochlear implant, and research is underway to develop a prosthetic to restore vision. An advanced neuroprosthetic device has enabled movement in paralyzed patients¹⁹.

The major challenge currently facing further development of the BMI is the need to decrease electrode impedance. The two main sources of electrode

impedance are the ability of a surface to transfer charge, and the physical inability of the implanted material to function due to encapsulation resulting from inflammatory biological response. It has been shown that inhibiting calcium ion channels will attenuate reactive gliosis^{10, 24, 39}. As demonstrated in Chapter 3, yttrium is a potent inhibitor of calcium ion channels. Moreover, electrodes coated with SWNTs have enhanced charge transfer and reduced impedance¹². Therefore, future research initiatives should explore the development of scaffolds that contain both carbon nanotubes and yttrium oxide nanoparticles to inhibit proximate calcium ion channels resulting in attenuated reactive gliosis.

Background

Neural interfaces connect neurons to electronic circuitry of the BMI. Neural interfaces serve to enable the understanding of physiological processes at the cellular level, and as prosthetics that restore function in the nervous system. Implantable neural interfaces record neuronal action potentials from within the brain. Ideally, electrodes should minimize damage to neural tissue, have numerous electrode sites to enable the interpretation of neural activity, have stable impedance, and have long-term biocompatibility.⁹ Neural interfaces perform very well in short-term acute applications; however, decreased reliability is observed in chronic applications. In the clinical setting, CINEs need to reliably record unit activity for decades.⁴³ A significant source of CINE failure is due to the biological response.

Studies in monkeys have reported a 40% drop in the number of functional electrodes and an 85% drop in the number of recordable neurons after 18

months.³⁶ Turner *et al* developed model probes made of silicon and inserted them into the rat cerebral cortex. A 'sheath of cells' was found to loosely organize after two weeks, adhering to the surface of the probe. By six weeks the sheath was highly compacted and continuous.⁴⁷ While the degree of scarring is proportional to electrode size, the process of encapsulation of chronic electrodes occurs independent of size, geometry and surface roughness.⁴⁶ The cells encapsulating the model electrodes can be labeled with antibodies for glial fibrillary acidic protein (GFAP)^{46, 47} and vimentin⁴⁶ indicating the encapsulation results from reactive gliosis of astrocytes. Reactive gliosis surrounding chronically implanted electrodes not only occurs in rat and mouse models, but also in non-human primates.¹³ Models of electrode bioimpedance have confirmed that astrocytes are the predominant cell type affecting bioimpedance, with the largest impedance contribution coming from reactive gliosis within 100 μ m of the neural interface.³¹ The distance from a neuronal body required to maintain a stable recording from an electrode is on the order of cell dimensions⁴³

The formation of a glial scar is independent of the type of electrode inserted and is the dominant theory behind the failure of CINEs. However, local neurodegeneration around the implant site may also contribute to electrode failure. Biran *et al* observed a significant reduction in nerve fiber density and nerve cell bodies in the tissue immediately surrounding the implanted silicon microelectrode.⁵ McConnell *et al* hypothesized that chronic inflammation, due to the persistent presence of the electrode, causes local neurodegeneration in the immediate vicinity of electrode implantation. The group observed progressive

neuronal and dendritic loss (but not axonal) correlated with increased levels of chronic inflammation over 16 weeks.³² This highlights an additional potential benefit of the proposed method, ie, the neuroprotection afforded by calcium channel inhibitors²⁵ and in particular yttrium⁴⁴.

Combined, these studies underscore the necessity of reducing the inflammatory response to chronically implanted electrodes. Reactive astrocytes surrounding the implant site are the main contributor to electrode encapsulation,^{46, 47} increased levels of bioimpedance at the electrode interface³¹, and contribute to local neurodegeneration^{5, 32} resulting in electrode failure. Generating a surface coating for electrodes that reduces astrocyte activation is a primary objective of this research.

Glial Scar Formation

As an electrode enters the brain, it damages capillaries, extracellular matrix and cells.⁴³ In general, the wound-healing response consists of four steps:

hemostasis, inflammation, repair and remodeling. For CINEs, this can be simplified into two immune responses: early and prolonged.^{14, 46} In the early acute response, severed capillaries allow activated platelets to contact the electrode, triggering the formation of a stable fibrin clot. Hemostatic clot formation occurs within seconds to hours after brain injury.⁴⁵ In addition to clot formation, activated platelets release signaling molecules that chemotactically attract inflammatory and wound healing cells. This marks the beginning of the inflammation phase of wound healing. The first cells present at the injury site are neutrophils. They release proteolytic enzymes for digestion of foreign debris, and superoxide and hydrogen peroxide to kill bacteria.⁴⁵ Once bacteria and

debris are cleared, the neutrophils undergo apoptosis. Microglia, the phagocytic cells of the CNS, become activated if debris needs to be cleared or if the blood-brain barrier is compromised.⁴³ They can remain active for up to two weeks, producing proinflammatory and neurotoxic factors (TNF- α , MCP-1, IL-1 β , IL-6, nitric oxide and superoxide) as well as anti-inflammatory and neurotrophic factors (IL-10, NGF, BDNF and neurotrophin-3).⁴⁵ Three days into the inflammatory response, activated astrocytes are seen at the periphery of the wound, while microglia are located at the center with the fibrin clot.⁴⁵ Astrocytes are involved in neurotransmitter regulation, ion homeostasis, blood-brain barrier maintenance, and the production of extracellular matrix molecules.¹¹ During inflammation, activated astrocytes increase production of GFAP and vimentin, and have hypertrophic cytoplasm, nuclei and increased proliferation^{41, 43}. The acute phase is dominated by the microglial response to the insertion trauma of the CINEs and lasts one to three weeks^{43, 46}.

At this point, in non-CNS tissue, the healing response enters the repair phase. However, the continued presence of the electrode and the inability of neurons of the CNS to regenerate, result in the generation of the glial scar that forms a boundary separating the foreign body from the rest of the brain. The prolonged reactive response that is dominated by reactive astrocytes, starts at the time of implantation and ends six to eight weeks post implantation with reactive gliosis.⁴³ At the center of the scar, microglia continue to digest the fibrin clot. A key element of glial scar formation is the inhibition of tissue regeneration.¹¹ Therefore, the glial scar can increase electrode bioimpedance

and remodel nearby tissue further separating neurons from the electrode surface.

43

Strategies to Improve Neural Interface

The size of the initial injury is proportional to the degree of acute response.

Therefore, up until recently, engineering strategies to reduce glial scar formation hinged on the geometry and insertion mechanism of the implant. As scar formation is a chronic response, encapsulation of chronic electrodes occurs independent of size, geometry and surface roughness.⁴⁶ Once in the body, the non-specific adsorption of proteins leads to cell adhesion and the foreign body response.⁹ While inflammatory cell adhesion to the electrode is detrimental, adhesion of neurites is advantageous. Therefore, more recent strategies have focused on engineering neural interfaces with anti-inflammatory agents, adhesion proteins or bioactive molecules.¹⁴ Dexamethasone, an anti-inflammatory agent used to reduce inflammation surrounding pace-makers, has been used as a surface coating for CINEs. *In vitro* studies show electrochemically controlled release of dexamethasone incorporated into a conductive polymer coating on a Michigan electrode had a comparable reduction in the count of reactive astrocytes as administration of the drug alone.⁴⁸ Another strategy includes the incorporation of immobilized anti-inflammatory agent, α -MSH, on the silicon electrode surface. A reduction in the microglial response and subsequent attenuation in glial scar formation was observed up to four weeks *in vivo*.¹⁶ This result is hopeful; however, since the glial scar is not fully formed around an electrode until week 6 *in vivo*⁴⁷, the efficacy in practice remains to be seen. Other strategies include the introduction of nanoscale surface roughness. By

increasing surface roughness, electrode impedance decreases and the amount of signal loss is reduced.⁹ To date, there have not been any strategies utilizing calcium channel inhibitors in the prevention of reactive gliosis around electrodes. There have not been any electrode coating designs to date that address two sources of electrode impedance.

Calcium channel inhibitors attenuate gliosis

The primary interface between the brain and the CINE undergoes a microglial response. Reactive astrocytes, involved in the formation of the glial scar, encompass the microglia/electrode. While astrocytic inhibition is the experimental focus of the current research, I hypothesize that yttrium oxide nanoparticle based calcium channel inhibitors will act in two ways to attenuate scar formation: first by inhibiting the microglial activation and second by inhibiting astrocyte activation. In this section I present evidence that inhibition of voltage-gated calcium channels attenuates activation of microglia and astrocytes.

IL-1, TGF- α , TGF- β , TNF- α , INF- α , and INF- γ have all been shown to effectively augment reactive gliosis *in vivo*.⁴⁵ Intracellular calcium levels increase when microglia are activated.²⁰ Brown *et al* have reported that ultrafine carbon black enhances calcium influx into primary rat alveolar macrophages resulting in expression of TNF- α . Treatment with verapamil, a calcium channel blocker, prevents the ultrafine carbon black induced TNF- α production.⁷ In a report published earlier this year, Li *et al* have shown that Nimodipine, a calcium channel inhibitor, attenuates microglial activation resulting in neuroprotective functions. Specifically, there were significantly decreased concentrations of nitric oxide, TNF- α , IL-1 β and PGE₂ produced from LPS-stimulated microglia treated

with Nimodipine.²⁵ Taken together, I hypothesize that calcium channel inhibitors may act to inhibit the microglial production of select cytokines known to augment reactive astrocytosis, thereby attenuating the onset of gliosis.

Astrocyte L-type calcium ion channel expression increases in several models of CNS injury such as kainic acid-induced epilepsy, mechanical and thermal lesions and ischemia.⁴⁹ Three weeks post-stab wound, reactive astrocytes are observed to express neuronal and L-type calcium ion channels.¹ Increase in astrocytic intracellular calcium concentration through application of a calcium ionophore results in increased production of GFAP.²⁴ Early work has shown that the application of verapamil at the time of lesion reduces the amount of GFAP staining at lesion site after 72 hours by 80% compared to treatment with saline.²³ Calcium channel blockers nickel, nifedipine verapamil and diltiazem, attenuate GFAP expression in astrocytes activated through acidic conditions.^{24,}³⁹ In vivo spinal cord injury experiments confirmed the effect of acidity and calcium channel blockers on reactive gliosis.¹⁰ These results suggest that increased intracellular calcium levels are necessary for astrocyte activation. As calcium ion channels are a significant source of intracellular calcium, an interesting application of yttrium oxide nanoparticles is to proximately release yttrium ions that would act to inhibit calcium ion channels and decrease reactive gliosis. The next section describes progress and experimental obstacles encountered in testing this hypothesis.

Preliminary Results

In the previous section, it was shown that calcium channel inhibitors decrease acid-triggered reactive gliosis. The main objective of this experimental work is to generate scaffolds containing carbon nanotubes and yttrium oxide nanoparticles, show yttrium leaching in acidic conditions and lastly demonstrate reduced astrocyte activation. This work is ongoing and therefore the data presented is preliminary.

Scaffold Formation

Many techniques were explored for the generation of scaffolds for astrocytic growth. Ideally, the scaffolds should be a homogeneous layer of nanotubes and yttrium oxide nanoparticles adhered to circular glass coverslips. The following techniques, previously reported in the literature, were explored for this application: airbrushing, spin coating, bar coating, drop coating, and vacuum filtration using various solvents such as ethanol, dimethylformamide (DMF), gum Arabic, water, tocopheryl polyethylene glycol 1000 succinate (TPGS) and sodium dodecyl sulfate. Vacuum filtration produced the most visually uniform scaffolds. Scanning electron micrograph of the scaffold is shown in Figure 4.1A. Further tests, such as atomic force microscopy, will need to be conducted to determine surface roughness.

The following procedure was used to generate scaffolds of carbon nanotubes and yttrium oxide nanoparticles. Purified single-walled nanotubes were suspended in 1.6% deoxycholate⁶ through bath sonication then centrifuged

for 10 min at 3,000 RPM and 4°C. The supernatant, containing the dispersed nanotubes was then used for vacuum filtration. Yttrium oxide nanoparticles were

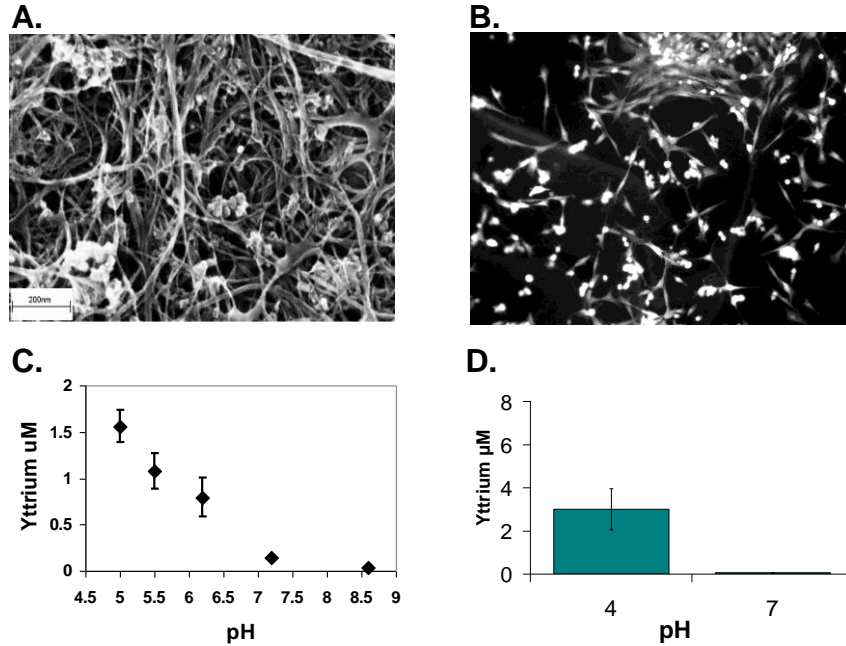


Figure 4.1 Carbon Nanomaterial and Yttrium Oxide Scaffolds

A. Scanning Electron Micrograph of single-walled carbon nanotube/Yttrium Oxide scaffold generated through vacuum filtration. B. Astrocyte cell line transfected with Green Fluorescent Protein cultured on carbon nanotube/yttrium oxide nanoparticle scaffolds. C. Yttrium ion release from 5 μM Yttrium Oxide nanoparticles in water as a function of solution pH. pH was adjusted and samples were allowed to incubate for 15 minutes prior to removal of nanoparticles through centrifugation. Availability was measured through Inductively Coupled Plasma Atomic Emission Spectroscopy. D. Yttrium ion release into culture media from Carbon Nanotube/Yttrium oxide nanoparticle scaffolds as a function of pH. Scaffolds were allowed to incubate for 48 hours in the absence of astrocytes.

stored suspended in water pH9 and at 4°C. Various combinations of single-walled nanotubes and yttrium oxide nanoparticles were deposited onto Millipore mixed cellulose esters (MCE) membranes. Acetone was used to dissolve the

membrane, effectively affixing the nanotube/yttrium oxide nanoparticle scaffold to the coverslips.⁵⁰

Yttrium Bioavailability

Yttrium ion release from yttrium oxide nanoparticles is the basis of this experimental hypothesis. Inductively coupled plasma atomic emission spectroscopy bioavailability assays were conducted to determine yttrium ion release. Free yttrium oxide nanoparticles in water of basic pH do not release yttrium ions. As the pH is lowered to more acidic conditions yttrium ions are released. In Figure 4.1C samples of 5 μ M yttrium oxide nanoparticles in water are taken as a function of water pH. As the pH approaches 6, yttrium ions are released more readily into solution. If the initial loading of 5 μ M yttrium oxide nanoparticles was fully oxidized into yttrium ions, 10 μ M yttrium would be expected. The results presented in Figure 4.1C suggest that at pH 5.5 roughly 10% of the total possible yttrium is released in ionic form. More experiments are needed to fully understand yttrium ion release kinetics from yttrium oxide nanoparticles. In particular, ion release as a function of incubation time at a given pH would be beneficial to the present experiments. While the data suggests that the maximum available yttrium ion concentration is not released at slightly acidic pH, the concentration that is released is sufficient to inhibit calcium ion channels. Therefore, in Figure 4.1D this observation is extended to demonstrate yttrium ion release from carbon nanotube/yttrium oxide nanoparticle scaffolds as a function of media pH. In acidic media, yttrium is released from scaffolds whereas at physiological pH, yttrium ions are not detectable. While

more experiments are needed to develop a clear understanding of the kinetics involved in yttrium ion release from yttrium oxide nanoparticles, this preliminary data is encouraging. A scaffold which releases yttrium ions when the cells are experiencing the applied stress of the acid treatment and does not release yttrium ions under normal physiological conditions would be experimentally ideal.

Cell studies

In the literature, it was shown that calcium inhibitors attenuate acidity triggered reactive gliosis in vitro and in vivo^{10, 24, 39}. In this section, the objective is to demonstrate attenuated acidity-induced astrocyte activation utilizing ionic yttrium released from the aforementioned scaffolds. Immortalized astrocyte cell line DI TNC1 (ATTC CRL 2005) was chosen as the cell line for these preliminary studies. The cell line is established from primary cultures of type 1 astrocytes from brain diencephalon tissue of day old rats and is advertised to retain characteristics consistent with the phenotype of type 1 astrocytes including glial fibrillary acidic protein (GFAP) immunoreactivity. Cells were cultured as recommended and were viable when cultured on carbon nanotube/yttrium oxide nanoparticle scaffolds (Figure 4.1 B).

In an experiment designed as a control to demonstrate the effect of ionic yttrium to attenuate acidity induced astrocyte activation, uniform levels of GFAP expression was observed, suggesting the cells have not activated (Figure 4.2) This could be due to a number of reasons; it is possible the media pH is not low enough to induce activity, the differences in expression are so small it is not detectable through microscopy, or the GFAP antibody was not working correctly.

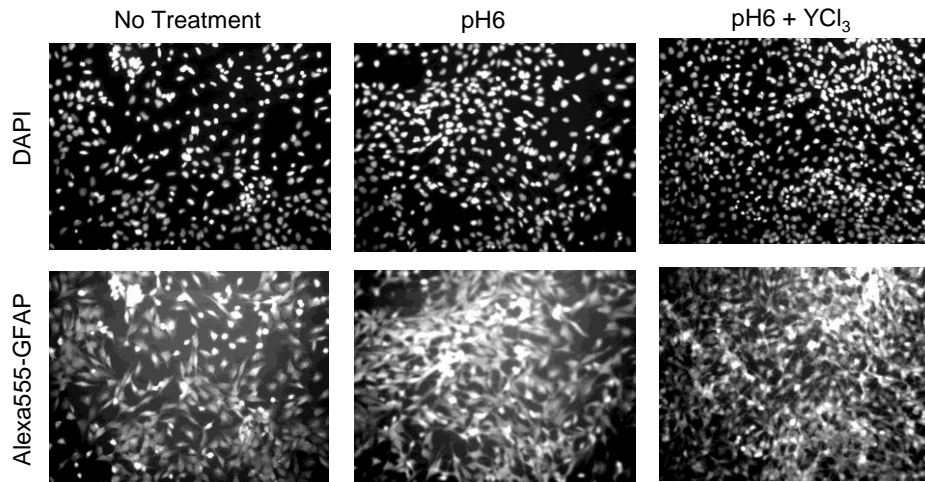


Figure 4.2 Astrocyte cell line exposed to acidic conditions.

Cells were untreated, treated with media of pH 6, or treated with media pH 6 with 3µM yttrium chloride. Cells were stained for nuclear marker DAPI and Alexa 555 conjugated antibody to GFAP. Increased GFAP signaling, indicative of activated astrocytes, is expected from cells treated with acidic media; GFAP signaling similar to the untreated control is expected from cells treated with yttrium chloride.

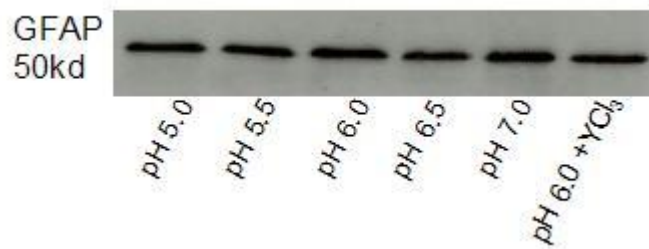


Figure 4.3 Western blot of Astrocyte Activation as a function of media pH.

Astrocyte cells were cultured and treated for two hours to media of pH 5.0-7.0. One sample was treated with media of pH 6 and 3µM yttrium chloride. Equal concentrations of protein were loaded into each well and labeled with CellSignal Technology GFAP (GA5) Mouse mAb #3670.

To explore these possibilities, the cells were then exposed to a range of acidic conditions for two hours. In figure 4.3, a western blot, using a different unconjugated GFAP antibody, suggests this cell line is in fact not activating under acidic conditions. In light of these recent results, future work on this project should involve the use of primary cell cultures.

To conclude, combining the use of carbon nanotubes with yttrium oxide nanoparticles to increase charge transfer and decrease glial scar formation around chronically implanted neural electrodes, is a unique hypothesis worthy of further experimentation. Yttrium is released as a function of decreased pH. Therefore, the use of yttrium oxide nanoparticles for this application is advantageous, since under physiological conditions, yttrium ions will not be released. Additionally, the use of a carbon nanotube scaffolds and the presence of metal catalysts improve electrode electrochemical behavior^{12, 22, 38}. Therefore, it may be hypothesized that the addition of yttrium oxide nanoparticles to the surface of an electrode will increase conductivity. This functional ability is unique from other calcium channel inhibitors and therefore advantageous. Traditional calcium channel inhibitors, unless encapsulated in an acid-sensitive polymer coating, will be bioavailable at all times. Additionally, the use of a polymer coating may increase electrode impedance, and be subject to shear upon implantation. It should be noted that in using yttrium oxide nanoparticles with carbon nanotubes for this application, the carbon nanotubes and yttrium oxide nanoparticles do not biodegrade under physiological conditions. As the coating

will be used on an electrode which is also not biodegradable, it does not seem likely to be an issue moving forward.

Preliminary data presented is hopeful, however, experiments still need to be performed to validate this hypothesis. This includes a more extensive characterization of yttrium ion release from yttrium oxide nanoparticles, and experiments coupling ion bioavailability with the potential physiological effect of attenuated astrocytic activation in primary cultures. As mentioned in the background section, the hypothesis can be extended to decrease microglial activation and improve neuronal viability. Therefore future studies can address these additional cell types.

4.3 References

1. Agrawal, S.K. and R. Nashmi and M.G. Fehlings. 2000. Role of L- and N-type calcium channels in the pathophysiology of traumatic spinal cord white matter injury. *Neuroscience*. 99: 1 179-188.
2. Awan, N.R. and A.M. Lozano and C. Hamani. 2009. Deep brain stimulation: current and future perspectives. *Neurosurgical Focus*. 27: 1 E2-
3. Beedle, A.M. and G. Zamponi. 2002. Inhibition of Transiently Expressed Low- and High- Voltage-Activated Calcium Channels by Trivalent Metal Cations. *Journal of Membrane Biology*. 187 225-238.
4. Bhaviripudi, S. and E. Mile and S.A. Steiner and A.T. Zare and M.S. Dresselhaus and A.M. Belcher and J. Kong. 2007. CVD Synthesis of Single-Walled Carbon Nanotubes from Gold Nanoparticle Catalysts. *Journal of the American Chemical Society*. 129: 6 1516-1517.
5. Biran, R. and D.C. Martin and P.A. Tresco. 2005. Neuronal cell loss accompanies the brain tissue response to chronically implanted silicon microelectrode arrays. *Experimental Neurology*. 195: 1 115-126.
6. Blanch, A.J. and C.E. Lenehan and J.S. Quinton. 2010. Optimizing Surfactant Concentrations for Dispersion of Single-Walled Carbon Nanotubes in Aqueous Solution. *The Journal of Physical Chemistry B*. 114: 30 9805-9811.
7. Brown, D.M. and K. Donaldson and V. Stone. 2002. Role of Calcium in the Induction of TNF α Expression by Macrophages on Exposure to Ultrafine Particles. *Annals of Occupational Hygiene*. 46: 2 219-222.
8. Cellot, G. and E. Cilia and S. Cipollone and V. Rancic and A. Sucapane and S. Giordani and L. Gambazzi and H. Markram and M. Grandolfo and D. Scaini and F. Gelain and L. Casalis and M. Prato and M. Giugliano and L. Ballerini. 2008. Carbon Nanotubes might improve neuronal performance by favouring electrical shortcuts. *Nature Nanotechnology*. 4: 126-133.

9. Cheung, K.C. 2007. Implantable microscale neural interfaces. *Biomedical Microdevices*. 9: 923-938.
10. Du, S. and A. Rubin and S. Klepper and C. Barrett and Y.C. Kim and H.W. Rhim and E.B. Lee and C.W. Park and G.J. Markelonis and T.H. Oh. 1999. Calcium Influx and Activation of Calpain I Mediate Acute Reactive Gliosis in Injured Spinal Cord. *Experimental Neurology*. 157: 1 96-105.
11. Fitch, M.T. and J. Silver. 2008. CNS injury, glial scars, and inflammation: Inhibitory extracellular matrices and regeneration failure. *Experimental Neurology*. 209: 294-301.
12. Gabriel, G. and R. Gómez-Martinez and R. Villa. 2008. Single-walled carbon nanotubes deposited on surface electrodes to improve interface impedance. *Physiological Measurement*. 29: S203-S212.
13. Griffith, R.W. and D.R. Humphrey. 2006. Long-term gliosis around chronically implanted platinum electrodes in the *Rhesus macaque* motor cortex. *Neuroscience Letters*. 406: 1-2 81-86.
14. Grill, W.M. and S.E. Normal and R.V. Bellamkonda. 2009. Implanted Neural Interfaces: Biochallenges and Engineered Solutions. *Annual Review of Biomedical Engineering*. 11: 1-24.
15. Hamani, C. and M.P. McAndrews and M. Cohn and C.M. Shapiro and R.A. Wennberg and A.M. Lozano. 2008. Memory Enhancement Induced by Hypothalamic Fornix Deep Brain Stimulation. *Ann Neurol*. 63: 1 119-123.
16. He, W. and G.C. McConnell and T.M. Schneider and R.V. Bellamkonda. 2007. A Novel Anti-inflammatory Surface for Neural Electrodes. *Advanced Materials*. 19: 3529-3533.
17. Hille B. 2001. *Ion Channels of Excitable Membranes*. Sinauer Associates, Inc., Sunderland, MA USA.
18. Hirsch, A. 2009. Growth of Single-Walled Carbon Nanotubes without a Metal Catalyst – A Surprising Discovery. *Angewandte Chemie International Edition*. 48: 30 5403-5404.

19. Hochberg, L.R. and M.D. Serruya and G.M. Friehs and J.A. Mukand and M. Saleh and A.H. Caplan and A. Branner and D. Chen and R.D. Penn and J.P. Donoghue. 2006. Neuronal ensemble control of prosthetic devices by a human with tetraplegia. *Nature*. 442: 164-171.
20. Hoffmann, A. and O. Kann and C. Ohlemeyer and U.-K. Hanisch and H. Kettenmann. 2003. Elevation of Basal Intracellular Calcium as a Central Element in the Activation of Brain Macrophages (Microglia) Suppression of Receptor-Evoked Calcium Signaling and Control of Release Function. *Journal of Neuroscience*. 23: 11 4410-4419.
21. Hu, H. and Y. Ni and V. Montana and R.C. Haddon and V. Papura. 2004. Chemically Functionalized Carbon Nanotubes as Substrates for Neuronal Growth. *Nano Letters*. 4: 3 507-511.
22. Keefer, E.W. and B.R. Botterman and M.I. Romero and A.F. Rossi and G.W. Gross. 2008. Carbon nanotube coating improves neuronal recordings. *Nature Nanotechnology*. 3: 434-439.
23. Klepper, S. and F. Naftolin and J.M. Piepmeier. 1995. Verapamil treatment attenuates immunoreactive GFAP at cerebral cortical lesion site. *Brain Research*. 695: 245-249.
24. Lee, Y.B. and S. Du and H.W. Rhim and E.B. Lee and G.J. Markelonis and T.H. Oh. 2000. Rapid increase in immunoreactivity to GFAP in astrocytes in vitro induced by acidic pH is mediated by calcium influx and calpain I. *Brain Research*. 864: 2 220-229.
25. Li, Y. and X. Hu and Y. Liu and Y. Bao and L. An. 2009. Nimodipine protects dopaminergic neurons against inflammation-mediated degeneration through inhibition of microglial activation. *Neuropharmacology*. 56: 580-589.
26. Liu, X. and L. Guo and D. Morris and A.B. Kane and R.H. Hurt. 2008. Targeted Removal of Bioavailable Metal as a Detoxification Strategy for Carbon Nanotubes. *Carbon*. 43: 3 489-500.
27. Lovat, V. and D. Pantarotto and L. Lagostena and B. Cacciari and M. Grandolfo and M. Righi and G. Spalluto and M. Prato and L. Ballerini. 2005. Carbon Nanotube Substrates Boost Neuronal Electrical Signaling. *Nano Letters*. 5: 6 1107-1110.

28. Malarkey, E.B. and R.C. Reyes and B. Zhao and R.C. Haddon and V. Parpura. 2008. Water Soluble Single-walled Carbon Nanotubes Inhibit Stimulated Endocytosis in Neurons. *Nano Letters*. 8: 10 3538-3542.
29. Mattson, M.P. and R.C. Haddon and A.M. Rao. 2000. Molecular Functionalization of Carbon Nanotubes and Use as Substrates for Neuronal Growth. *Journal of Molecular Neuroscience*. 14: 175-182.
30. Mazzatenta, A. and M. Giugliano and S. Campidelli and L. Gambazzi and L. Businaro and H. Markram and M. Prato and L. Ballerini. 2008. Interfacing Neurons with Carbon Nanotubes: Electrical Signal Transfer and Synaptic Stimulation in Cultured Brain Circuits. *Journal of Neuroscience*. 27: 26 6931-6936.
31. McConnell, G.C. and R.J. Butera and R.V. Bellamkonda. 2009. Bioimpedance modeling to monitor astrocytic response to chronically implanted electrodes. *Journal of Neural Engineering*. 6: 55005-55015.
32. McConnell, G.C. and H.D. Rees and A.I. Levey and C.-A. Gutekunst and R.E. Gross and R.V. Bellamkonda. 2009. Implanted neural electrodes cause chronic, local inflammation that is correlated with local neurodegeneration. *Journal of Neural Engineering*. 6: 56003-56015.
33. Mlinar, B. and J.J. Enyeart. 1992. Block of current through T-type calcium channels by trivalent metal cations and nickel in neural rat and human cells. *Journal of Physiology*. 469 639-652.
34. Nachshen, D.A. 1984. Selectivity of the Ca Binding Site in Synaptosome Ca Channels. *Journal of General Physiology*. 83: 941-967.
35. Ni, Y. and H. Hu and E.B. Malarkey and B. Zhao and V. Montana and R.C. Haddon and V. Parpura. 2005. Chemically Functionalized Water Soluble Single-Walled Carbon Nanotubes Modulate Neurite Outgrowth. *Journal of Nanoscience and Nanotechnology*. 5: 1707-1712.
36. Nicolelis, M.A.L. and D. Dimitrov and J.M. Carmena and R. Crist and G. Lehew and J.D. Kralik and S.P. Wise. 2003. Chronic, multisite, multielectrode recordings in macaque monkeys. *Proceedings of the National Academy of Sciences*. 100: 19 11041-11046.

37. Nicolelis, M.A.L. and M.A. Lebedev. 2009. Principles of neural ensemble physiology underlying the operation of brain-machine interfaces. *Nature*. 10: 530-540.
38. Niessen, R.A.H. and J. de Jonge and P.H.L. Notten. 2006. The Electrochemistry of Carbon Nanotubes. *Journal of The Electrochemical Society*. 153: 8 A1484-A1491.
39. Oh, T.H. and G.J. Markelonis and J.R. Von Visger and B. Baik and M.T. Shipley. 1995. Acidic pH rapidly increases immunoreactivity of glial fibrillary acidic protein in cultured astrocytes. *Glia*. 13: 4 319-322.
40. Park, K.H. and M. Chhowalla and Z. Iqbal and F. Sesti. 2003. Single-walled Carbon Nanotubes are a New Class of Ion Channel Blockers. *Journal of Biological Chemistry*. 278: 50 50212-50216.
41. Pekny, M. and M. Nilsson. 2005. Astrocyte Activation and Reactive Gliosis. *Glia*. 50: 427-434.
42. Pethig, R. and A. Menachery and E. Heart and R.H. Sanger and P.J.S. Smith. 2008. Dielectrophoretic assembly of insulinoma cells and fluorescent nanosensors into threedimensional pseudo-islet constructs. *IET Nanobiotechnology*. 2: 2 31-38.
43. Polikov, V.S. and P.A. Tresco and W.M. Reichert. 2005. Response of brain tissue to chronically implanted neural electrodes. *Journal of Neuroscience Methods*. 148: 1-18.
44. Schubert, D. and R. Dargusch and J. Raitano and S.-W. Chan. 2006. Cerium and yttrium oxide nanoparticles are neuroprotective. *Biochemical and Biophysical Research Communications*. 342: 86-91.
45. Stroncek, J.D. and W.M.Reichert Overview of Wound Healing in Different Tissue Types. pp. 3-39. *In: W.M. Reichert. [eds.] 2007. **Indwelling Neural Implants: Strategies for Contending with the In Vivo Environment.** Taylor & Francis Group,*
46. Szarowski, D.H. and M.D. Andersen and S. Retterer and A.J. Spence and M. Isaacson and H.G. Craighead and J.N. Turner and W. Shain. 2003.

Brain responses to micro-machined silicon devices. Brain Research. 983: 23-35.

47. Turner, J.N. and W. Shain and D.H. Szarowski and M. Andersen and S. Martins and M. Isaacson and H. Craighead. 1999. Cerebral Astrocyte Response to Micromachined Silicon Implants. Experimental Neurology. 156: 33-49.
48. Wadhwa, R. and C.F. Lagenaur and X.T. Cui. 2005. Electrochemically controlled release of dexamethasone from conducting polymer polypyrrole coated electrode. Journal of Controlled Release. 110: 3 531-541.
49. Westenbroek, R.E. and S.B. Bausch and R.C.S. Lin and J.E. Franck and J.L. Noebels and W.A. Catterall. 1998. Upregulation of L-Type Ca^{2+} Channels in Reactive Astrocytes after Brain Injury, Hypomyelination, and Ischemia. Journal of Neuroscience. 18: 7 2321-2334.
50. Wu, Z. and Z. Chen and X. Du and J.M. Logan and J. Sippel and M. Nikolou and K. Kamaras and J.R. Reynolds and D.B. Tanner and A.F. Hebard and A.G. Rinzler. 2004. Transparent, Conductive Carbon Nanotube Films. Science. 305: 5688 1273-1276.